

A Thesis Submitted for the Degree of PhD at the University of Warwick

Permanent WRAP URL:

<http://wrap.warwick.ac.uk/101575/>

Copyright and reuse:

This thesis is made available online and is protected by original copyright.

Please scroll down to view the document itself.

Please refer to the repository record for this item for information to help you to cite it.

Our policy information is available from the repository home page.

For more information, please contact the WRAP Team at: wrap@warwick.ac.uk



**Algorithms for the Analysis of Bone Marrow
Cancer Histology Images**

by

Tzu-Hsi Song

Thesis

Submitted to the University of Warwick

for the degree of

Doctor of Philosophy

Department of Computer Science

July 2017

THE UNIVERSITY OF
WARWICK

Contents

| | |
|---|-------------|
| List of Tables | v |
| List of Figures | vi |
| Acknowledgments | xiv |
| Declarations | xv |
| List of Publication | xvi |
| Abstract | xvii |
| Abbreviations | xix |
| Chapter 1 Introduction | 1 |
| 1.1 Myeloproliferative Neoplasms | 3 |
| 1.1.1 Subtypes of MPNs | 5 |
| 1.1.2 WHO criteria of MPNs | 6 |
| 1.2 Digital Pathology | 8 |
| 1.3 Motivation | 10 |
| 1.4 Aims and Objectives of the Thesis | 13 |
| 1.5 Main Contributions | 14 |
| 1.6 Thesis Organization | 15 |

| | |
|---|-----------|
| Chapter 2 Literature Review | 16 |
| 2.1 Problems in Histology Image Analysis | 17 |
| 2.1.1 Segmentation | 20 |
| 2.1.2 Detection | 23 |
| 2.1.3 Classification | 27 |
| 2.2 Approaches for Histology Image Analysis | 28 |
| 2.2.1 Active Contour | 28 |
| 2.2.2 Classical Machine Learning Approaches | 32 |
| 2.2.3 Deep Learning Approaches | 33 |
| 2.2.3.1 Neural Networks | 34 |
| 2.2.3.2 Autoencoder | 36 |
| 2.2.3.3 Convolutional Neural Network | 38 |
| 2.3 Materials and Related Methods | 40 |
| 2.4 Summary | 40 |
| | |
| Chapter 3 Megakaryocyte Delineation using a Traditional Approach | 42 |
| 3.1 Introduction | 42 |
| 3.2 The Basic Framework | 46 |
| 3.2.1 Stain Normalization and Deconvolution | 46 |
| 3.2.2 Megakaryocytic selection | 48 |
| 3.2.3 Circumscribing Active Contour Model | 51 |
| 3.3 The Proposed Framework | 55 |
| 3.3.1 Delineation of MK Nuclei | 55 |
| 3.3.2 The Proposed Dual-Channel Active Contour Model | 58 |
| 3.3.2.1 The External Energy Force | 58 |
| 3.3.2.2 The External Energy Force on Stain Channel Images | 60 |
| 3.4 Experimental Results | 65 |
| 3.4.1 Evaluation of MK nuclei detection | 65 |

| | | |
|------------------|--|-----------|
| 3.4.2 | Evaluation of the Proposed DCAC Model | 67 |
| 3.4.3 | Comparison with Multi-Region Active Contour Model | 72 |
| 3.5 | Summary | 75 |
| Chapter 4 | Cell Detection via Hybrid Deep Autoencoder | 76 |
| 4.1 | Introduction | 76 |
| 4.2 | The Proposed Method | 78 |
| 4.2.1 | Curve-Support Gaussian Model | 78 |
| 4.2.2 | Training of Encoder and Decoder networks | 81 |
| 4.2.3 | The Connecting Layer | 82 |
| 4.3 | Hybrid Deep Autoencoder | 83 |
| 4.4 | Experimental Results | 86 |
| 4.4.1 | The Dataset | 86 |
| 4.4.2 | Network Architectures Setting | 86 |
| 4.4.3 | Generation of Training and Testing Sets | 88 |
| 4.4.4 | Training the HDAE | 88 |
| 4.4.5 | Comparison of the proposed network with other deep learning methods | 91 |
| 4.5 | Summary | 96 |
| Chapter 5 | A Synchronized Asymmetric Deep Learning Model for Cell Classification | 97 |
| 5.1 | Introduction | 97 |
| 5.2 | Related Work | 99 |
| 5.3 | Methodology | 101 |
| 5.3.1 | Conventional Deep AE Structure of Classification | 101 |
| 5.3.2 | Synchronized Hybrid Deep AE | 102 |
| 5.4 | Synchronized Asymmetric Deep Hybrid AE (Syn-ADHA) | 104 |
| 5.4.1 | Neighboring Class Selector | 109 |

| | | |
|--|---|------------|
| 5.5 | Experimental Results | 110 |
| 5.5.1 | Data collection | 110 |
| 5.5.2 | Network Setting and Training | 110 |
| 5.5.3 | Evaluation and Comparison of Syn-AHDA network | 111 |
| 5.5.4 | Computational Run Times | 115 |
| 5.6 | Summary | 115 |
| Chapter 6 Conclusions and Future Work | | 116 |
| 6.1 | Conclusions | 116 |
| 6.2 | Future Directions | 118 |

List of Tables

| | | |
|-----|--|-----|
| 1.1 | World Health Organization (WHO) diagnostic criteria for PV, ET and PMF [1]. | 7 |
| 3.1 | MK nuclei detection accuracy of three evaluated methods | 66 |
| 3.2 | Parameters of the evaluated models | 67 |
| 3.3 | Average of accuracy, number of iterations and run times of Ballaro’s method and four evaluated active contour models for delineating MKs | 72 |
| 3.4 | Segmentation accuracy of the proposed framework and the multi-region active contour model for MK cell, nuclear and cytoplasmic regions | 73 |
| 4.1 | Architectures and parameter setting of HDAE network. The network consists of input network N_I , connect network N_C , and probability network N_P | 87 |
| 4.2 | Comparative results for detection | 92 |
| 5.1 | Comparison of results of detection between the proposed model and other methods | 114 |
| 5.2 | Comparison of classification results between the proposed model and other combined approaches | 114 |
| 5.3 | Comparison of the training time between conventional frameworks and the proposed method | 115 |

List of Figures

| | | |
|-----|---|---|
| 1.1 | The process of capturing the BM aspiration and trephine biopsy. The doctor often chooses the back of hip bone and then places the bone marrow needle through the skin into bone. For BM aspiration, the doctor uses a syringe on the back of needle to draw out the liquid portion of BM. For BM biopsy, the doctor presses the needle further down into the bone with a twisting motion and a small BM sample is taken up into the needle [2,3]. | 2 |
| 1.2 | Visual examples of BM aspiration biopsies. Aspiration is primarily utilized for cytological assessment and consists of population of hemopoietic cells, such as erythroid, myeloid and lymphoid cells at various stages. In left aspiration image, there are many different types of BM cells: erythroblasts (with blue cytoplasm), red blood cells (without nuclei), myelocytes, monocytes, band neutrophils, eosinophil (with pink cytoplasm), megakaryocyte(right slide of the image); there are five erythroblasts with various stages, one myelocyte, two lymphocytes and one neutrophil in right image [4–6]. | 3 |

| | | |
|-----|--|----|
| 1.3 | Visual examples of BM trephine biopsies (10×). Trephine biopsy allows the evaluation of the bone marrow's overall cellularity. In above sample images, there are three main components: bone trabeculae with pink texture, adipocytes with white circle areas, and other type of cells including megakaryocytes, erythroid cells and myeloid cells. | 4 |
| 1.4 | The workflow of digital pathology for disease diagnosis. Clinical slides are scanned and digitized to get high-revolution whole slide images. These digital images are easily stored into and accessed from any storage device, such as cloud storage. The pathologists can immediately share and discuss digital slides even if they do not sit together. Moreover, digital slides can be investigated and analyzed by computer-aided techniques for helping disease diagnosis [7–11]. | 9 |
| 1.5 | Examples of ET and prefibrotic PMF [12]. The left case belongs to ET, and the other one is prefibrotic PMF. There are no obvious morphological characteristics or cytological architecture to distinguish between them and pathologists have low agreement of identifying these two bone marrow diseases. In the study [13], it also mentions that many patients with prefibrotic PMF are diagnosed with ET because of unclear and ambiguous diagnostic features. | 11 |
| 1.6 | The diagram of research objectives. According to the aims of thesis, the final framework will automatically do quantitative analysis of BM trephine biopsies and provide the statistical information to help the pathologists improve the accuracy of distinguishing ET and prefibrotic PMF. There three major sections (in blue-dash rectangle) to construct the proposed final framework: megakaryocyte delineation, non-MK cell detection, and classification of erythroid and myeloid cells. | 13 |

| | | |
|-----|--|----|
| 2.1 | Examples of histology images in different cancer tissue: (a) Breast (b) Prostate (c) Lung and (d) Bone marrow. We observe the various types of cells with complicated morphological features in each case. These massive variations show that computer-aided methods face difficulty in obtaining accurate and specific histology and cellularity information. | 18 |
| 2.2 | The all possible cases of region-based active contour [14, 15]. F1 energy force is generated from inside region of the contour, and F2 energy force is from outside region of the contour. If one of these two energy forces is larger than the other, the fitting energy moves the contour toward the lower energy region. If fitting energy is equal to zero, the movement of the contour will stop and fix. | 30 |
| 2.3 | The diagram of structure of a layer of neural network. The input data are multiplied by the weights to extract the feature elements, and then feature elements are added together. The sum of feature elements is processed by an activation function to output the result. | 34 |
| 2.4 | The basic structure of autoencoder. Blue and red dash boxes represents the encoding and decoding sections, respectively. Autoencoder learns compressed feature vector of input images by comparing with reconstructed images. | 36 |
| 2.5 | The general architecture of CNN. CNN uses convolutional and pooling layers to extract the feature maps from input data and reduce the size of feature maps for accelerating processing speed. Then fully connection layers and softmax layer are used to capture high-level global features and combine them to obtain the proposed task, like classification. | 38 |

| | | |
|-----|--|----|
| 3.1 | Representative examples of bone marrow trephine histology images. The MKs are contained within the yellow dotted rectangles. Note that MK cytoplasm is often partially occluded by nearby cells, other cytoplasmic and non-smooth regions, and their boundaries usually comprise weak edges. | 43 |
| 3.2 | The workflow of the framework with the basic CAC model. | 47 |
| 3.3 | Example results of stain normalization and color deconvolution process. Input images are on the left, while output stain channel images are on the right. | 47 |
| 3.4 | Intermediate samples of the process followed to identify MK nuclei in the basic framework. Overlapping the masks of all nuclei and MK cytoplasm and thresholding the size of nuclei are used to select potential MK nuclei. | 49 |
| 3.5 | The region outside of the current evolving contour C in CV model and in the CAC model | 53 |
| 3.6 | The workflow of the framework with the proposed DCAC model. . . | 56 |
| 3.7 | Example intermediate results of the process followed to identify MK nuclei in the proposed framework. The masks of all nuclei and MK cytoplasm are used to identify MK nuclei. | 56 |
| 3.8 | An example initial contour and the corresponding inside region and the nuclear boundary, C_n . The initial contour (in green) is obtained by dilating C_n (in yellow). | 57 |

| | | |
|------|--|----|
| 3.9 | The upper row shows how the difference between pixel values and c_H is larger on the H-channel image than on the E-channel image. This helps to stop the evolving contour when encountering other nuclei outside the cytoplasmic regions. The bottom row shows how the E-channel image can be used to efficiently distinguish between the MK cytoplasmic region and other non-MK cytoplasm region different from nuclei. In other words, if the energy force of H-channel image is larger than that of E-channel image, the evolving contour will be stopped on the boundary of the nucleus by the energy force of H-channel image (upper row). If the energy force of E-channel image is larger than that of H-channel image, the energy force of E-channel image will control the evolving contour stopping on the boundary of non-MK cytoplasm region, like background (bottom row). When the difference between the energy force of H-channel image and the energy force of E-channel image is quite small, the evolving contour will stop moving. | 62 |
| 3.10 | An example evolving contour and the corresponding ring-like region. The green contour denotes the evolving contour C ; the blue dashed contour denotes the cytoplasmic boundary; the yellow contour denotes the nuclear boundary, C_n ; and the red dashed contour denotes the ring-like region boundary. | 65 |
| 3.11 | Visual results of the proposed DCAC model for identification of MK cytoplasmic boundaries. Yellow contours denote the segmented nuclear boundaries by the CV model. This boundary is used as the initial contour in the proposed model after dilating them. Green contours denote the identified cytoplasmic boundaries. Blue dashed contours denote the ground truth as manually annotated. | 68 |

| | | |
|------|---|----|
| 3.12 | Visual results of CV model (first row), LBF model (second row), CAC model (third row) and DCAC model (fourth row). The yellow line denotes the initial contour; the green line denotes the final result and the blue dashed line denotes the ground truth. | 69 |
| 3.13 | Visual results of my entire proposed framework (left column) and the multi-region active contour model (right column) for delineation of MK nuclear and cytoplasmic boundaries. Yellow contours denote the identified nuclear boundaries; green contours denote the identified cytoplasmic boundaries; red and blue dashed contours denote the ground truth of nuclear and cytoplasmic boundaries, respectively. . . | 74 |
| 4.1 | Many examples of bone marrow hematopoietic stem cells (40×). We observe that there are different types of cells densely mixing and randomly distributed in bone marrow tissue. Green and yellow arrows point out erythroid cells and myeloid cells, respectively. Some specific shaped myeloid cells are shown in yellow circles. | 77 |
| 4.2 | Some examples of input images and corresponding probability maps by using the curve-support Gaussian model. The parameter k controls the level of curvature. When k increases, the level of curvature becomes bigger. In addition, the parameter θ manages the orientation of curve-support Gaussian model. In the bottom right, there are some probability maps generated by combining different k and θ . . . | 80 |
| 4.3 | An overview of the proposed HDAE network. The top part of the Figure shows the whole structure of HDAE and the bottom part presents three sections to form final structure: (1) input AE network, (2) probability label AE network and (3) connect layer network. . . | 84 |

| | | |
|-----|--|----|
| 4.4 | Visual results for nuclear detection via the HDAE network. (a) An example image (b) Probability map generated by the HDAE network. Detecting the center of an individual nucleus is based on the location of local maxima found in the probability map. (c) Detection results of HDAE. Here the detected centers of the nuclei are shown as red dots and ground truth areas are green shaded circles. Detection results of the proposed method and other approaches are shown in Figure 4.5 and 4.6. | 90 |
| 4.5 | Comparative result for the proposed method and other approaches for nuclei detection on the sample image shown in Fig. 4.4(a): (a) BR, (b) EM, (c) LIPSyM, (d) SSAE, (e) SC-CNN, (f) HDAE. The ground truth areas are represented by green shaded circle and red dots represent detected centers of nuclei. The Precision (P), Recall (R) and F1-Score (F1) are listed below each sample. | 94 |
| 4.6 | Another comparative result for the proposed method and other approaches for nuclei detection: (a) BR, (b) EM, (c) LIPSyM, (d) SSAE, (e) SC-CNN, (f) HDAE. Also, the Precision (P), Recall (R) and F1-Score (F1) are shown below each sample case. It shows that the proposed method provides better performance of nuclei detection than other conventional and learning approaches. | 95 |
| 5.1 | Examples of different types of bone marrow hematopoietic stem cells by H&E staining. There are two major cell types: erythroid cells and myeloid cells. The myeloid cells include several subtypes of cells but are difficult to be observed and identified by experts. Moreover, some of erythroid and myeloid samples have similar and rather fuzzy shape or intensity features (last two columns). | 98 |

| | | |
|-----|---|-----|
| 5.2 | The representation of conventional progress for detection and classification via deep learning approaches. In general, there are two networks to process detection (upper dash-rectangle) and classification (bottom dash-rectangle) sequentially. | 101 |
| 5.3 | The architecture of synchronized HDAE network for detection and classification. The middle layer of connection network works with softmax classifier is used to identify different types of cells. | 103 |
| 5.4 | The structure representation of Syn-AHDA network. Here I construct an asymmetric learning network to detect the position of cell centers and classify different types of cells. The details of the key components: (1) asymmetric connect network and (2) probability network are shown in Fig. 5.5. | 105 |
| 5.5 | The structure of asymmetric connect network and probability network. There are two different processing sections to HDAE network in the training stage. The asymmetric connect network integrates one input vector and reconstructs two output vectors: the input vector for classification and probability label vector for detection. Moreover, the decoder of probability network is trained by the probability maps associated with corresponding class labels. | 105 |
| 5.6 | Sample results of detection and classification via Syn-AHDA network. Green and yellow dots represent the erythroid and myeloid cells, respectively. Red dots denote the incorrect cases of detection and cyan dots are incorrect cases of classification. | 113 |

Acknowledgments

It is my great honor to undertake this PhD which is absolutely an exciting and enjoyable experience in my life. This wonderful journey could never be accomplished without enduring supports and trusts from all my family, supervisors, collaborators and colleagues.

First, I would like to sincerely thank my supervisor Prof. Nasir Rajpoot for offering this opportunity of leading me into this incredible field and support to participate in scientific research under his patient, kind and professional supervision. I would like to thank my co-supervisor Dr. Victor Sanchez for his dedicated reviewing of my academic writing, inspirations to my research work during all these years. In addition, I would like to thank the adviser Dr. Hesham EIDaly for his patience and feedback with his expertise.

I am thankful to all current and previous TIAlab members: Dr. Samuel Jefferyes, Dr. Shan E Ahmed Raza, Dr. Adnan Khan, Dr. Violeta Kovacheva, Dr. Korsuk Sirinukunwattana, Dr. Nicholas Trahearn, Dr. Guannan Li, Mary Shapcott, Najah Alsubaie, Talha Qaiser, Muhammad Shaban and Simon Graham for their support and suggestions after listening to my research problems every time. I personally thank Dr. Korsuk Sirinukunwattana and Dr. Nicholas Trahearn. They always gave me good and useful advices and had private brainstorming meetings with me when I got stuck in research.

More importantly, I would like to thank my parents and my younger brother who provided me morally support and a massive dose of positive thinking while I am journeying along the way to complete my PhD.

Declarations

This thesis is submitted to the University of Warwick in support of my application for the degree of Doctor of Philosophy. It has been composed by myself, except where acknowledged, and has not been submitted in any previous application for any degree.

Tzu-Hsi Song

2017

List of Publication

- **Tzu-Hsi Song**, Victor Sanchez, Hesham EIDaly and Nasir M. Rajpoot, "Dual-Channel Active Contour Model for Megakaryocytic Cell Segmentation in Bone Marrow Trephine Histology Images", IEEE Transactions on Biomedical engineering, in press, 2017.
- **Tzu-Hsi Song**, Victor Sanchez, Hesham EIDaly and Nasir M. Rajpoot, "A circumscribing active contour model for delineation of nuclei and membranes of megakaryocytes in bone marrow trephine biopsy images", Proc. SPIE 9420, Medical Imaging 2015: Digital Pathology, 94200T, 2015.
- **Tzu-Hsi Song**, Victor Sanchez, Hesham EIDaly and Nasir M. Rajpoot, "Hybrid Deep Autoencoder with Curvature Gaussian of various types of cells in bone marrow trephine biopsy images, Conference on International Symposium on Biomedical Imaging (ISBI), 2017.
- **Tzu-Hsi Song**, Victor Sanchez, Hesham EIDaly and Nasir M. Rajpoot, "Simultaneous Cell Detection and Classification with an Asymmetric Deep Autoencoder in Bone Marrow Histology Images", Conference on Medical Image Understanding and Analysis (MIUA), 2017.

Abstract

Automated computer-aided systems and approaches are widely required to investigate and analyze histology images for improving the accuracy of cancer diagnosis and effective treatment decision making. Quantitative analysis has immense potential to investigate and analyze the tissue and cellular characteristics of histology images in cancer research. It is based on accurate cellular, morphological, and tissue features. Automated approaches not only make the feature extraction and analysis more objective and more reproducible, but they can also help pathologists look for useful potential clues from a vast amount of hidden information in cancer tissues, whose clinical value may not be fully realized and visualized. This entails the automated computer algorithms with a key role of quantitative analysis of histology images for different cancers.

In this thesis, I concentrate on bone marrow cancers and develop automated computer algorithms to extract and realize cellular and texture characteristics of bone marrow biopsies for efficiently characterizing different types of bone marrow cancers in further investigation and analysis. We focus on the development of automated algorithms for identifying various types of cells in bone marrow trephine biopsies, which are tiny cores of bone marrow tissues. All the algorithms are specifically designed for histological sections stained by a standard hematoxylin and eosin (H&E) stain. Firstly, we propose an automated framework with a novel segmentation model for delineating and segmenting megakaryocytes. Secondly, we create a novel deep learning network that processes the nuclear detection with irregular shape for various types of bone marrow stem cells. Then we construct another syn-

chronized deep learning approach to simultaneously do detection and classification. We demonstrate the effectiveness of the network of detection and classification at same time and the training time consumed in this synchronized network.

Abbreviations

| | |
|--------|--|
| AC | Active Contour |
| AE | Autoencoder |
| BM | Bone Marrow |
| BR | Blue Ratio |
| CAC | Circumscribing Active Contour |
| CAD | Computer-Assisted Diagnosis |
| CNN | Convolutional Neural Network |
| CV | Chan-Vese |
| DCAC | Dual-Channel Active Contour |
| DL | Deep Learning |
| EM | Expectation-maximization |
| ET | Essential Thrombocythemia |
| H&E | Hematoxylin and Eosin |
| HDAE | Hybrid Deep Autoencoder |
| LBF | Local Binary Fitting |
| LIPSyM | Local Isotropic Phase Symmetry Measure |
| ML | Machine Learning |
| MPNs | Myeloproliferative Neoplasms |
| NN | Neural Network |
| PCA | Principal Component Analysis |
| PMF | Primary Myelofibrosis |
| PV | Polycythemia Vera |

| | |
|----------|---|
| ROI | Region of Interest |
| SC-CNN | Spatially Constraint Convolutional Neural Network |
| SMC | Softmax Classifier |
| SSAE | Stacked Sparse Autoencoder |
| Syn-AHDA | Synchronized Asymmetric Hybrid Deep Autoencoder |
| UHCW | University Hospital Coventry and Warwickshire |
| WHO | World Health Organization |

Chapter 1

Introduction

Cancer is a group of diseases wherein the cancerous tissue exhibits out-of-control growth and many invade or spread to other parts of the body. It is one of the most serious and threatening diseases in the world and there are over 100 different types of cancers affecting humans [16]. Cancer causes altered cells to uncontrollably divide and grow to form masses of tissue, which are called tumor. According to the properties of tumors, the progress and attributes of cancer can be identified by expert pathologists and then the oncology specialists aim to give the patients efficient and precise treatments. In addition, there are some cancers that don't form solid tumors and can be diagnosed by analyzing the cellularity and morphology in the tissue, such as blood or bone marrow cancers.

Bone marrow (BM) cancer is a form of cancer that occurs in the spongy material inside the bones. The major functions of BM are to make new blood cells every day, including red blood cells, white blood cells, and platelets. These blood cells are differentiated from hematopoietic stem cells. When a person has bone marrow cancer, this process does not work properly and seriously affects hematopoietic function, coagulation, and immune function of the body. For instance, in leukemia, the bone marrow makes abnormal white blood cells to invade or destroy normal cells. In order to efficiently and precisely diagnose BM cancers, there are several

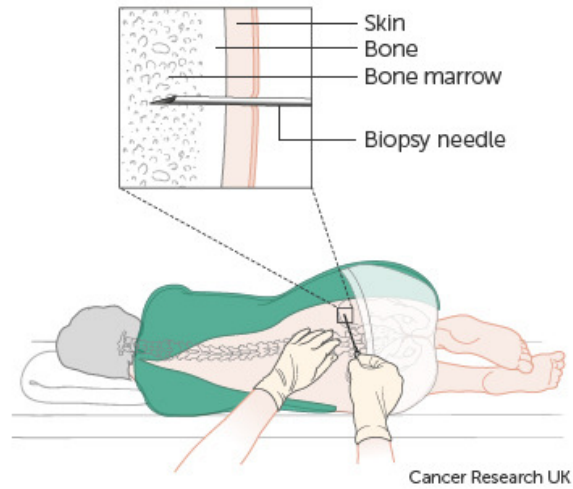


Figure 1.1: The process of capturing the BM aspiration and trephine biopsy. The doctor often chooses the back of hip bone and then places the bone marrow needle through the skin into bone. For BM aspiration, the doctor uses a syringe on the back of needle to draw out the liquid portion of BM. For BM biopsy, the doctor presses the needle further down into the bone with a twisting motion and a small BM sample is taken up into the needle [2,3].

clinical examinations in the diagnostic procedure. In general, a BM aspiration and a BM trephine biopsy are usually used to obtain cellular and morphological information to make accurate identification of BM cancers. Fig. 1.1 shows the clinical procedure of obtaining the BM aspirate and trephine specimen.

A BM aspiration is to suck some bone marrow cells up into a syringe, and a BM trephine biopsy is to remove a 1 or 2 cm core of bone marrow in one piece [13]. In other words, BM aspiration takes a liquid marrow sample and BM trephine biopsy takes a solid one. Both tests are usually performed at the same time. Fig. 1.2 and 1.3 show the sample images of BM aspiration and trephine biopsies under the microscope, respectively. These two tests provide information about the health of the bone marrow and its capability for blood cell production. Both tests not only give the overlapping BM information but also provide complementary pathological features. The BM trephine biopsy allows a complete assessment of marrow architecture and of the pattern of distribution of any abnormal infiltrate, whereas the

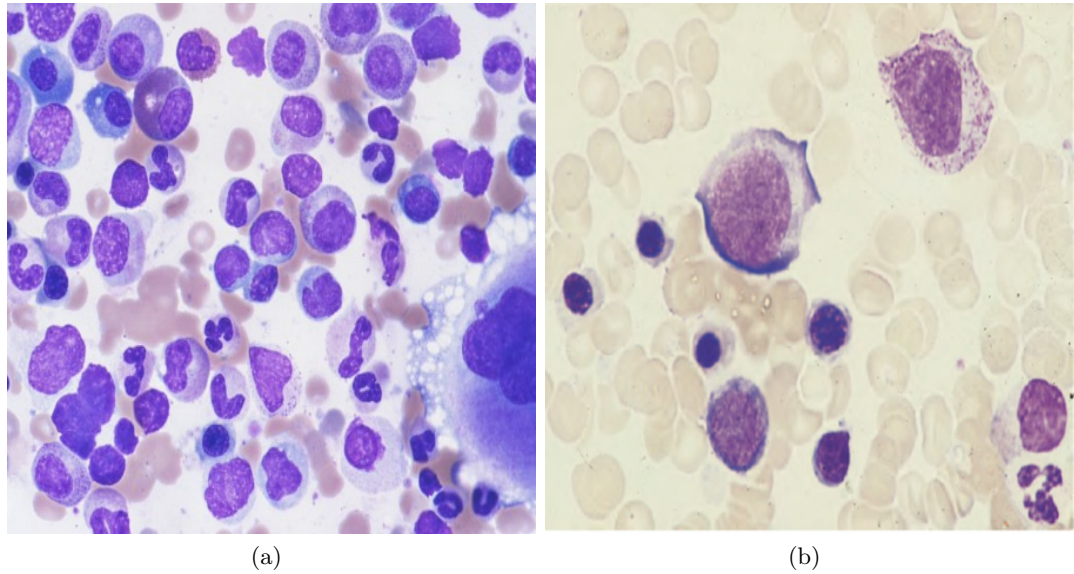


Figure 1.2: Visual examples of BM aspiration biopsies. Aspiration is primarily utilized for cytological assessment and consists of population of hemopoietic cells, such as erythroid, myeloid and lymphoid cells at various stages. In left aspiration image, there are many different types of BM cells: erythroblasts (with blue cytoplasm), red blood cells (without nuclei), myelocytes, monocytes, band neutrophils, eosinophil (with pink cytoplasm), megakaryocyte(right slide of the image); there are five erythroblasts with various stages, one myelocyte, two lymphocytes and one neutrophil in right image [4–6].

BM aspiration allows just the morphological and cytometric characteristics of bone marrow cells [13, 17]. These two advanced examinations can be used to investigate and indicate the stages of BM cancers for further treatment plans and progress. In this thesis, I concentrate on BM trephine biopsies for one type of BM cancers and develop image analysis methods to ultimately help pathologists make accurate diagnosis in early stage of cancer.

1.1 Myeloproliferative Neoplasms

Myeloproliferative neoplasms (MPNs) are a closely related group of progressive blood cancers and comprise a group of neoplastic disorders of BM hematopoietic stem cells, in which the hematopoietic cells proliferate abnormally [6]. MPNs

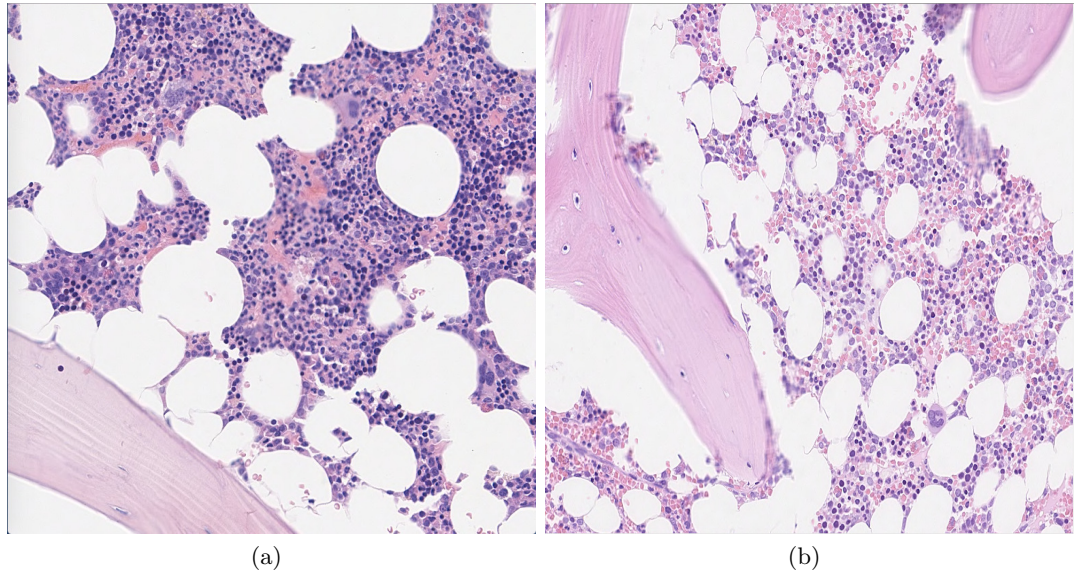


Figure 1.3: Visual examples of BM trephine biopsies (10 \times). Trephine biopsy allows the evaluation of the bone marrow's overall cellularity. In above sample images, there are three main components: bone trabeculae with pink texture, adipocytes with white circle areas, and other type of cells including megakaryocytes, erythroid cells and myeloid cells.

were originally labeled as myeloproliferative disorders by Dr. William Dameshek in 1951. In 2008, World Health Organization (WHO) guidelines classified MPNs based on shared molecular and genetic abnormalities and similar clinical and BM histologic findings. Classic MPNs consist of four main different subtypes: chronic myelogenous leukemia (CML), polycythemia vera (PV), essential thrombocythemia (ET) and primary myelofibrosis (PMF) [1, 6, 13, 18]. CML comes from an acquired translocation known as the BCR-ABL gene fusion, also called Philadelphia chromosome, and can be efficiently diagnosed by detecting this hybrid oncogene. The rest of subtypes of MPNs are also called BCR-ABL-negative MPNs or Philadelphia-chromosome-negative (Ph-negative) MPNs. Here I use the term MPNs to mean Ph-negative MPNs in the thesis.

1.1.1 Subtypes of MPNs

MPNs arise from precursors of the myeloid lineages in the BM and have similar clinical symptoms and physiological responses [6]. Here I briefly describe three main subtypes of MPNs (Ph-negative MPNs) as follows [13]:

1. PV is characterized by neoplastic proliferation and overproduction of red blood cells, white blood cells and platelets. It commonly occurs over the age of 60. The annual incidence rates of PV range from 0.01 to 2.61 per 100,000 population [19]. PV patients are prone to the development of blood clots and then commonly have pruritus, itching or peptic ulcer.

2. ET is a blood malignancy that is characterized by the overproduction of platelets by megakaryocytes in the bone marrow. It usually occurs over the age of 50, but up to 20% of patients are diagnosed at less than 40 years of age [13]. The range of incidence rate is approximately 0.21 to 2.27 cases per 100,000 persons per year [19]. The common symptoms in ET patients are bleeding, blood clots, headache, and so on.

3. PMF is a chronic blood cancer in which the proliferation of an abnormal clone of hematopoietic stem cells in the BM and other sites results in fibrosis, or the replacement of the marrow with scar tissue. The term primary means that the disease is of spontaneous origin. PMF commonly occurs over the age of 60 with an annual rate of 0.22 to 0.99 per 100,000 persons per year [19]. In patients with PMF, the hematopoietic tissue is replaced by the fibrosis to impair the patient's ability to generate new blood cells and the spleen mainly bears hematopoietic function of BM to become abnormal massive enlargement.

These three main subtypes of MPNs usually have similar clinical responses, such as enlarged spleen or anemia, and might develop into other subtypes of MPNs or other BM cancers, like acute myeloid leukemia (AML). For efficiently and precisely differentiating between these subtypes of MPNs, the WHO established criteria of

disease classification for MPNs derived from clinical investigation and symptoms to help pathologists make correct diagnosis and treatment.

1.1.2 WHO criteria of MPNs

The above list of MPNs exhibits a varied but partially overlapping set of clinical and cytomorphological features. This inevitably makes the task of objectively classifying a bone marrow trephine biopsy sample into one of the above MPN diseases quite challenging in some cases [1, 6, 13, 18, 20, 21]. In order to create a standard set of pathological measurements that aid in distinguishing the three subtypes of MPNs in routine clinical diagnosis, the WHO has established a set of diagnostic guidelines to associate clinical diagnostic data with observed histological and cytological features and molecular-genetic findings [1, 13, 20, 21]. In 2001, WHO classification proposed the definition and diagnostic guideline of MPNs, and it reviewed and modified this MPN diagnosis document according to recent clinical and scientific investigations in 2008. Table 1.1 gives the current improved criteria of distinguishing among the three MPNs [1].

Based on this table of revised WHO criteria of MPNs, these criteria show that several genetic and histologic features of the marrow can be ascertained with reasonable reproducibility, specifically those associated with marrow topography, cellularity, and degree of fibrosis for diagnosing these subtypes of MPNs [22–25]. For instance, the fluorescence in situ hybridization is used to perform BCR-ABL gene fusion for diagnosing the CML, which is a type of Ph-positive MPN, but can not provide significant information to distinguish subtypes of Ph-negative MPNs [26, 27]. The mutation Janus kinase (JAK2) V617F, which is cytoplasmic tyrosine kinase signal transducer in controlling production of blood cells from hematopoietic stem cells, is the most important feature to efficiently and precisely help the pathologists distinguish PV from MPNs. Moreover, the reticulin, also called reticular fibers, is another clear significant features to identify PMF and it often appears in the late

Table 1.1: World Health Organization (WHO) diagnostic criteria for PV, ET and PMF [1].

| WHO Diagnostic Criteria | PV | ET | PMF |
|-------------------------|--|--|--|
| Major | <ol style="list-style-type: none"> hemoglobin >18.5 g/dL (men) >16.5 g/dL (women) Presence of JAK2V617F or JAK2 exon 12 mutation | <ol style="list-style-type: none"> Platelet count $\geq 450 \times 10^9/L$ Megakaryocyte proliferation with large and mature morphology Not meeting WHO criteria for CML, PV, MDS, or other myeloid neoplasms Demonstration of JAK2V617F or other clonal marker or no evidence of reactive thrombocytosis | <ol style="list-style-type: none"> Megakaryocyte proliferation and atypia accompanied by either reticulin and/or collagen fibrosis Not meeting WHO criteria for CML, PV, MDS, or other myeloid neoplasms Demonstration of JAK2V617F or other clonal marker or no evidence of reactive marrow fibrosis |
| Minor | <ol style="list-style-type: none"> BM trilineage myeloproliferation Subnormal serum erythropoietin level Endogenous erythroid colony (EEC) growth | | <ol style="list-style-type: none"> Leukoerythroblastosis Increased serum LDH level Anemia Palpable splenomegaly |

stages of PMF. Although JAK2 examination and reticulin are used to efficiently discriminate PV and PMF, for accurate diagnosis, the general routine diagnosis of these diseases needs to follow the WHO diagnostic criteria of MPNs. Patients are diagnosed with PV if they present with both major criteria and 1 minor criterion or the first major criterion and 2 minor criteria. ET patients are diagnosed by meeting all 4 major criteria, and the clinical symptoms of PMF patients need to match all 3 major criteria and 2 minor criteria. Although it seems like these diagnostic criteria are crucial to identify the corresponding subtypes of MPNs, most of these criteria cannot provide concrete and precise diagnosis of MPNs. For instance, ET has heterogeneous properties that overlap with PMF that could make diagnosis somewhat difficult [13, 20]. In order to resolve this problem, computer techniques can be introduced to develop an automatic system applied on pathology images. Comparing with manual routine assessment that is labor intensive and time consuming, automated approaches provide fast and reproducible measurement and analysis and efficiently reduce the inter-observer variations due to the complex nature of pathology images.

1.2 Digital Pathology

The investigation of diseases, especially cancers, is the major topic in pathological science. In recent years, the discipline of pathology has gradually shifted from understanding single parts of larger pathological images to understanding complex systems at the cellular and molecular levels. Understanding complexity of pathological images is a difficult task because it requires acquisition, analysis and sharing of large and high-dimensional image datasets. Manually processing and analyzing large amounts of pathological images is usually infeasible. Moreover, manual work due to subjective assessment is prone to human error. For solving these problems, digital pathology (DP) is rapidly gaining momentum due to the advanced development

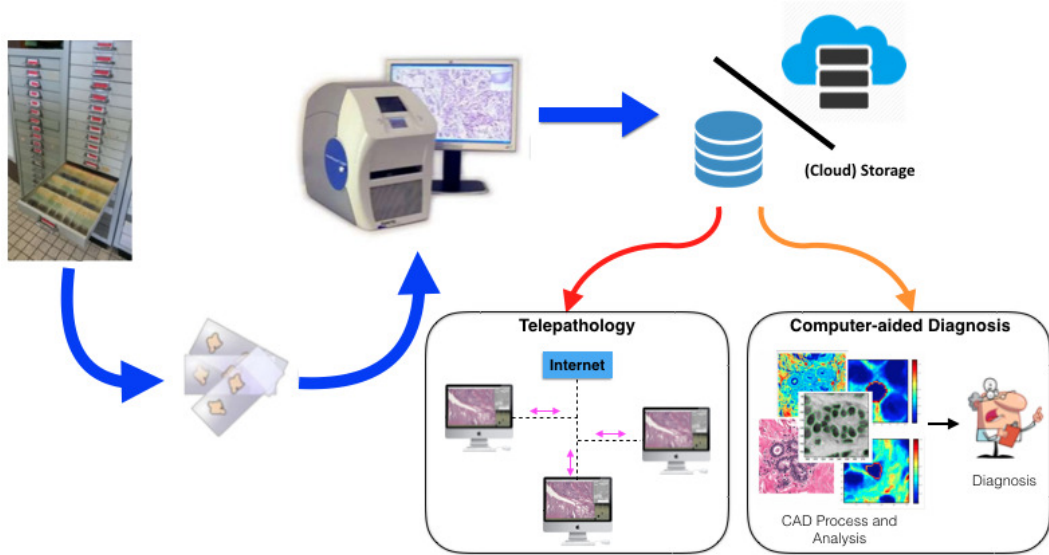


Figure 1.4: The workflow of digital pathology for disease diagnosis. Clinical slides are scanned and digitized to get high-resolution whole slide images. These digital images are easily stored into and accessed from any storage device, such as cloud storage. The pathologists can immediately share and discuss digital slides even if they do not sit together. Moreover, digital slides can be investigated and analyzed by computer-aided techniques for helping disease diagnosis [7–11].

of computer techniques and algorithms in hardware and software. The automated computer-aided diagnosis (CAD) system can play an important role in DP and gradually takes the place of conventional manual process and analysis for pathological images on a large scale [28, 29]. CAD systems can efficiently reduce laboratory expenses, improve operational efficiency, and enhance productivity, reproducibility and objectivity in the diagnostic process. Fig. 1.4 shows general processing steps from digitizing histology slides to clinical applications and CAD implementations.

In CAD systems, image processing and analysis become a key component for discriminating the types of diseases and are widely used to study cancer gene expression, genetic progression and cellular morphology for strengthening the ability of cancer diagnosis and treatment. Also, they provide an opportunity for investigating morphological and cellular characteristics in different stages of diseases, especially early stage of diseases or cancers. In general, if a certain disease or cancer, such as

breast cancer or colorectal cancer, can be diagnosed in early stage, the patients will live longer or benefit from getting efficient and precise treatments. However, it is difficult to differentiate some types of diseases/cancers in early stage that have similar pathological and morphological symptoms and it is necessary to have efficient and robust criteria for the diagnosis of those diseases. For instance, for the subtypes of MPNs in bone marrow, which is the main types of cancers studied in this thesis, there does not exist a standard and approved criteria of diagnosis. By developing advanced computer techniques and algorithms, we may find potential clues to construct and improve current diagnostic criteria to assist pathologists making an accurate diagnosis for efficient therapies.

1.3 Motivation

According to the WHO diagnosis criteria, JAK2 mutation and reticulin can efficiently identify PV and PMF from MPNs. The examination of JAK2 mutation is the routine step of diagnosing subtypes of MPNs, and reticulin is only observed in BM trephine biopsy. However, in general, the reticulin clearly appears when PMF is in late stage. In early stage of PMF, the reticulin is unclear or does not exist. It means that PMF without reticulin, called prefibrotic PMF, cannot efficiently help pathologists precisely distinguish PMF. In [13], it was found that approximately 40%-50% of patients with ET in fact have PMF. Fig. 1.5 shows that it is difficult to differentiate the histology images in ET and prefibrotic PMF. It is because prefibrotic PMF and ET have overlapping clinical symptoms and morphological features. In addition, according to WHO disease category, including the distinction between prefibrotic PMF and true ET, the assessment of cytological features is much less reliable and it is difficult to have good reproducibility of distinguishing these subtypes of MPNs in routine diagnostic practice for hematopathologists, even experienced ones. In other words, the current WHO histologic criteria are not

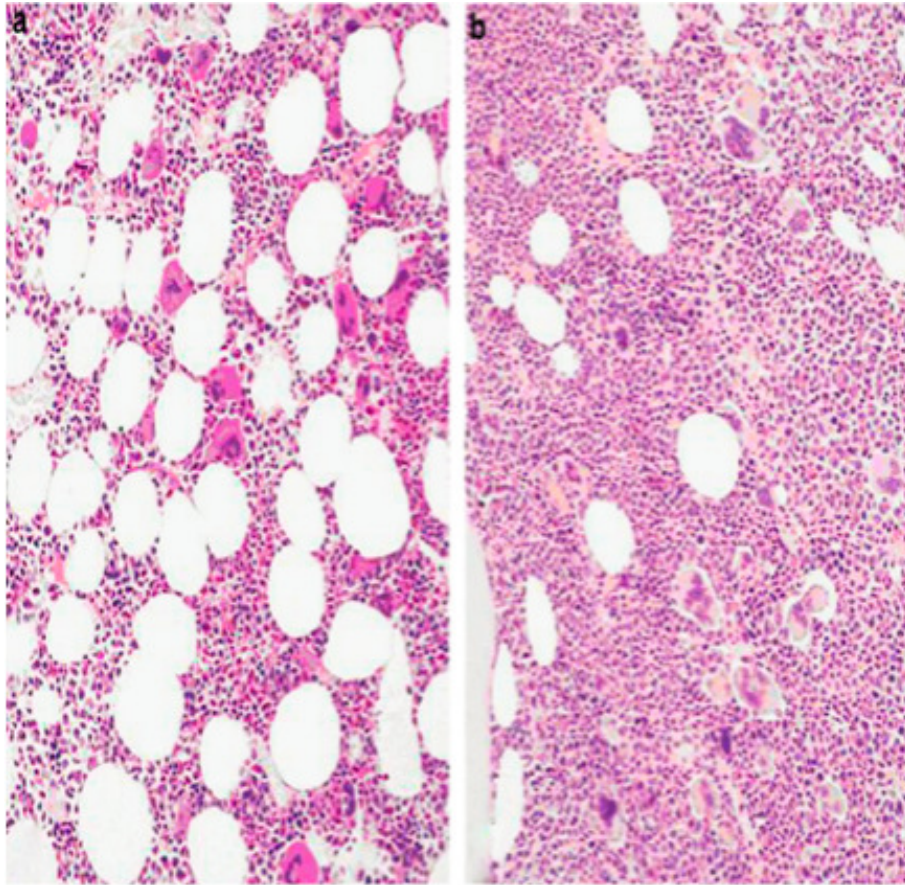


Figure 1.5: Examples of ET and pre-fibrotic PMF [12]. The left case belongs to ET, and the other one is pre-fibrotic PMF. There are no obvious morphological characteristics or cytological architecture to distinguish between them and pathologists have low agreement of identifying these two bone marrow diseases. In the study [13], it also mentions that many patients with pre-fibrotic PMF are diagnosed with ET because of unclear and ambiguous diagnostic features.

sufficiently robust to define ET and pre-fibrotic PMF. There is poor inter-observer agreement on what is represented by the terms pre-fibrotic PMF and true ET, and there are striking differences in the emphasis each of the hematopathologists placed on different morphologic criteria when arriving at a diagnosis. It causes there is no standard or obvious priority of diagnostic criteria and pathologists use their own experience of diagnosing these two types of disorders resulting in subjective identification [13]. In order to collect more potential histology information for finding efficient diagnostic features of these two subtypes of MPNs, I adopt trephine biopsy

examination that is one of the bone marrow examinations and allows a complete assessment of bone marrow structure and of the pattern of distribution of any abnormal infiltrate [6, 13, 18]. Here the staining protocol used in trephine histology, namely Hematoxylin and Eosin (H&E) staining, is fairly standard protocol that is used worldwide. Although a BM core biopsy may not be required in every case, an adequate biopsy does provide the most accurate assessment of the marrow cellularity, topography, stromal changes, and maturation pattern of the hematopoietic lineages, and it can be invaluable in detecting residual disease following therapy. If marrow aspirate smears are poorly cellular, the trephine biopsy provides material for detecting, diagnosing and monitoring a number of diseases and conditions that can affect the bone marrow and blood cell production [1,6,13,18]. Moreover, ET and PMF have the risk of mutation and convert to other types of bone marrow cancer, like AML. For patient survival and health, early diagnosis of these two diseases is necessary, and trephine biopsy processing and analysis have attracted our attention for improving the WHO diagnosis guidelines and looking for potential clues that have never been discovered.

In order to objectively and efficiently obtain cellular morphological and histologic information for advanced investigation of ET and prefibrotic PMF, I propose automated advanced computer techniques to ultimately help the pathologists establish a suitable and robust model to potentially extract more cellular and morphological features. I can then provide these features to pathologists looking for or improving current diagnostic criteria for more efficient and precise diagnosis and treatment. Moreover, computer-aided approaches are much more useful to facilitate quantitative analysis of hematopathological images and the discovery of unidentified prognostic morphological features. The characteristic outcomes of quantitative analysis through these automated methods are more reliable and objective in disease progression evaluation and diagnostic decision.

In this thesis, I concentrate on developing specific algorithms for extract-

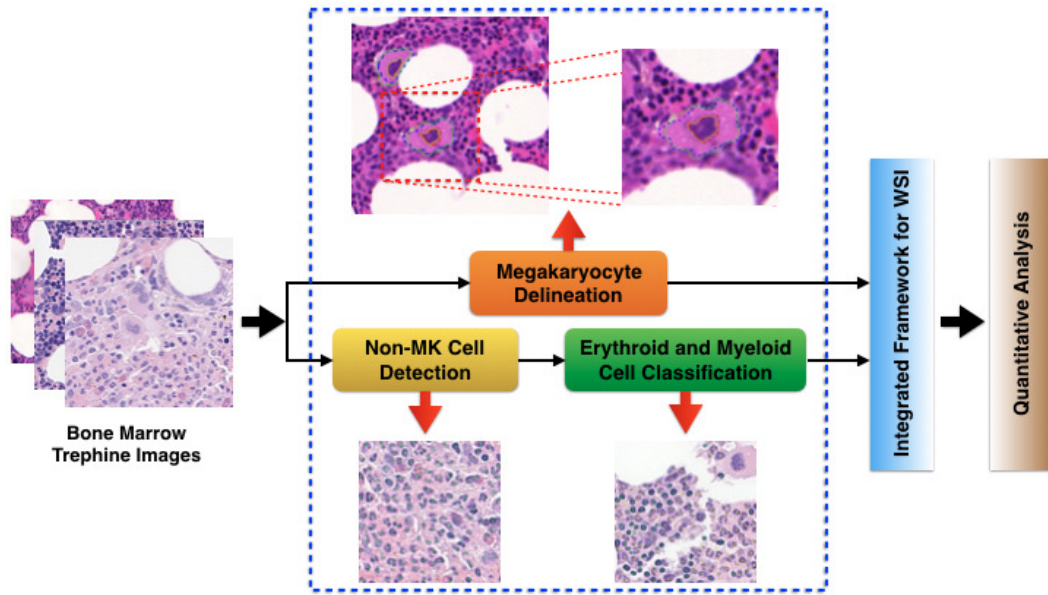


Figure 1.6: The diagram of research objectives. According to the aims of thesis, the final framework will automatically do quantitative analysis of BM trephine biopsies and provide the statistical information to help the pathologists improve the accuracy of distinguishing ET and prefibrotic PMF. There three major sections (in blue-dash rectangle) to construct the proposed final framework: megakaryocyte delineation, non-MK cell detection, and classification of erythroid and myeloid cells.

ing cytological morphological features and geographic distribution of all types of hematopoietic stem cells in BM trephine biopsy for further investigation and analysis. As shown in Table 1.1, quantitative measurements of megakaryocyte (MK) cellularity, the ratio between types of BM cells, and the distribution of MK are considered to improve the current criteria and help the pathologists make more precise decision of diagnosis and therapies of ET and prefibrotic PMF [30–33].

1.4 Aims and Objectives of the Thesis

This thesis seeks to ultimately assist the pathologists to look for efficient histopathological characteristics to distinguish between the subtypes of MPNs, especially ET and prefibrotic PMF, by extracting and analyzing cellular morphological features and geographic distribution from BM trephine biopsies. Fig. 1.6 shows the research

objectives of this thesis. In order to achieve the aims, I will construct the proposed framework to take into account BM trephine whole slide images (WSIs) and do quantitative analysis of BM trephine data. There are several important research objectives:

1. For automatically delineating MK, I will adopt unsupervised methods and active contour models to construct a proposed framework.

2. In order to detect all non-MK hematopoietic stem cells, I would like to use deep learning approaches and various shape models to efficiently identify the center of any types of BM cell.

3. For classifying erythroid and myeloid cells, machine learning and deep learning methods will be used.

I will compare these proposed approaches with current and state-of-art corresponding approaches by evaluating the performance of the results to make sure that the proposed methods are accomplished. After building above three major components, I integrate all of them to construct a framework working on BM trephine WSIs and collect more image data and their ground truth images for further quantitative analysis. These three proposed methods will take at least 1 year to be designed and accomplished, and then I will spend 1 to 2 months to build the final framework for further quantitative analysis.

1.5 Main Contributions

According to research objectives, the accomplished major contributions are described as below:

1. I propose an automated framework with a novel dual-channel active contour model for delineating MK cells with weak shape feature (Chapter 3).

2. I propose a novel hybrid deep learning network to reconstruct the topological features for nuclear detection. I use a curve-support Gaussian-based model to rep-

resent the location of nuclear/cell centers and emphasize the ability of detecting irregular shapes of nuclei/cells (Chapter 4).

3. I design a synchronized asymmetric deep learning network to take into account detection and classification strategies at the same time. The proposed network can efficiently reduce time required for training and maintain the accuracy of detection and classification performance (Chapter 5).

1.6 Thesis Organization

Chapter 2: Literature Review. It contains a brief review of current studies on histology image challenges and corresponding solutions. It also describes the concepts and principles of popular image processing approaches and application in histopathology images.

Chapter 3: A dual-channel active contour model. This chapter proposes an image-processing framework with a novel segmentation approach for delineating a very specific type of cell from a heterogeneous histopathology image microenvironment with poor morphological characteristics.

Chapter 4: A hybrid deep learning approach for cell/nuclei detection. I propose a novel deep learning neural network with a Gaussian-based topological model to efficiently detect all types of cells, including irregular-shape nuclei/cells, in BM trephine images.

Chapter 5: A synchronized asymmetric hybrid deep learning network for detection and classification. I propose a novel parallel structure of deep learning network by using the concepts of asymmetric learning method to process detection and classification stages simultaneously and efficiently reduce the training time of learning network.

Chapter 6: Conclusions and future directions. Finally, in this chapter, I conclude the thesis, discuss possible application of the work and future research directions.

Chapter 2

Literature Review

Histopathology is an important area of clinical medicine that studies the cell anatomy and tissues of human at a microscopic level. In the current practice of medicine, histology specimens are analyzed to identify normal and abnormal biological structures, morphological and architectural characteristics of cytology or tissue, and they play one of the most significant roles in therapeutic decision making for routine clinical disease diagnosis like cancer. They are also used to analyze anatomy of cells and tissues, which could be identified by pathologists depending on their experience. But some structures are quite small with respect to tissue region, and relevant patterns generally have high visual appearance variability. In addition, manually identifying and interpreting the tumor or abnormal tissue in histology slides is tedious, time-consuming, and in some cases, an error-prone procedure, and requires a lot of skill and experience. Recently, according to the development of computer techniques and approaches, CAD can play an important role in biomedical and clinical diagnosis, analysis and investigation. In general, the automated techniques of CAD also have the capacity to not only significantly reduce the laborious and tedious nature of providing accurate quantification but to act as a reviewer helping to reduce large inter-observer variability among pathologists [34]. Moreover, automated computer approaches can greatly reduce the subjective bias and provide efficient and accurate

characterization of diseases [35]. Many computational algorithms or methods exist and take advantage of the increasing assortment of biomedical images [28, 29, 36]. However, histology image analysis is a specific research field in digital image processing and there are many challenges and limitations to customize traditional image processing methods for different types of histology images. In order to resolve these problems, there are many recent automated computer approaches developed for efficiently and precisely extracting quantitative data from images.

In this chapter, I would like to describe the challenges in various aspects of histology image processing steps and briefly review current researches for addressing these challenges in histology images in Section 2.1. Also, I introduce the concepts and advanced applications of popular and state-of-the-art image processing approaches on histology images in Section 2.2.

2.1 Problems in Histology Image Analysis

According to the development of computer technique, the investigation and analysis of histology become more important and employ a key role in cancer research and diagnosis. Also, digital high-resolution histology images are easily obtained and provide an opportunity of observing and capturing cellular information in histology microenvironment. However, there are various factors influencing the automated image processing approaches and the accuracy of outcomes in quantitative analysis. For example, histological samples contain large numbers of cells and other structures that are widely and unevenly distributed and surrounded by many different types of tissue and make complicated features, such as color, light, texture or inner structures [37, 38]. In Fig. 2.1, we can observe these sample cases and found the complicated and various architecture of tissue and cells. Moreover, the different conditions of histology image acquisition process, including sampling, cutting, staining, and digitalizing, cause high visual variability of nuclear or cell representation.

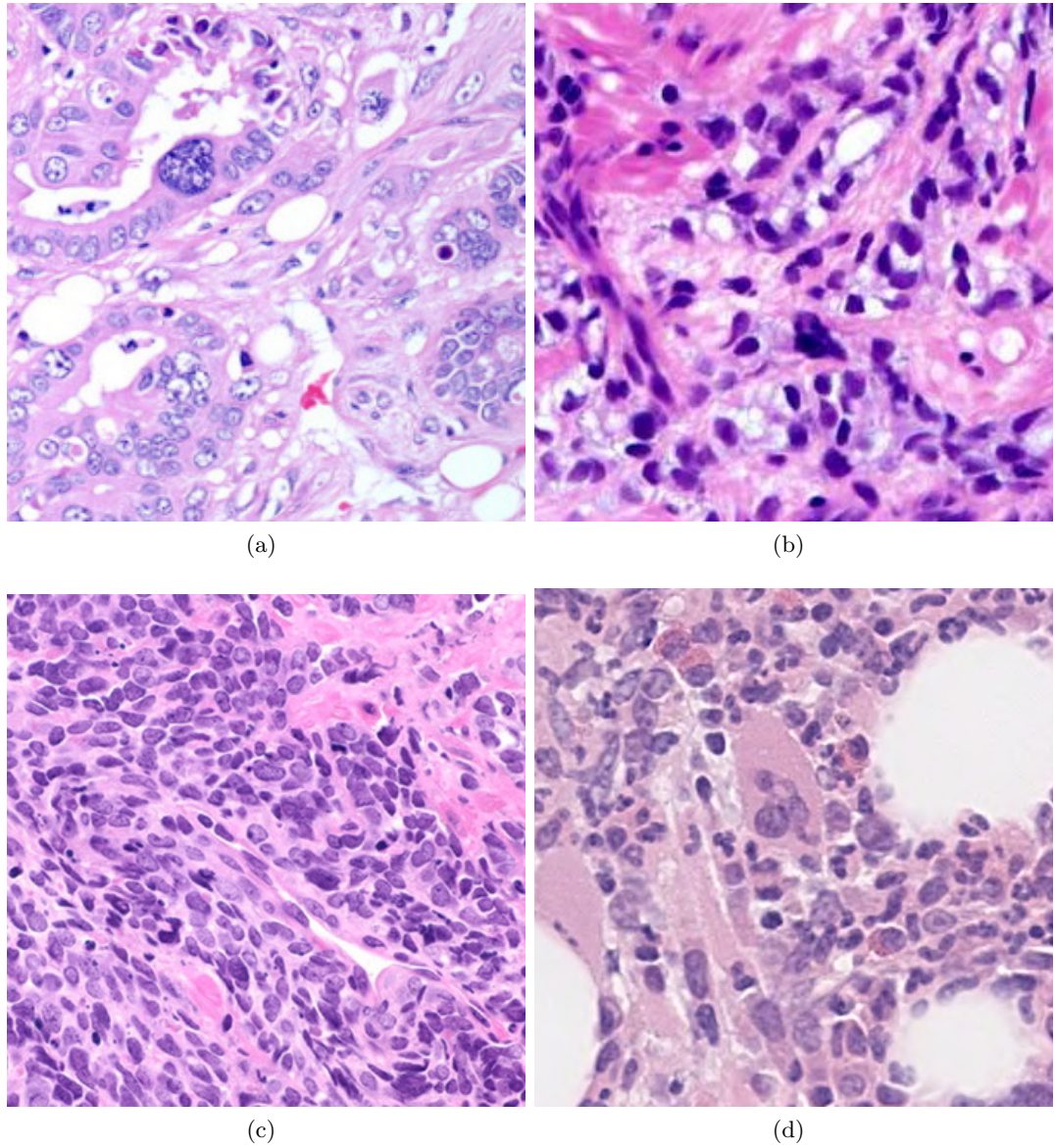


Figure 2.1: Examples of histology images in different cancer tissue: (a) Breast (b) Prostate (c) Lung and (d) Bone marrow. We observe the various types of cells with complicated morphological features in each case. These massive variations show that computer-aided methods face difficulty in obtaining accurate and specific histology and cellularity information.

These factors increase the difficulty of histology image processing and analysis for automated approaches or models.

In H&E histology images, color variation has become more of an issue. Typically, two or three different colored stains are used to highlight cellular and subcellular target components. If the stain color in each histology sample become stable and is normalized, the ability and performance of automated methods will efficiently improve and increase the robustness of outcomes. In order to reduce the influence of these various factors, color or stain normalization in pre-processing step is necessary. There are several stain normalization approaches that are usually used. For instance, Reinhard *et al.* [39] proposed a color normalization method where the mean and standard deviation of each channel of the image are matched to that of the target image by means of a set of linear transforms in Lab color space. Moreover, Magee *et al.* [40] and Macenko *et al.* [41] proposed stain normalization methods based on a color deconvolution (CD)-derived representation. CD method uses the given stain matrix to obtain stain concentration values and describes how the color is affected by the stain concentration. The difference is that Magee *et al.* [40] used a supervised pixel classification-based approach to estimate stain colors, whereas Macenko *et al.* [41] used an singular value decomposition (SVD)-based approach to directly estimate the stain matrices. Recently, Khan *et al.* [42] proposed a nonlinear mapping with stain color descriptor (SCD) to efficiently take into account stain normalization for reducing the influence of color variation.

After introducing above pre-processing approaches, I would like to focus on the major procedure of digital image analysis: detection, segmentation and classification. These strategies are main steps and widely used to extract and identify the features and types of cells [29]. However, these strategies have difficult and different computer vision problems due to high variability in histopathology images. I would like to describe the limitations and challenges and provide recent research methods to tackle these problems by designing for specific tasks in histology images.

2.1.1 Segmentation

Nuclei or cell segmentation is necessary and one of the main functional components in a fully automated histology image investigation and analysis [43, 44]. It aims to separate individual nuclei and cells with delineating their boundaries and to obtain extracted histology information and features for various quantitative analysis, which includes to calculate cellular morphology, such as size, shape, texture, and other intensity information of segmented nuclei or cells. The simplest way to segment nuclei or cells in histopathological images is based on thresholding and morphological operations [45–47]. This methodology actually suffers from its simplicity by including little object knowledge. In addition, it lacks robustness on size and shape variations, as well as on texture variations, which are very frequent in histopathological images. Watershed transform is one of the popular region accumulation methods, which floods the landscape with water from regional minima, such as seed points, with the intensity representing the elevation to create labeled regions [29, 48, 49]. Wahlby *et al.* [50] used this method to segment clustered nuclei and proposed a methodology that combined the intensity and gradient information along with shape parameters for improved segmentation. However, it requires the prior detection of seed points. The edge map and distance transform are used for seed detection [50, 51]. The reported results are suboptimal for ring-shaped nuclei having clear homogeneous regions. Furthermore, the watershed transform does not include any prior knowledge to improve its robustness. In addition, since a regional minimum corresponds to an object, the watershed transform usually leads to oversegmentation.

In addition, clustering is to group a collection of objects into subsets or clusters, such that those within each cluster are closely related to one another than objects assigned to different clusters [52]. For instance, Arif *et al.* [53] have formulated nuclei segmentation as manifold learning-based shape classification on prostate histology images, which segment nuclei or nucleus clumps with K-means cluster-

ing. Expectation-maximization (EM) algorithm [54], which is originally designed for maximum likelihood estimation, can be used to conduct cluster analysis with soft assignment. Jung *et al.* [55] have presented an EM-based automated nucleus segmentation approach in mammary invasive ductal carcinomas and cervical images. Moreover, supervised classification techniques have also been used for nucleus or cell segmentation. Janssens *et al.* [56] have applied a multi-class support vector machine (SVM) classifier to cell segmentation on H&E stained skeletal muscle images. Besides, Dalle *et al.* [57] proposed gradient in polar space (GiPS), a novel nuclei segmentation method. Initially, nuclei are detected using thresholding and morphological operations. Then, transformation into polar coordinate system is performed for every patch with the center of mass of the nucleus as the origin. Finally, a biquadratic filtering is used to produce a gradient image from which nuclei boundaries are delineated.

Active contour (AC) models can combine both shape characteristics, which consist of smoothness and shape model, with image features, such as image gradient and intensity distribution. However, the resulting segmentation is strongly dependent upon the initial seed points. Cosatto *et al.* [58] described an automated method for accurately and robustly measuring the size of neoplastic nuclei and providing an objective basis for pleomorphic grading. First, a difference of Gaussian (DoG) filter is used to detect nuclei. Then, the Hough transform is used to pick up radially symmetric shapes. Finally, an AC model with shape, texture, and fitness parameters is used to extract nuclei boundaries. Huang and Lai [24] proposed watershed and AC-based framework for nuclei segmentation in hepatocellular carcinoma biopsy images. Initially, a dual morphological gray-scale reconstruction method is employed to remove noise and accentuate the shapes of nuclei. Then, a marker-controlled watershed transform is performed to find the edges of nuclei. Finally, AC model is applied to generate smooth and accurate contours for nuclei. This framework achieves poor segmentation in case of low contrast, noisy background, and irregular

nuclei.

However, in histopathology imagery, it is difficult to achieve robust and accurate nuclei and cell segmentation because there are a number of various factors, such as nuclei type and malignancy of the disease, heterogeneous chromatin distribution and irregular boundaries. In addition, nuclei and cells are often clustered into clumps so that they might partially overlap with one another. These variations seriously affect the ability of computer algorithms to separate overlapped or clumped nuclei and cells and to cause segmentation problems. The results of segmentation also make serious influence of detection and classification in further analysis and investigation. In order to address these problems, there are many advanced segmentation methods derived from above approaches to improve the performance of nuclei or cell segmentation. In general, an advanced segmentation approach may combine some of these algorithms as well as other methods. As compared with nuclei segmentation methods, these methods are more tolerant to variations in shape of nuclei, partial occlusion, and differences of the staining. For instance, a variety of approaches using curvature information have been investigated to separate the overlapped nuclei [59–61]. However, most of these methods are highly dependent on the concavity, and thus it is difficult to obtain robust segmentation results when the concave points are not detected correctly [59, 60]. The watershed algorithm usually collaborates with detection methods and extends to form the marker-controlled watershed technique. Cloppet and Boucher [62] presented a scheme for segmentation of overlapping nuclei in immunofluorescence images by providing a specific set of markers to the watershed algorithm. Other marker-controlled watershed segmentation methods use gradient information, such as nuclei segmentation in H&E stained histopathology images [63] and H&E stained cytology images [64].

AC models are also used to take into account overlapping problems by collaborating with other methods or adding more morphological or texture information. For instance, Fatakdaawala *et al.* [65] proposed EM-driven Geodesic AC model

with overlap resolution for segmentation of lymphocyte nuclei in breast cancer histopathology. EM-based AC model initialization allows the model to focus on relevant objects of interest. Mouelhi *et al.* [66] proposed a modified GAC with the Chan-Vese (CV) energy model with concavity points and watershed transform to segment clustered nuclei in breast cancer histopathology. Moreover, Kulikova *et al.* [67] proposed a method based on marked point processes (MPPs), which is a type of high-order AC model, to segment overlapping nuclei as several individual objects. There is no need to initialize the process with seed points giving the location of the nuclei to be segmented. A shape prior term is used for handling overlapping nuclei.

Some classifiers are also used to take into account nuclei and cell segmentation with overlapping problem. For instance, EM- and Gaussian mixture model (GMM)-based unsupervised Bayesian classification scheme was used for segmentation of overlapping nuclei in IHC images [68]. This approach primarily involves applying the distance transform to generate topographic surface, which is viewed as a mixture of Gaussian. Then, a parametric EM algorithm is employed to learn the distribution of topographic surface (GMM) for separating overlapping nuclei. In addition, machine learning (ML) approaches are also widely used and applied in segmentation. For instance, Jung *et al.* [68] used Bayesian model and estimate cell topographic surface to take into overlapped and clumped nuclei in segmentation strategy. Recently, deep learning (DL) approaches make significant progress in learning image representations and there are some DL models proposed for nuclei or cell segmentation. Ronneberger *et al.* proposed U-net [69], which is based on full convolution network (FCN), to segment glioblastoma-astrocytoma U373 cells. In addition, Song *et al.* [70] proposed a multi-scale convolutional network to segment cervical nuclei and cytoplasm.

2.1.2 Detection

Nuclei or cell detection is viewed as obtaining the object location without accurately delineating the boundaries, and it is usually referred to as a marker or a seed seeking

near the object centroids. The marker can be a single point or a small region inside the object and provide support for nucleus/cell counting, tracking, and segmentation. In general, automatic detection in histopathology images is a very challenging task for several reasons. It is because there are amount of different types or subtypes of cells characterized by a large variety of shape configurations, which are related to the high variation of biological structures, such as mitosis cells in breast cancer diagnosis. In addition, clustering cells usually appear touching or overlapping cells and have similar morphological appearance, resulting in lots of false negatives in the detection process. In order to address these challenges, many automatic cell detection algorithms are proposed and based on nuclear or cellular hand-crafted features, such as color intensity and texture information. Sometimes the procedure of a marker detection method might combine several algorithms or segmentation methods for specific nuclei or cell detection. These detection approaches are widely applied in routine H&E histological images to identify nuclei and perform high degrees of detection accuracy under certain circumstances. For instance, binary morphological filtering is a technique processing the images with a certain structure element, such as circular disk, square, cross, and so on [71]. It performs image filtering by examining the geometrical and topological structures of objects with a predefined shape. Yang *et al.* [72] have presented a conditional erosion method to detect nucleus markers in fluorescence microscopy images. Distance transform is another sample method to assign each pixel with the distance to the nearest feature point [73]. In nucleus and cell detection, the feature points are usually selected as the edge pixels in a binary image and Euclidean distance is chosen as the metric. Therefore, ideally the local maxima in the generated distance map correspond to the centroids of nuclei or cells. Adiga *et al.* [74] have exploited a distance transform to detect nucleus centers in breast cancer histopathological images. However, Euclidean distance transform is only effective on regular shapes in a binary image, and small variations on the edge pixels will result in false local maxima. Therefore, it might fail to detect overlapping

nuclei or cells. The maximally stable extremal region (MSER) detector [75] is also used to locate blob objects. Similar to the procedure that applying an increasing intensity threshold to a gray-level image, it generates a set of nested extremal regions based on the level sets in the intensity landscape and considers one region to be stable using a local intensity minimum based criterion. Lu *et al.* [76] have applied this strategy to nucleus detection in Pap smear microscopy images. Metas *et al.* used a MSER detector to detect each isolated nucleus [77]. In [78], the algorithm heavily depends on the quality of MSER detector that does not take advantage the prior cell shape information and the performance will deteriorate when the cells overlap with one another.

Moreover, the Laplacian of Gaussian (LoG) filter is one of most popular methods to identify small blob objects, which usually correspond to the central regions of nuclei or cells in histology images. Byun *et al.* [79] have successfully applied a LoG filter with a specified scale to nucleus locating on retinal images, but this method assumes that the object size is known a priori. Later, the scale-normalized LoG filter [80] is used to detect cells on phase-contrast microscopy images [81, 82]; nevertheless, it might fail in touching or overlapping objects which exhibit weak boundaries. To tackle this issue, Al-Kofahi *et al.* [83] have introduced a multi-scale LoG filter constrained by a Euclidean distance map to detect nuclei in histopathology images. Parvin *et al.* [84] proposed an iterative voting algorithm based on oriented kernels to localize cell centers, in which the voting direction and areas were dynamically updated within each iteration. However, in general, the above detection approaches have some limitations. For example, both [84] and [85] are sensitive to the selection of proper cell diameter parameters. However, finding an appropriate parameter that works under all conditions is extremely difficult when the cells exhibit large size variations.

Since nuclei usually exhibit circular or elliptical shapes in pathological images, Hough transform [86, 87] based nucleus detection and radial symmetry trans-

form [88, 89] have attracted many research interests of centroids of nuclei or cells. Ramesh *et al.* [89] have first thresholded the hematopoietic cell regions in bone marrow images, and then applied the circular Hough transform to hematopoietic cell detection. Cossatto *et al.* proposed the method which uses difference of Gaussian (DoG) and Hough transform to find symmetrical shapes to detect cells [90]. However, the Hough transform might generate false peaks due to image noise, incorrect edge extraction, or touching objects. Meanwhile, radial symmetry based voting in practical applications is limited by the high computational complexity. In order to resolve these problems, Loy and Zelinsky [91] have proposed a fast radial symmetry transform (FRST) to significantly decrease the time cost. Veta *et al.* [63] have applied the FRST to nucleus detection in H&E stained breast cancer images. However, the FRST might produce false peaks in the transformed image due to clustered nuclei, and the radius range needs careful selection to handle nucleus scale variations. In addition, many nuclei or cells exhibit elliptical but not circular shapes. These irregular shape nuclei or cells present significant challenges for the FRST. Additionally, there are several approaches proposed to detect the seed points. For instance, Qi *et al.* proposed a single-pass voting to vote the centers of nuclei by applying the mean-shift clustering [92].

In recent years, DL methods also used successfully for nuclei and cell detection. For instance, Cireşan *et al.* [93] used convolutional neural network (CNN) to detect mitosis in breast cancer histology images. Xie *et al.* [94] proposed structural regression CNN capable of learning a proximity map of nuclei for providing more accurate detection results. Sirinukunwattana *et al.* [95] used CNNs with local spatial features for identifying the position of nuclear center but the performance of this method was found to be limited when detecting long-tailed or irregular-shape nuclei.

2.1.3 Classification

Basically, classification depends on the ability of detection or segmentation. For nuclei or cell classification, extracting useful and accurate features is much important. If the results of detection or segmentation are worse, the outcomes of classification become more terrible. In early period of time, classifying a specific cell is based on the manual conditions setting. The users need to have some prior information of target images to identify the thresholding values or build the conditions from specific morphological or texture features of objects. For instance, Ballaro *et al.* [96] proposed a framework to identify the nuclei of megakaryocytes (MKs) by manually setting the thresholding value of nuclear size. In recent years, ML algorithms become the mainstream of classification and can improve useful computer tools to make the classification more efficient, such as principal component analysis (PCA), which can find significant correlative features to reduce the dimensionality of a dataset. For instance, Huang *et al.* [97] used SVM as a classifier with intensity, morphological and texture features to identify cancer nuclei in liver images. Vink *et al.* [98] identified nuclei by using Adaboost classifier with intensity and texture information in IHC breast images. Malon *et al.* [99] classified mitosis nuclei by using SVM with intensity features. In addition, Zhou *et al.* [100] used Markov model to classify phase identification of dynamic cell cycle behaviors of a large population of cells. However, the above classification approaches always need precise and robust feature extraction, which depends on the ability of segmentation approaches. In other words, segmentation (or detection) seriously affects the results of classification.

Recently, DL methods not only have been shown to be more efficient and robust than the classical ML approaches but can also extract the features without segmentation or detection. DL is a hierarchical learning approach that learns high-level features from pixel intensities that are useful for differentiating objects by a classifier. DL methods avoid the traditional design and computation of features

and directly exploit large numbers of unlabeled image data to capture high-level features; they are full feed-forward in terms of feature extraction [101–103]. For instance, in [104], the authors employ a convolutional neural network (CNN) with autoencoder for histopathological image representation learning. Then a softmax classification is employed for classifying regions of cancer and non-cancer. In [101], Xu *et al.* proposed a stacked sparse autoencoder (SSAE) with a softmax classifier (SMC) to classify the centers of nuclei. Sirinukunwattana *et al.* [95] used CNNs with local spatial features for identifying the position of nuclear center and classifying multiple cells in breast cancer images.

2.2 Approaches for Histology Image Analysis

After realizing the challenges of image processing strategies in histology images and related advanced computer algorithms and methods of efficiently overcoming these problems, I would like to select several important and useful approaches and introduce them. These methods will be further developed in this thesis.

2.2.1 Active Contour

Image segmentation approaches based on deformable models have been widely used to successfully delineate various structures in pathology images [29, 58, 105–107] and widely applied for tissue and nucleus segmentation for cancer diagnosis, such as breast cancer [58, 65, 105, 106, 108, 109] and prostate cancer [110, 111]. In case of nuclei or cell segmentation, the active contour (AC) model is one of the most popular nucleus or cell segmentation algorithms, since they exhibit a great trade-off between efficiency and flexibility [112]. AC model starts from a certain initial position, which is manually specified by a user or automatically detected by another algorithm, and evolves an active contour towards the object boundary by minimizing an energy functional. The AC model achieves desirable segmentation results when

the evolving contour matches the object boundary. Basically, the energy of the active contour model is formulated as a linear combination of three terms [113] and is defined using the energy function E over the contour points c as:

$$E = \oint_c (\alpha E_{Int}(c) + \beta E_{Img}(c) + \gamma E_{Ext}(c)) dc, \quad (2.1)$$

where E_{Int} controls the contour and length of the contour (internal energy), E_{Img} influences the contour to move towards features of interest (image energy) and E_{Ext} is user defined force or prior knowledge of object to control the contour (external energy), respectively. α , β and γ are empirically derived constants.

The two major implementations of deformable models for nuclei or cell segmentation are geodesic and parametric AC models, which are with implicit and explicit contour representations, respectively. The parametric model represents curves and surfaces explicitly in their parametric forms during deformation. The geometric model is based on the theory of curve evolution in time, according to intrinsic geometric measures of the image, and is numerically implemented via level set algorithms [112]. For instance, Li *et al.* [114,115] have combined a region energy and an edge energy into a level set model to segment and track cells in phase-contrast microscopy images. Recently, Xing *et al.* [116,117] have introduced a contour-based repulsive term into the balloon snake model, which belongs to the parametric model, for nucleus segmentation in pancreatic neuroendocrine tumor images.

As image segmentation methods, there are two types of AC models based on the force that evolves the contours: edge-based and region-based. In a more general context, region-based level set methods [14,118–121] have been particularly successful by incorporating region-based statistical information into an energy functional (see Fig. 2.2). Unlike edge-based level set methods, which are based on the image gradient and use edge detector output to deform the contour toward the object boundary, region-based methods use the statistical information of global region

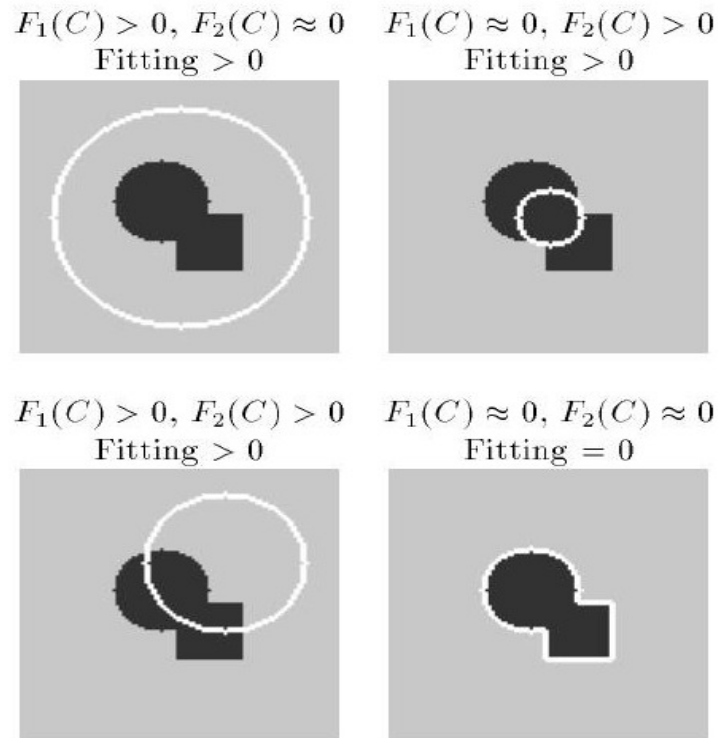


Figure 2.2: The all possible cases of region-based active contour [14, 15]. F1 energy force is generated from inside region of the contour, and F2 energy force is from outside region of the contour. If one of these two energy forces is larger than the other, the fitting energy moves the contour toward the lower energy region. If fitting energy is equal to zero, the movement of the contour will stop and fix.

to stabilize their responses to local variations. These methods have been shown to achieve higher segmentation accuracy than edge-based level set methods on images with weak boundaries. Among the state-of-the-art level set methods, the Chan-Vese (CV) model [14, 118, 122, 123] is one of the most representative and efficient ones. This particular model assumes that the image statistics in two regions remain relatively constant; these two regions are the inside and outside of the evolving contour. The CV model, therefore, performs very well on images where these two regions are relatively smooth. However, this model often leads to poor segmentation results for non-smooth images, i.e., with intensity inhomogeneities, due to the fact that the deformation movement of the evolving curve is guided by global region information [123–128].

Many improvements have been proposed to address some of the limitations of the CV model [118,122–132]. In [128], Li *et al.* propose an efficient region-based level set method by introducing a local binary fitting (LBF) energy term, which enables the extraction of local information with a Gaussian kernel and can be used on images with intensity inhomogeneities. Wang *et al.* [129] introduce the Local Chan-Vese (LCV) model, which employs both global image information and local statistics for efficiently segmenting images with intensity inhomogeneities. In [130], Zhou *et al.* combine a local active contour model and an adaptive diffusion flow active contour model to improve medical image segmentation in inhomogeneous regions with weak edges. In order to control the movement of the evolving contour towards the object’s boundary in images with intensity inhomogeneities, Ji *et al.* [131] propose an energy functional that minimizes a local likelihood energy term derived from the image intensity within each pixel’s neighborhood. Brown *et al.* [133] propose a multi-phase active contour model for global multiple region segmentation. Although all these methods improve segmentation accuracy of the CV model on images with weak edges and intensity inhomogeneities, they are all sensitive to the position of the initial contour and the value of parameters [129,132,134,135]. Based on the CV model, Zhang *et al.* [136] have proposed a coupled geodesic active contour model for cell segmentation and tracking in fluorescence microscopy images, which minimizes the overlaps between contours corresponding to touching or overlapping cells to prevent them from merging.

Within the context of cell segmentation in histology images, most of the recently proposed methods focus on nuclei segmentation as cytoplasm segmentation remains a challenging task in many types of histology images [29,106,107,137]. For instance, Ali *et al.* propose an adaptive active contour model with shape prior for nuclear segmentation in prostate cancer tissue [138]. Among the very few methods that are capable of segmenting nuclear and cytoplasmic regions, the one proposed by Nosrati *et al.* [139] uses color features of manually labeled regions to generate a

prior feature response map. This map is used along with containment and exclusion energy terms to simultaneously segment multiple regions.

2.2.2 Classical Machine Learning Approaches

Machine learning is the sub-field of computer science enables the computers to learn without being explicitly programmed [140]. In pattern recognition and computational learning theory in artificial intelligence, machine learning explores the study and construction of algorithms that can learn from and make predictions on data [141,142]. It is also employed in a range of computing tasks where designing and programming explicit algorithms is infeasible. Nowadays, several machine learning approaches are widely applied to many different types of medical images. To deal with complex histology images, supervised machine learning based methods have attracted much attention. Supervised classification technique is one of machine learning techniques aiming to infer a mapping function or model from training labeled data [47]. The nuclei and cell detection is usually formulated as a pixel or region classification problem, and a specific model is learned to assign new data examples into discrete labels. Many classifiers with various feature representations have been presented in the literature, and here I mainly focus on traditional ML methods and their applications on histology images. The deep neural networks will be introduced in the next section.

Traditionally, Support Vector Machine (SVM) is a non-probabilistic binary classifier, aiming to find a hyperplane with a maximal margin to separate high-dimensional data points [143]. Su *et al.* [144,145] have applied a binary SVM classifier to automatic nuclear detection in isolated single muscle fiber fluorescence images. Khan *et al.* [146] have presented a learning approach for mitotic cell detection in breast cancer histopathology images, which models image intensities with a Gamma-Gaussian mixture model and performs pixel-wise classification in testing images, and then generates a set of candidate regions. Finally they distinguish mi-

totic from non-mitotic cells using a SVM classifier with a set of texture features. In addition, Janssens *et al.* [56] have applied a multi-class SVM classifier to cell segmentation on H&E stained skeletal muscle images.

Random forest (RF) [147], which is derived from random decision forests and stochastic discrimination approach, is another popular ML method due to fast training and testing, and fair error tolerance in training data. For instance, Sommer *et al.* [148] constructed a hierarchical learning workflow with RF classifier for automated mitosis detection in breast cancer. In addition, other machine learning methods are also applied into different medical images. For instance, a mitotic cell detection method presented in [149] learns a discriminative dictionary with sparse representation and conducts mitosis classification based on the sparse reconstruction errors [150]; Dong *et al.* [151] have proposed a Bayesian classification based leukocyte detection algorithm on intravital microscopy images. A mitotic cell detection method presented in [149] learns a discriminative dictionary with sparse representation and conducts mitosis classification based on the sparse reconstruction errors [150]. Vink *et al.* [98] constructed a large feature set and modified Adaboost with intensity and texture information to propose an efficient nucleus detector.

2.2.3 Deep Learning Approaches

Deep learning (DL) is the major research trending of artificial intelligence and widely applied to many different fields in recent years. Different from SVM and RF that rely on hand-crafted features for object classification, deep learning (DL) exploits this idea of hierarchical explanatory factors that are higher level, more abstract concepts learned from the lower level ones. DL methods avoid traditional designing features or detectors by hands. A deep neural network hierarchically stacks multiple layers of neurons to form a hierarchical feature representation. This special structure causes DL approaches result in more efficiency and robustness to make intelligent predictions in different target databases. There are various types of deep learning

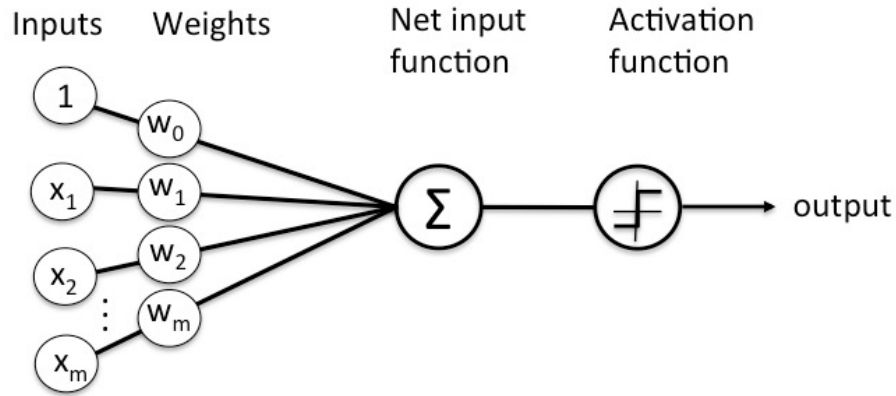


Figure 2.3: The diagram of structure of a layer of neural network. The input data are multiplied by the weights to extract the feature elements, and then feature elements are added together. The sum of feature elements is processed by an activation function to output the result.

algorithms used in research. Here I would like to introduce the theoretical concepts from simple neural network to popular state-of-the-art deep learning approaches. Also, I will mention the current applications of deep learning methods in image processing and analysis of histopathology.

2.2.3.1 Neural Networks

DL method is derived from artificial neural network (NN), which is inspired by biological nervous systems of human brain processing system. A standard artificial neural network (NN) consists of many simple, connected processors called neurons, each producing a sequence of real-valued activations. In a simple case, there may be two sets of neurons: ones that receive an input signal and ones that send an output signal (Fig. 2.3) [103, 152]. We can observe that each input signal will be processing by weights, combination operator and transfer function (also called activation function) and then produce the output. The formulation of a simple neural network is given by:

$$Y = f\left(\sum_{i=1}^N W_i x_i + b\right), \quad (2.2)$$

where $X = x_i, i = 1, 2, \dots, n$ represent the inputs to the neuron and Y represents the output. Each weight W_i times the associated input. Their sum is added by a bias b and then processed by an activation function f . According to Eq. 2.2 and Fig. 2.3, if we select a suitable transfer function and the connection of neurons, various neural networks will be constructed and trained for producing the specified outputs. Based on this concept, DL architectures are constructed with a greedy layer-by-layer NN method to form a hierarchical representation. It means that DL approaches help to disentangle these abstractions and pick out which features are useful for learning [103, 152–155].

In general, the learning paradigms for DL methods in histology image processing generally include supervised learning and unsupervised learning. In supervised learning, a network is trained using a set of inputs and outputs (targets). For each training case, there will be a set of input values and one or more associated output values, and the goal is to minimize the network's overall output error for all training cases by iteratively adjusting the neuron connection weights and bias values using a specific training algorithm. On the other hand, in unsupervised learning, the training data set does not include any target information. Instead a function is defined that measures the suitability or accuracy of the network. This kind of unsupervised learning network normally uses both input values and output value(s) to produce a cost energy for the current network configuration. Normally the aim of unsupervised learning is to minimize or minimize the cost for all input vectors in the training set [103, 152, 153, 156].

Here I would like to introduce two popular deep learning approaches in recent years: autoencoder (AE) and convolutional neural network (CNN). Autoencoder is an unsupervised learning approach while convolutional neural network is a supervised learning strategy. Both are widely and successfully used in nucleus and cell detection, segmentation and classification of histology images.

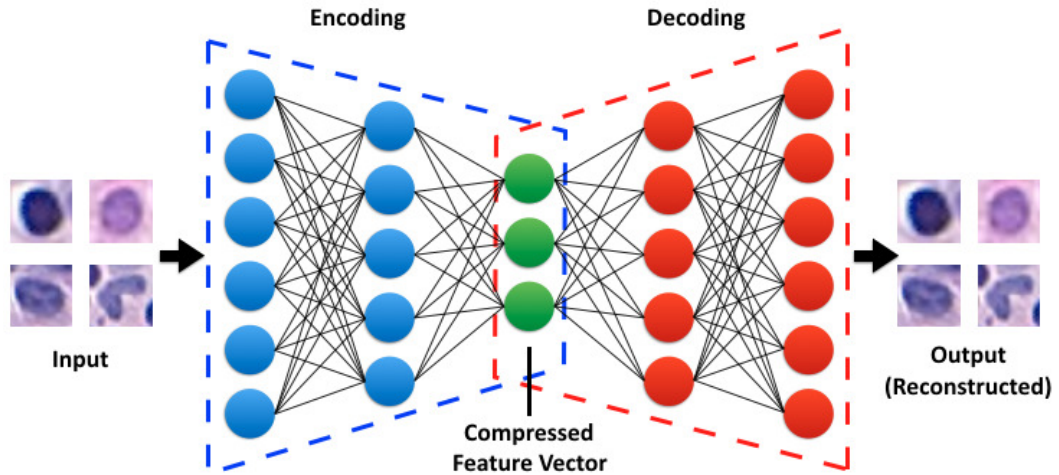


Figure 2.4: The basic structure of autoencoder. Blue and red dash boxes represents the encoding and decoding sections, respectively. Autoencoder learns compressed feature vector of input images by comparing with reconstructed images.

2.2.3.2 Autoencoder

An autoencoder is a specific form of an artificial neural network [157]. Autoencoders were first introduced in the 1980s by Hinton and the PDP research group [103] to address the problem of "backpropagation without a teacher", by using the input data as the teacher to train the layers. The purpose of an autoencoder is to learn another representation of the input data in compressed or sparse representation. More specifically, an autoencoder is an unsupervised learning method that sets the target values to the input values. Together with Hebbian learning rules [103, 152], autoencoders provide one of the fundamental paradigms for unsupervised learning and for beginning to address the mystery of how synaptic changes induced by local biochemical events can be coordinated in a self-organized manner to produce global learning and intelligent behavior.

Functionally, an autoencoder contains two components in the training process, an encoder and a decoder, as shown in Fig. 2.4. The encoder is used to encode the input data x_i to the desired compressed (or sparse) representation by applying transformations, while the decoder decodes this compressed representation to

an approximation of the reconstructed inputs \hat{x}_i , with \hat{x}_i as close to x_i as possible. Usually, the non-linear transformation h is a sigmoid function, i.e., the logistic function

$$h(z) = \frac{1}{1 + \exp(-z)}, \quad (2.3)$$

where $z = Wx + b$ and W is a weight matrix, b is a bias vector. In the training phase of an autoencoder, the parameters W and b are optimized such that the average reconstruction error is minimized. The reconstruction error is used to measure the similarity of \hat{x}_i and x_i , which can be measured in many ways. In general, the traditional squared error is usually used, that is, for any input x_i

$$L(x_i) = (x_i - \hat{x}_i)^2, \quad (2.4)$$

where I assume x_i is a d-dimensional vector.

More recently, autoencoders have taken center stage again in the [103] "deep architecture" approach where autoencoders, particularly in the form of Restricted Boltzmann Machines (RBMS), are stacked and trained bottom up in unsupervised fashion, followed by a supervised learning phase to train the top layer and fine-tune the entire architecture. The bottom up phase is agnostic with respect to the final task and thus can obviously be used in transfer learning approaches. These deep architectures have been shown to lead to state-of-the-art results on a number of challenging classification and regression problems. There are other techniques to prevent autoencoders from learning the identity function and to improve their ability to capture important information and learn richer representations, such as denoising autoencoder (DAE) and sparse autoencoder (SAE). For instance, Su *et al.* [158] use a denoising autoencoder to reconstruct the shape information for cell segmentation. Xu *et al.* [101] use the stacked sparse autoencoder with a softmax classifier to learn a high-level representation of nuclear and non-nuclear objects for detecting and classifying the nuclear region.

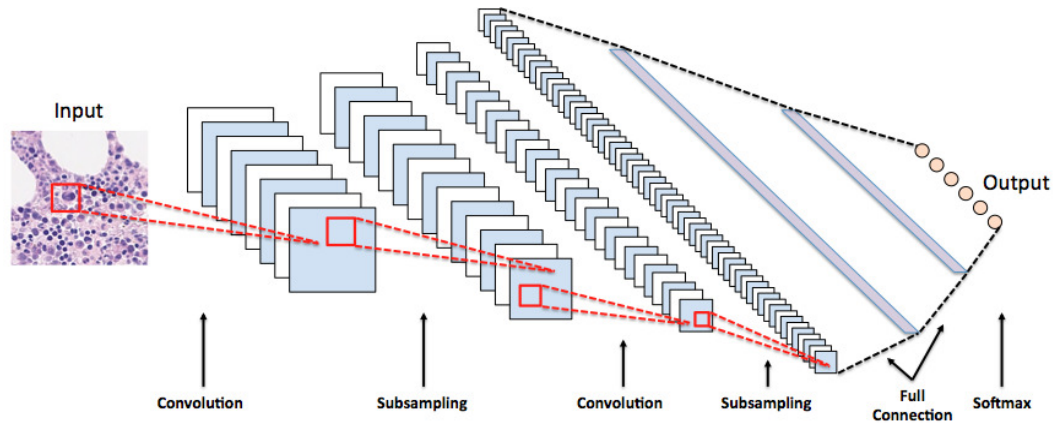


Figure 2.5: The general architecture of CNN. CNN uses convolutional and pooling layers to extract the feature maps from input data and reduce the size of feature maps for accelerating processing speed. Then fully connection layers and softmax layer are used to capture high-level global features and combine them to obtain the proposed task, like classification.

2.2.3.3 Convolutional Neural Network

Recently, CNN has attracted particular attention [152,159,160]. CNN can automatically learn multi-level hierarchies of features which are invariant to irrelevant variations of samples while preserving relevant information [161,162], and has achieved great success on image classification and scene labeling [163,164]. Also, CNN is used on histology image processing. A CNN usually consists of successive pairs of convolutional and pooling layers, followed by several fully connected layers. A convolutional layer learns a set of convolutional filters, which are used to calculate output feature maps, with each convolutional filter corresponding to one output feature map. The pooling layer summarizes the activities and picks the max values over a neighborhood region in each feature map. The pooling layer is also called subsampling layer and is often chosen as max-pooling, which uses a max filter. The fully-connected layer learns more higher level feature representation and the last is often a softmax layer (fully-connected) which outputs the probability that the input patch belongs to a certain category [165]. Fig. 2.5 shows a general CNN struc-

ture. Here the convolution layer is more focused on extracting local features more than global features. This can increase the accuracy dramatically. Also this can reduce the number of excess connections this can also help on algorithms accuracy. Also, the convolution operation can consider the inter relationship between input parameters.

In recent studies, CNN has been successful applied in histology images for detection, segmentation and classification. Cireşan *et al.* [93] have applied a deep CNN to automatic mitotic cell detection in breast cancer histology images. With raw intensities of the testing image, the CNN provides a probability map, in which each pixel value is the probability of the centroid of a mitotic cell. Next, the probability map is smoothed with a disk kernel and final centroid detection is obtained with non-maxima suppression. Similarly, a nine-layer CNN [166] followed by non-maxima suppression is applied to cell detection in wide-field microscopy zebrafish images, which are converted into the YUV color space, and a seven layer CNN [167] is used to locate circular tumor cells in both fluorescence and phase-contrast microscopy images. In [168], Xing *et al.* have learned three different CNN models corresponding to brain tumor, pancreatic neuroendocrine tumor, and breast cancer pathology images, respectively, which are applied to automated nucleus detection. Instead of using a simple non-maxima suppression for detection refinement, Liu and Yang [169] have formulated pancreatic neuroendocrine and lung cancer nucleus detection into an optimization problem. Furthermore, Xie *et al.* [94] have extended the conventional CNN based classification to structure regression for nucleus and cell detection, which generates proximity patches with the fast scanning technique.

Moreover, there are other advanced deep learning architectures such as fully convolution network (FCN), which adopts the concept of AE and only uses convolutional layer and pooling. For instance, BenTaieb *et al.* [170] proposed FCN to process gland segmentation. It can be expected to get more state-of-the-art results to improve the current techniques in the future.

2.3 Materials and Related Methods

In this thesis, I concentrate on H&E stained BM trephine images, which are scanned at $40\times$ magnification objective, which is approximately equal to $0.275\ \mu\text{m}$ per pixel, by using the Omnyx VL120 digital slides scanner from the University Hospital Coventry and Warwickshire (UHCW). Moreover, I use the machine that has 3.1GHz Intel Core i7 with 16 GB memory to implement all the experiments. According to Section 1.4, there are three main approaches to achieve in this thesis. In Chapter 3, I adopt the similar concept from region-based active contour to develop a novel active contour model for delineating megakaryocytes (MKs). In Chapter 4 and 5, I use the autoencoder structure to design a hybrid deep learning approach and a synchronized deep learning approach for BM cell detection and classification. I also compare the performance of the proposed approaches with the performance of conventional and other state-of-the-art methods that I mentioned in this chapter.

2.4 Summary

This chapter briefly described the challenges of histopathology image processing and the current approaches developed for detection, segmentation and classification in histology images. Moreover, I introduced the concepts and advanced applications of image processing and deep learning approaches that I will use to redesign the proposed methods for identifying and obtaining the targets of interest in bone marrow trephine images. For delineating MKs, I consider and improve the region-based active contour, such as Chan-Vese model, because of weak boundary feature of MK cytoplasm. Also, because deep learning approaches provide better performance than other conventional detection methods [95, 101], I adopt the idea of autoencoder model to design novel deep learning methods for detecting and classifying non-MK bone marrow hematopoietic cells in BM trephine images. The details of

the proposed methods will be described in next three chapters.

Chapter 3

Megakaryocyte Delineation using a Traditional Approach

3.1 Introduction

As I mentioned in Section 1.3, these MPNs exhibit a varied but partially overlapping set of clinical and cytomorphological features. This inevitably makes the task of objectively classifying a bone marrow trephine biopsy sample into one of MPNs quite challenging in some cases [1,6,13,18,20,21]. According to WHO classification criteria of MPNs, the present guidelines clearly show that morphological features play a key role in diagnosis and classification. This, however, may cause low reproducibility of diagnostic results and inter-observer variability among the hematopathologists because of ambiguous diagnostic criteria and histological features [13, 20]. In an attempt to resolve these challenges, CAD techniques can be introduced to assist pathologists in classifying the different subtypes of MPNs efficiently and objectively by using digital pathology images [37,171]. Here, trephine histology is used to help in the identification of these bone marrow diseases with CAD techniques.

Within the context of CAD using bone marrow trephine biopsy images, a reliable measurement in the diagnosis of bone marrow diseases is the morphology of

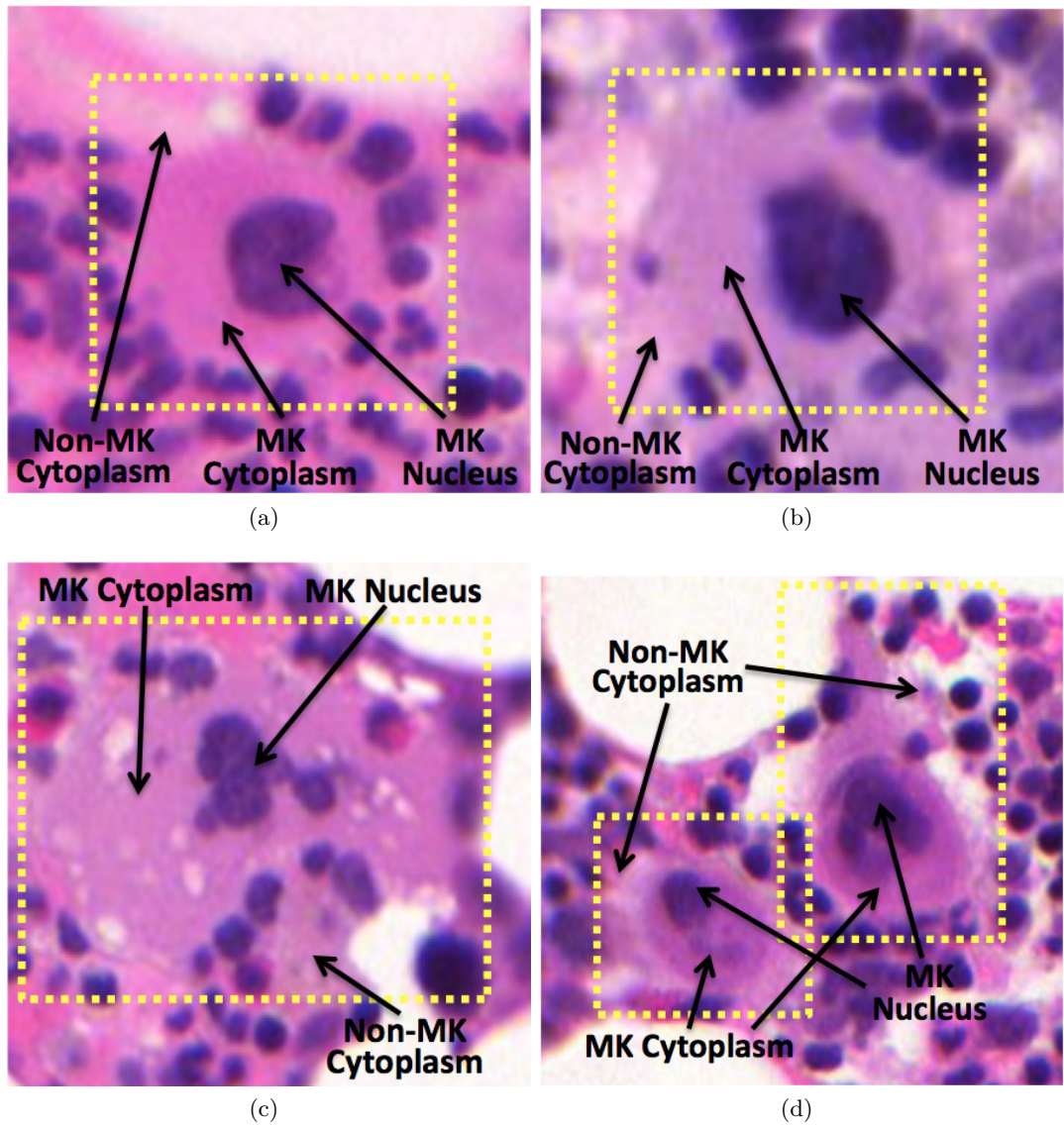


Figure 3.1: Representative examples of bone marrow trephine histology images. The MKs are contained within the yellow dotted rectangles. Note that MK cytoplasm is often partially occluded by nearby cells, other cytoplasmic and non-smooth regions, and their boundaries usually comprise weak edges.

megakaryocytes (MKs), which constitute a population of bone marrow resident cells that are responsible for the production of blood platelets [1, 13, 20, 21]. Compared to other bone marrow cells, MKs usually have distinctive morphological features, like large-sized nuclei and more well-defined cytoplasmic region (see Fig. 3.1). It is thus of particular interest to perform a quantitative analysis of the morphological features of MKs through the detection of the corresponding nucleus and delineation of the cytoplasmic boundary. However, unlike the nucleus, the cytoplasm of MKs is often partially occluded by nearby cells, other cytoplasm and other types of tissue, as shown in Fig. 3.1. Moreover, the corresponding cytoplasmic boundary usually comprises weak edges (see Fig. 3.1 (c)). All these aspects make the task of delineating MKs quite challenging.

There are many approaches applied into BM images [172, 173]. For instance, Huang *et al.* use fuzzy *c*-means clustering method and SVM classifier to detect immature precursors for predicting the early stage of acute myelocytic leukemia [173]. However, in BM trephine biopsy images, a very limited number of approaches have been proposed for the specific cases of MKs. The method proposed by Ballaro *et al.* [96, 174] is a representative approach of obtaining MKs from BM trephine images. They propose an unsupervised image analysis framework to detect and delineate the nuclear and cytoplasmic regions of MKs by using morphological operations, pyramid functions and shape detection [96, 174]. Their framework, however, requires that a single MK be located in the center of the image and be surrounded by a smooth region. In the majority of bone marrow trephine biopsy images we have collected, however, MKs are usually surrounded by non-smooth regions depicting other types of cells and non-MK cytoplasmic regions.

In this chapter, I propose a framework for delineation of MK nuclear and cytoplasmic boundaries based on a novel region-based level set model. The proposed framework first employs color and texture features of different stain color channels of the image in a supervised machine learning setting to delineate MK nuclei. It

then employs a novel region-based active contour model, formulated as a level set function, to delineate the corresponding cytoplasmic boundaries. According to the assumption that the MK nuclei are usually surrounded by cytoplasm, the proposed model incorporates the difference in intensity between internal and external regions of the evolving contour across two deconvolved stain channels into an energy functional to delineate the cytoplasmic boundary. I refer to this novel model as a dual-channel active contour (DCAC) model. Extensive experiments with a large dataset objectively compare the performance of the proposed model with other state-of-the-art methods. I compare the proposed framework using a two-fold approach. First I evaluate the delineation accuracy of my method against other supervised and unsupervised methods. Second, I evaluate the accuracy of the proposed DCAC model in segmenting the corresponding cytoplasmic regions against the Chen-Vese (CV) model, the local binary filter (LBF) model, my basic circumscribing active contour (CAC) model [175], and the multi-region active contour model in [139]. I show that the proposed framework is capable of delineating MKs more accurately than other methods. I particularly show that the DCAC model can identify the MK cytoplasmic boundaries with good segmentation accuracy (around 85%) even in challenging cases where the MK cytoplasm has weak edges and is surrounded by non-smooth regions.

The rest of the chapter is organized as follows. First, I describe the basic framework with CAC model for MK delineation in Section 3.2. Then, in Section 3.3, I introduce the proposed framework for nuclear and cytoplasmic boundary delineation and describe the proposed DCAC model in detail. In Section 3.4, I present and discuss the experimental results and comparison with other methods. Finally, I draw conclusions about the work presented in this chapter in Section 3.5.

3.2 The Basic Framework

In order to automatically delineate MK nuclei and cytoplasm region, I construct a basic framework with an improved CV-based model. Fig. 3.2 illustrates each step involved in the basic framework. The steps within the purple dashed box correspond to pre-processing and MK nuclei delineation. The delineation of cytoplasmic boundaries is performed by the steps within the black dotted box. The initial contour used by the basic CAC model is the boundary of the corresponding MK nucleus. All these steps are described in detail in the remainder of this section.

3.2.1 Stain Normalization and Deconvolution

Bone marrow trephine biopsy slides are commonly dyed using the standard Hematoxylin and Eosin (H&E) stains. Color constancy in these images might be affected by variations on the microscopy light levels, chemical coloring reactivity and staining procedures. These factors may influence the image processing methods used to identify cellular structures. In order to minimize any negative effects on the delineation of MKs, input images are first processed by stain normalization and stain deconvolution. Stain normalization standardizes the stain color while stain deconvolution separates the image into a number of channels that correspond to the stain used. The latter allows analyzing each stain, or channel, separately. I employ a non-linear mapping approach, which estimates stable stain matrices by using an image-specific color descriptor and a robust color classification framework for a particular stain, with channel statistics for stain normalization by using a source image, as proposed in [42]. For stain deconvolution, I employ the stain color descriptor method also proposed in [42] to separate the H&E stained images into two color channel images. The H-channel image provides information about the position of MK nuclei, while the E-channel image emphasizes other tissue constituents including the MK cytoplasm. An example of the output generated by the stain normalization and color

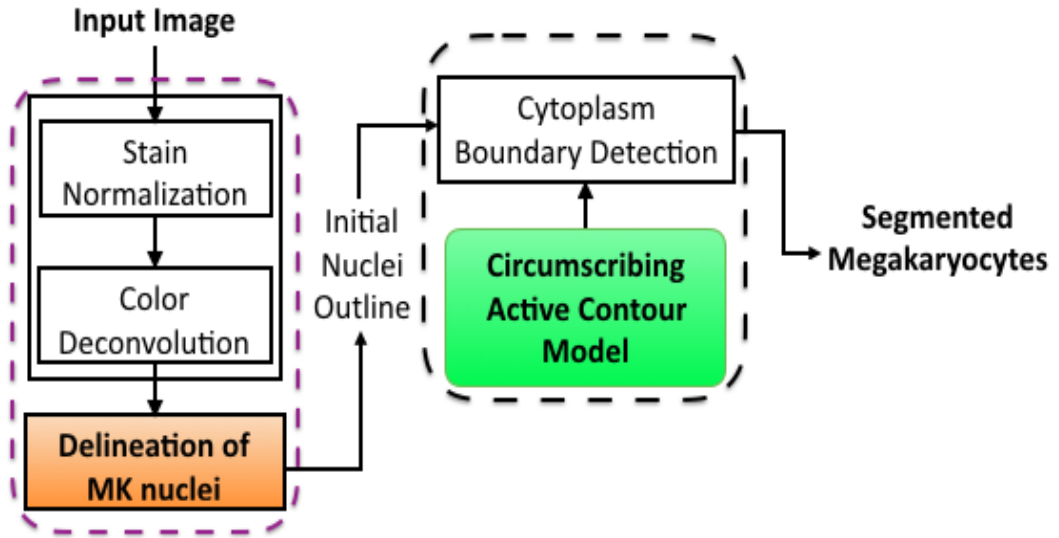


Figure 3.2: The workflow of the framework with the basic CAC model.

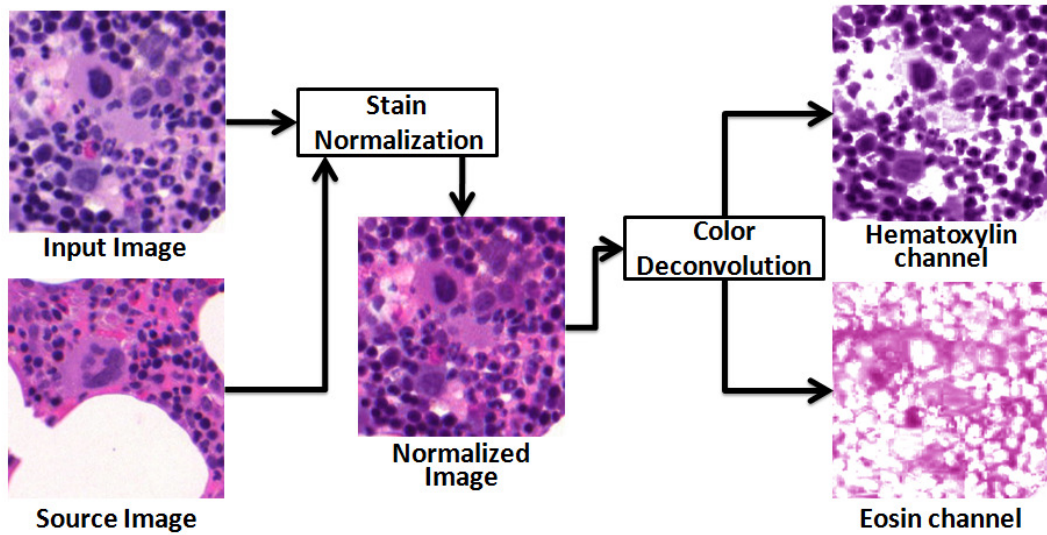


Figure 3.3: Example results of stain normalization and color deconvolution process. Input images are on the left, while output stain channel images are on the right.

deconvolution process is shown in Fig. 3.3. I can observe that indeed, the H- and E-channel images provide clear information about the regions depicting nuclei and cytoplasm, respectively.

3.2.2 Megakaryocytic selection

After stain normalization and color deconvolution, I extract color features from the image data to create the mask of nuclei. Here I consider two color features: gray-scale channel and blue-red ratio of color hematoxylin channel obtained from stain color descriptor method [42], which is the ratio of blue and red color channels and provides a unique way to characterize nuclear pixels. A naïve Bayesian classifier, which is based on applied Bayes theorem with strong independence assumptions, is adopted to generate the nucleus mask by using these color features computed in the H-channel image. The training data for the naïve Bayesian classifier are small patches (10×10 pixels) depicting nuclei in the H-channel images. There are no overlap between adjacent patches as no sliding window is used. These training data is used to estimate the maximum likelihood value for predicting pixels belonging to nuclei [176]. It is important to note that MK nuclei are similar in color and texture to other nuclei, thus the obtained mask depicts all possible nuclei in the image. In order to distinguish MK nuclei from other nuclei in the nuclei mask, I also generate a binary mask depicting MK cytoplasm.

I observe that in the Eosin channel of bone marrow images, the color of MK cytoplasm regions is very similar to other regions; however, the corresponding texture is smoother than that of other regions. In order to compute the cytoplasm mask, I employ an Adaboost classifier, which uses a number of weak classifiers and combines them to form a strong and robust classifier. I use color and texture features of the Eosin channel. Color features are simplified to the intensity level of the gray-scale Eosin channel, which aid in distinguishing and emphasizing the background regions. Texture features are computed using a log-Gabor filter with 6 scales and 10

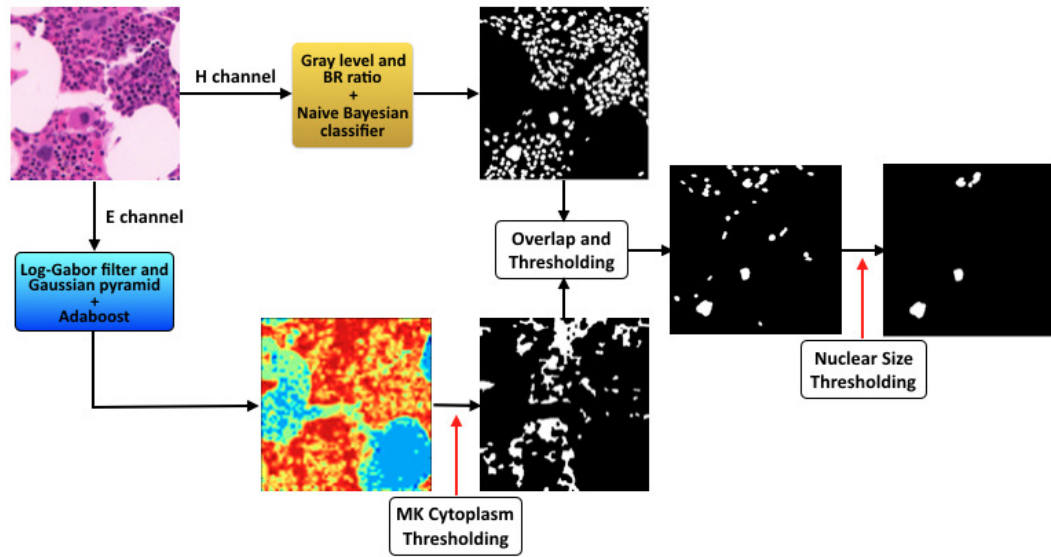


Figure 3.4: Intermediate samples of the process followed to identify MK nuclei in the basic framework. Overlapping the masks of all nuclei and MK cytoplasm and thresholding the size of nuclei are used to select potential MK nuclei.

orientations and a Gaussian pyramid function with an six-level pyramid [177]. Log-Gabor filters are similar to the Gabor filter, which uses a Gaussian kernel function to analyze any specific frequency content in specific direction in the image for texture extraction and analysis, and can be constructed with arbitrary bandwidth for texture measurement. In a Gaussian pyramid, each element of the pyramid represents a local average obtained at a particular scales by Gaussian blurring and downsampling for texture extraction and target localization. The Adaboost classifier is trained with the obtained color and texture features from the image data. Here, in order to avoid encountering an overfitting problem, I use a five-fold cross validation to train the Adaboost classifier. The Adaboost classifier results on a probability map that features high probability values in the smooth regions depicting cytoplasm in the Eosin channel. I use a suitable thresholding value, which is evaluated and optimized by cytoplasm training data, to localize the cytoplasm region in this map and to generate the cytoplasm mask. Fig. 3.4 shows the intermediate process of selecting MK nuclei.

After I obtain the masks of nuclei and cytoplasm, I use these two masks to identify the location of potential MKs. I overlap these two masks and calculate the percentage of the region that each nucleus overlaps with the cytoplasmic area. Here, I eliminate those nuclei that only have an overlap of less than 50 percent. Those with an overlap equal or greater than 50% have a higher probability of being the potential nuclei of MKs. I then keep only those nuclei that are larger than a certain size, which is obtained by measuring the average size of the nuclei of MKs in nuclear training data, since megakaryocytes tend to be larger than other bone marrow cellular structures. Then I delineate the boundaries of the detected nuclei from the binary mask of MK nuclei and further refine them using a simple region-based active contour model. Specifically, I use the CV model, since MK nuclei are usually smooth dark regions surrounded by another relatively smooth region, i.e. the cytoplasm. The CV model includes four energy terms: length, area, internal region intensity and external region intensity. The energy functional is then as follows:

$$\begin{aligned}
F(c_1, c_2, C) &= \mu \text{Length}(C) + \nu \text{Area}(\text{inside}(C)) \\
&+ \lambda_1 \int_{\text{inside}(C)} |I(x, y) - c_1|^2 dx dy \\
&+ \lambda_2 \int_{\text{outside}(C)} |I(x, y) - c_2|^2 dx dy,
\end{aligned} \tag{3.1}$$

where C denotes the evolving contour, c_1 and c_2 are, respectively, the average intensity of the regions inside and outside of C ; $I(x, y)$ denotes the pixel intensity in the image at position (x, y) , and μ , ν , λ_1 and λ_2 are constant parameters. The last two energy terms in (3.1) are the internal and external region intensity terms, respectively. These two terms are usually called as the external energy because they generate an energy force from the image and not the contour itself. These terms control the contour's movement externally. The evolving contour C can be represented by the level-set function $\phi(x, y)$ [14, 118], where $\phi(x, y) > 0$ if the position (x, y) is inside of C and $\phi(x, y) < 0$ if the position (x, y) is outside of C . If position (x, y)

lies on C , $\phi(x, y) = 0$. Let us define the evolving curve C in the image domain Ω . The energy functional $F(c_1, c_2, C)$ can then be formulated in terms of the level-set function $\phi(x, y)$ as follows:

$$\begin{aligned}
F(c_1, c_2, \phi) &= \mu \int_{\Omega} \delta(\phi(x, y)) |\nabla \phi(x, y)| dx dy \\
&+ \nu \int_{\Omega} H(\phi(x, y)) dx dy \\
&+ \lambda_1 \int_{\Omega} |I(x, y) - c_1|^2 H(\phi(x, y)) dx dy \\
&+ \lambda_2 \int_{\Omega} |I(x, y) - c_2|^2 H(1 - \phi(x, y)) dx dy,
\end{aligned} \tag{3.2}$$

where the Heaviside function $H(z)$, Dirac delta function $\delta(z)$, c_1 and c_2 are:

$$H(z) = \begin{cases} 1, & \text{if } z \geq 0 \\ 0, & \text{if } z < 0 \end{cases} \tag{3.3}$$

$$\delta(z) = \frac{d}{dz} H(z) \tag{3.4}$$

$$c_1 = \frac{\int_{\Omega} I(x, y) H(\phi(x, y)) dx dy}{\int_{\Omega} H(\phi(x, y)) dx dy} \tag{3.5}$$

$$c_2 = \frac{\int_{\Omega} I(x, y) H(1 - \phi(x, y)) dx dy}{\int_{\Omega} H(1 - \phi(x, y)) dx dy}. \tag{3.6}$$

3.2.3 Circumscribing Active Contour Model

After segmenting and refining the boundary of nuclei, I detect the boundary of cytoplasm as well. I use the detected nuclear boundary to be the initial contour for the cytoplasm detection process in order to reduce the probability of incorrect segmentation. Note that in the case of cytoplasm detection using CV model, the region outside the contour may be highly heterogeneous, as it may depict other

cellular structures. Since the energy term related to the external region can negatively influence the detection process in cases where this external region is not homogeneous, I restrict the outside region to a n -pixel thick ring area surrounding the current evolving contour C . The optimal value n of ring area is set to 5 because this width value of ring area can get enough neighboring color and texture features and provides better performance of MK delineation. Fig. 3.5 illustrates the original outside region $\tilde{\Omega}(C)$ used in CV model and the modified outside region $\tilde{\Omega}'(C)$ in the CAC model.

In addition, I use the texture features provided by the probability map generated by the Adaboost classifier to assist the region-based active contour model in detecting the boundary of cytoplasm. Specifically, apart from the regularizing terms related to the length and area of contour C , and the external forces related to the difference in intensities inside and outside contour C , I add two energy terms related to the difference in cytoplasmic probabilities inside and outside C as two extra external forces. Since the outside region in the proposed model is a ring surrounding the desired object and the initial contour is the one obtained previously for the corresponding nucleus, I call this model circumscribing active contour (CAC) model. The energy functional is then defined as follows:

$$\begin{aligned}
F(c_1, \bar{c}_2, p_1, \bar{p}_2, C) = & \mu Length(C) + \nu Area(C) + \int_{\Omega(C)} |u_0(x, y) - c_1|^2 \\
& + \int_{\tilde{\Omega}'(C)} |u_0(x, y) - \bar{c}_2|^2 + \int_{\Omega_p(C)} |p_0(x, y) - p_1|^2 \quad (3.7) \\
& + \int_{\tilde{\Omega}_p'(C)} |p_0(x, y) - \bar{p}_2|^2,
\end{aligned}$$

where $\tilde{\Omega}'(C)$ is new outside region that replaces the original outside region $\tilde{\Omega}(C)$; \bar{c}_2 is the mean intensity value of the new restricted outside region $\tilde{\Omega}'$; Ω_p is the probability map of MK cytoplasmic texture; $\Omega_p(C)$ and $\tilde{\Omega}_p'(C)$ are the inside and outside regions of contour C on the probability map, respectively; p_1 and \bar{p}_2 are the

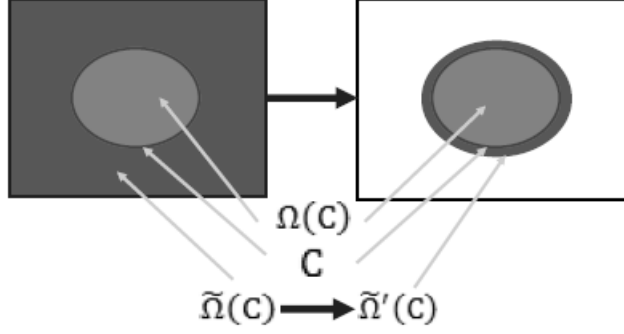


Figure 3.5: The region outside of the current evolving contour C in CV model and in the CAC model

mean cytoplasmic probability values of the inside and outside regions of contour C , respectively; and $p_0(x, y)$ represents the cytoplasmic probability value at location (x, y) .

The detail energy functional of the proposed CAC model is derived from CV model. I modify the outside region of the contour C to be restricted to a ring around C . I also add texture features in the form of two extra energy terms based on the probability map of cytoplasm:

$$\begin{aligned}
F(c_1, \bar{c}_2, p_1, \bar{p}_2, \phi, \phi') &= \mu \int_{\Omega} \delta(\phi(x, y)) |\nabla \phi(x, y)| dx dy + \nu \int_{\Omega} H(\phi(x, y)) dx dy \\
&+ \lambda_1 \int_{\Omega} |u_0(x, y) - c_1|^2 H(\phi(x, y)) dx dy \\
&+ \lambda_2 \int_{\Omega} |u_0(x, y) - \bar{c}_2|^2 (1 - H(\phi(x, y))) H(\phi'(x, y)) dx dy \\
&+ \lambda_3 \int_{\Omega_p} |p_0(x, y) - p_1|^2 H(\phi(x, y)) dx dy \\
&+ \lambda_4 \int_{\Omega_p} |p_0(x, y) - \bar{p}_2|^2 (1 - H(\phi(x, y))) H(\phi'(x, y)) dx dy,
\end{aligned} \tag{3.8}$$

$$\begin{aligned}
\frac{\partial \phi}{\partial t} &= \delta_{\varepsilon}(\phi) \left[\mu \operatorname{div} \left(\frac{\nabla \phi}{|\nabla \phi|} \right) - \nu - \lambda_1 (u_0 - c_1)^2 + \lambda_2 (u_0 - \bar{c}_2)^2 - \lambda_3 (p_0 - p_1)^2 \right. \\
&\quad \left. + \lambda_4 (p_0 - \bar{p}_2)^2 \right],
\end{aligned} \tag{3.9}$$

where Ω_p is the probability map, and $\lambda_1, \lambda_2, \lambda_3$ and λ_4 are the parameters controlling the energy force of inside and outside regions in intensity and probability maps. \bar{c}_2 and \bar{p}_2 are the mean values of two new restricted outside regions in the intensity and probability map images, respectively. These constants and ϕ' , which denotes the boundary of the new restricted outside region, are calculated as follows:

$$\bar{c}_2 = \frac{\int_{\Omega} u_0(x, y) (1 - H(\phi(x, y))) H(\phi'(x, y)) dx dy}{\int_{\Omega} (1 - H(\phi(x, y))) H(\phi'(x, y)) dx dy}, \quad (3.10)$$

$$\bar{p}_2 = \frac{\int_{\Omega_t} u_0(x, y) (1 - H(\phi(x, y))) H(\phi'(x, y)) dx dy}{\int_{\Omega_t} (1 - H(\phi(x, y))) H(\phi'(x, y)) dx dy}, \quad (3.11)$$

$$\phi'(x, y) = \phi(x + \gamma \vec{\eta}_x, y + \gamma \vec{\eta}_y), \quad (3.12)$$

$$\vec{\eta}(x, y) = \frac{\nabla \phi(x, y)}{|\nabla \phi(x, y)|}, \quad (3.13)$$

where $\vec{\eta}(x, y)$ denotes the normal vector to the contour C and γ is a parameter for setting the width of the new restricted outside region ϕ' . It is important to emphasize that, by using a smaller outside region to define the external forces, I avoid creating forces based on a highly heterogeneous external region depicting different cellular structures, which may hinder the evolution of the contour to the cytoplasm boundary.

However, this basic framework with CAC model still has the drawbacks in MK delineation. For instance, the Adaboost classifier needs much time to be trained and cannot efficiently identify the MK cytoplasm region because log-Gabor filter may blur the difference between the nuclear region and cytoplasm region in Eosin channel. In addition, CAC model are affected by this texture feature energy force, which uses the cytoplasm probability map from the Adaboost classifier, and does not efficiently and easily minimize the convergence energy. The results of MK cy-

toplasmic boundaries have serious jitter shape because of the influence of texture feature energy. In order to resolve these problems, I redesign an advanced framework to efficiently and precisely delineate MKs. In order to resolve the problems of the basic framework with CAC model, I propose another novel framework with a novel AC model to delineate MKs.

3.3 The Proposed Framework

Fig. 3.6 graphically illustrates the steps involved in the proposed framework to delineate MK nuclei and cytoplasm. The different sections between the basic and proposed framework are MK nuclei delineation and the delineation of cytoplasmic boundaries. The proposed AC model is performed by the steps within the red dotted box. As same as the basic framework, the initial contour used by the proposed DCAC model is the boundary of the corresponding MK nucleus. The details of these two different parts in the proposed framework are described in this section.

3.3.1 Delineation of MK Nuclei

In proposed framework, I use the same approach [42] to do stain normalization and color deconvolution for obtaining H- and E-stain channels. As same as the basic framework, I first manually crop several small patches (10×10 pixels) from different training H-channel images. These training patches depict MK nuclear regions, MK cytoplasmic regions, other cytoplasmic regions and the background region, e.g., fat tissue. I then use the naïve Bayesian classifier with color features extracted from these H-channel training patches to generate a binary mask of all nuclei. Also, in order to identify MK nuclei from other nuclei in the nuclei mask, I need to generate a binary mask depicting MK cytoplasm. It is important to note that I apply the scattering transform [178], which construct invariant, stable and informative signal representations by scattering the signal information with a cascade of wavelet

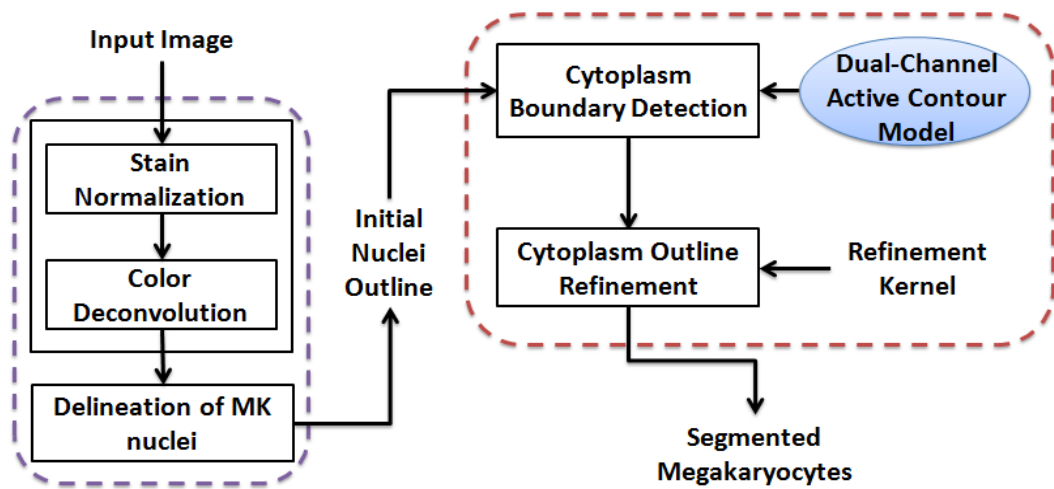


Figure 3.6: The workflow of the framework with the proposed DCAC model.

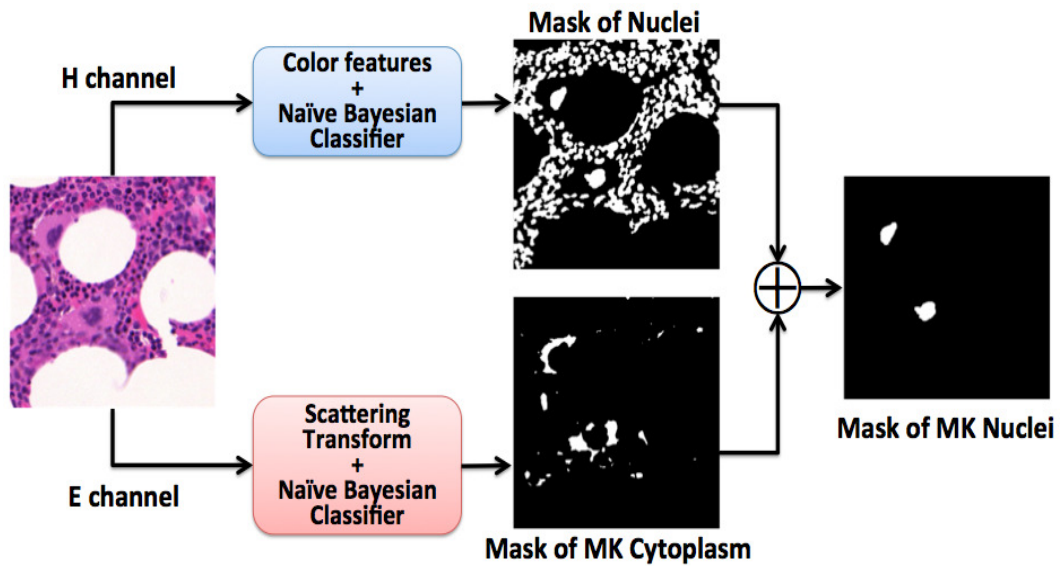


Figure 3.7: Example intermediate results of the process followed to identify MK nuclei in the proposed framework. The masks of all nuclei and MK cytoplasm are used to identify MK nuclei.

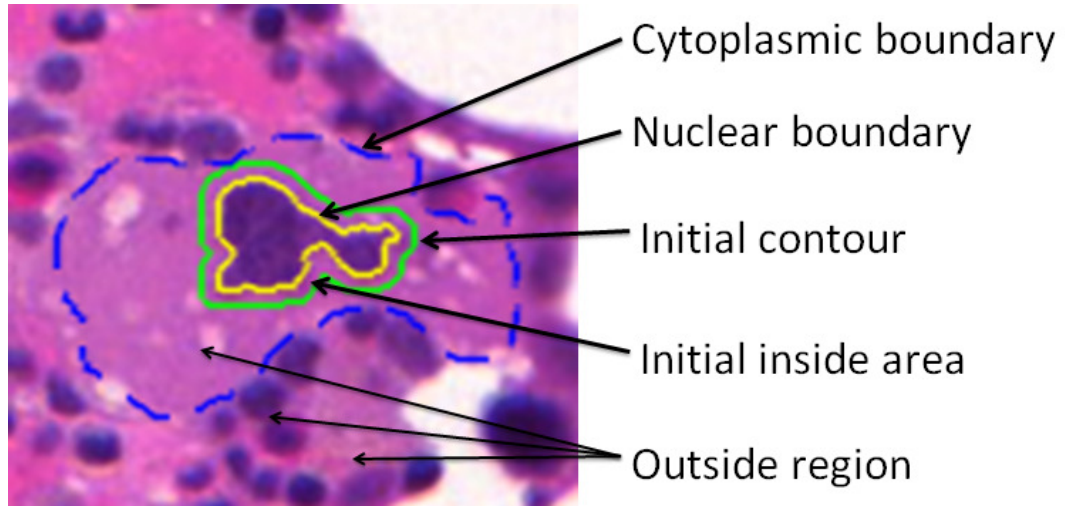


Figure 3.8: An example initial contour and the corresponding inside region and the nuclear boundary, C_n . The initial contour (in green) is obtained by dilating C_n (in yellow).

modulus operators, on E-channel training images to extract texture features of MK cytoplasm instead of log-Gabor filter and Gaussian pyramid. Scattering transform extracts texture features of MK cytoplasmic region more efficiently than log-Gabor filter and Gaussian pyramid do. After that, these features are used in another naïve Bayesian classifier, which takes the place of Adaboost classifier, along with E-channel color features to generate the cytoplasm mask. It is because Adaboost classifier takes much time on training and has worse performance than naïve Bayesian classifier. Since the MKs have larger cytoplasmic regions than other cells, I overlap these two masks and measure the area surrounding each nucleus that overlaps a cytoplasmic region in order to identify MK nuclei. In other words, I am interested in identifying those nuclei surrounded by a large cytoplasm. Fig. 3.7 shows example intermediate results of the process followed to identify MK nuclei. Then I also use the CV model to refine the boundaries of the detected nuclei. To this end, the refined nuclear boundary generated by employing the model in (3.2) serves as the initial contour for the proposed DCAC model, which I use to delineate the corresponding MK cytoplasm boundary.

3.3.2 The Proposed Dual-Channel Active Contour Model

3.3.2.1 The External Energy Force

As I mentioned before, MK cytoplasm are usually relatively smooth regions partially occluded by other tissues and surrounded by non-smooth regions, as shown in Figure 3.8. Based on this observation, my proposed DCAC model considers intensity information of both the H- and E-channel images to delineate the boundary of MK cytoplasm. Similar to the CV model, the proposed DCAC model also employs four energy terms: length, area, internal region intensity and external region intensity. It employs the corresponding previously delineated nuclear boundary as the initial contour. The DCAC model, however, uses as the inside region of the evolving contour C , the region inside of C excluding the nucleus. Therefore, the initial contour is dilated by a small amount in order to define the initial region inside of C . I denote the previously delineated nuclear boundary in terms of a level-set function as $C_n = \{(x, y) \mid \phi_n(x, y) = 0\}$. The proposed inside region intensity term, F_{in} , in the DCAC model is then given by:

$$\begin{aligned} F_{in}(c'_1, \phi) &= \int_{inside(C) - inside(C_n)} |I(x, y) - c'_1|^2 dx dy \\ &= \int_{\Omega} |I(x, y) - c'_1|^2 \left(\widehat{H}(\phi(x, y), \phi_n(x, y)) \right) dx dy, \end{aligned} \quad (3.14)$$

where the function $\widehat{H}(a, b)$ is defined as the difference of two Heaviside functions:

$$\widehat{H}(a, b) = H(a) - H(b), \quad (3.15)$$

and the inside mean value c'_1 is defined as:

$$c'_1 = \frac{\int_{\Omega} I(x, y) \widehat{H}(\phi(x, y), \phi_n(x, y)) dx dy}{\int_{\Omega} \widehat{H}(\phi(x, y), \phi_n(x, y)) dx dy}. \quad (3.16)$$

The energy function in (3.14) assumes a relatively smooth region, which is true as long as the inside region of C represents exclusively the cytoplasm. Under this assumption, the energy term in (3.14) is then minimized when the inside region of C exclusively comprises the MK cytoplasm. An example initial contour and the corresponding inside region and C_n are depicted in Fig. 3.8.

It is worth recalling that the outside region intensity term of the CV model in (3.2) is expected to be minimized when the pixels intensities in the outside region are similar to the value c_2 (see (3.1)). In the DCAC model, I assume that the outside region is non-smooth and, therefore, several pixels in this outside region are likely to be dissimilar to the value of c_2 . However, I expect that when the contour is located in the cytoplasmic boundary, the pixels in the outside region are sufficiently different from the mean of the inside region, i.e. c'_1 in (3.16). In other words, I expect that the integral $\int_{outside(C)} (I(x, y) - c'_1)^2$ results in a large value when the contour is located at the cytoplasmic boundary. Based on this observation, I use this large difference between pixels in the inside region of C (i.e., those depicting the MK cytoplasm) and those in the outside region of C to be the outside region intensity term. To this end, I introduce a maximum intensity difference value, MD , in the outside region intensity term to help the contour to expand and accurately detect the cytoplasmic boundary:

$$MD = \max\{|I(x, y) - c'_1|\}. \quad (3.17)$$

The proposed outside region intensity term in the proposed DCAC model is then given as follows:

$$F_{out}(c'_1, \phi, MD) = \int_{\Omega} |MD - |I(x, y) - c'_1||^2 \times \left(1 - H(\phi(x, y))\right) dx dy. \quad (3.18)$$

According to (3.18), F_{out} is expected to be minimized when the difference

between pixels in the region outside of C and c'_1 is sufficiently large and close to MD . Therefore, MD represents the maximum difference between a pixel in the region outside of C and c'_1 , under the assumption that the outside region of the evolving contour is non-smooth, which is the case when detecting MK cytoplasm in bone marrow trephine biopsies. The proposed external energy force in the DCAC model is then defined as follows:

$$\begin{aligned}
F_{ex}(c'_1, \phi, MD) = & \lambda_1 \int_{\Omega} |I(x, y) - c'_1|^2 \times \\
& \left(\widehat{H}(\phi(x, y), \phi_n(x, y)) \right) dx dy \\
& + \lambda_2 \int_{\Omega} |MD - |I(x, y) - c'_1||^2 \times \\
& \left(1 - H(\phi(x, y)) \right) dx dy.
\end{aligned} \tag{3.19}$$

3.3.2.2 The External Energy Force on Stain Channel Images

In order to improve the delineation accuracy of the cytoplasmic boundary using the external energy force in (3.19), I employ intensity information from the two stain channel images. As discussed earlier, the H-channel image usually shows the position of nuclei very clearly while the E-channel image is usually useful to discriminate between cytoplasm and other tissues. I take advantage of this and define the external force in (3.19) for each of these two channel images:

$$\begin{aligned}
F_{ex_H}(c'_H, \phi, MD) = & \lambda_1 \int_{\Omega} |I_H(x, y) - c'_H|^2 \times \\
& \left(\widehat{H}(\phi(x, y), \phi_n(x, y)) \right) dx dy \\
& + \lambda_2 \int_{\Omega} |MD_H - |I_H(x, y) - c'_H||^2 \times \\
& \left(1 - H(\phi(x, y)) \right) dx dy,
\end{aligned} \tag{3.20}$$

$$\begin{aligned}
F_{ex-E}(c'_E, \phi, MD) = & \lambda_1 \int_{\Omega} |I_E(x, y) - c'_E|^2 \times \\
& \left(\widehat{H}(\phi(x, y), \phi_n(x, y)) \right) dx dy \\
& + \lambda_2 \int_{\Omega} |MD_E - |I_E(x, y) - c'_E||^2 \times \\
& \left(1 - H(\phi(x, y)) \right) dx dy,
\end{aligned} \tag{3.21}$$

where c'_H and c'_E are the average intensity values of the inside regions of C in the H-channel image, denoted by $I_H(x, y)$, and E-channel image, denoted by $I_E(x, y)$, respectively. MD_H and MD_E denote the MD values for the H- and E-channel images, respectively. Fig. 3.9 illustrates how the H- and E-channel images can help the evolving contour to detect the extent of the MK cytoplasmic region. In order to accurately differentiate MK cytoplasmic regions from other non-MK cytoplasmic regions, I use either the external energy force in (3.20) or in (3.21) based on the channel that provides the most discriminative information. To this end, I define a binary weight W as follows:

$$W(c'_H, c'_E) = \begin{cases} 1, & \text{if } |I_H(x, y) - c'_H| \geq |I_E(x, y) - c'_E| \\ 0, & \text{otherwise} \end{cases}. \tag{3.22}$$

The binary weight W considers the difference between pixels and the mean intensity of the region inside of C in each stain channel image. I use this binary weight to select the stain channel image that provides the largest difference. This is based on the observation that the H- and E-channel images provide distinct boundary information. The H-channel image emphasizes the nuclear boundaries more strongly than the E-channel image. On the other hand, the E-channel image emphasizes the cytoplasmic boundaries more strongly than H-channel image. This allows us to accurately control the contour's expansion towards the MK cytoplasmic boundary and accurately minimize the external energy term. It is important to note that if W is defined as a weight that can take any value in the range $[0, 1]$, the

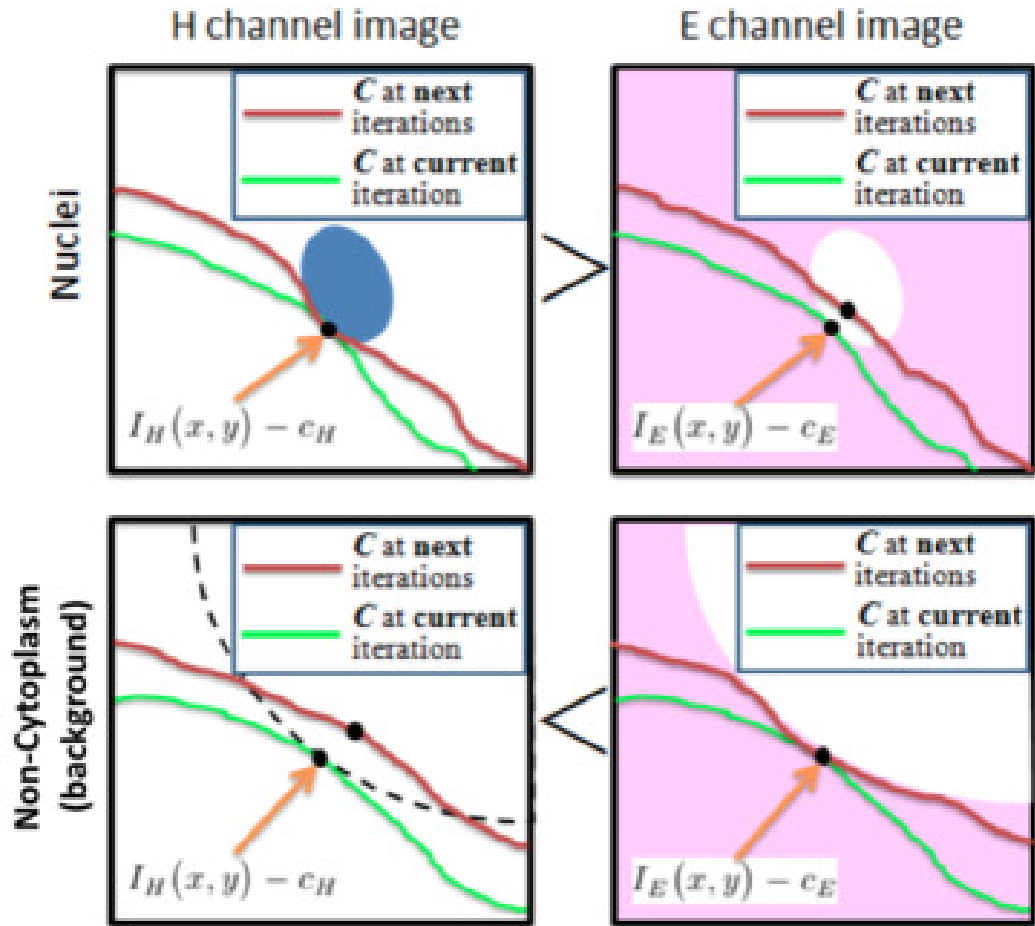


Figure 3.9: The upper row shows how the difference between pixel values and c_H is larger on the H-channel image than on the E-channel image. This helps to stop the evolving contour when encountering other nuclei outside the cytoplasmic regions. The bottom row shows how the E-channel image can be used to efficiently distinguish between the MK cytoplasmic region and other non-MK cytoplasm region different from nuclei. In other words, if the energy force of H-channel image is larger than that of E-channel image, the evolving contour will be stopped on the boundary of the nucleus by the energy force of H-channel image (upper row). If the energy force of E-channel image is larger than that of H-channel image, the energy force of E-channel image will control the evolving contour stopping on the boundary of non-MK cytoplasm region, like background (bottom row). When the difference between the energy force of H-channel image and the energy force of E-channel image is quite small, the evolving contour will stop moving.

result would again mix the information provided by the H- and E-channel images, thus defeating the purpose of channel deconvolution. Combining the external energy forces as defined for the two stain channel images with binary weight $W(c'_H, c'_E)$, the external energy force is then given as follows:

$$F_{ex_total} = W(c'_H, c'_E)F_{ex_H} + (1 - W(c'_H, c'_E))F_{ex_E}. \quad (3.23)$$

In order to prevent over-segmentation of non-MK cytoplasmic regions in the outside region of C , I restrain the contour's expansion to those pixels located in a ring-like region surrounding C . The boundary of this ring-like region is given by:

$$\phi_\gamma(x, y) = \phi(x + \gamma\vec{\eta}_x, y + \gamma\vec{\eta}_y), \quad (3.24)$$

$$\vec{\eta}(x, y) = \frac{\nabla\phi(x, y)}{|\nabla\phi(x, y)|}, \quad (3.25)$$

where the parameter γ controls the width of the ring-like region and $\vec{\eta}(x, y)$ denotes the normal vector of the expanding contour. An example of this ring-like region is shown in Fig. 3.10. The complete set of forces in the DCAC model is then as follows:

$$\begin{aligned} F_{total} &= \mu \int_{\Omega} \delta(\phi(x, y)) |\nabla\phi(x, y)| dx dy \\ &+ \nu \int_{\Omega} H(\phi(x, y)) dx dy \\ &+ F_{ex_total} \hat{H}(\phi_\gamma(x, y), \phi(x, y)). \end{aligned} \quad (3.26)$$

It is important to note that the ring-like expansion, ϕ_γ , in conjunction with F_{ex_total} play key roles to help the contour to efficiently and accurately conform to the cytoplasmic boundary. It is also important to note that if the contour encapsulates smooth cytoplasm from neighboring cells, and not only the smooth cytoplasm from the MK to be delineated, F_{out} in (3.18) may still be a valid force making the contour evolve. In this case, the internal energy terms in (3.26) help to prevent these types of leakages.

The energy functional in (3.26) can be minimized with respect to ϕ by deducing the associated Euler-Lagrange equation for ϕ as follows:

$$\begin{aligned} \frac{\partial \phi}{\partial t} = \delta(\phi) \left\{ \mu \operatorname{div} \left(\frac{\nabla \phi}{|\nabla \phi|} \right) - \nu - (\delta(\phi_\gamma) - \delta(\phi)) \times \right. \\ \left. \left[W(c'_H, c'_E) \left(\lambda_1 (I_H - c'_H)^2 \right. \right. \right. \\ \left. \left. \left. - \lambda_2 (MD_H - |I_H - c'_H|)^2 \right) \right. \right. \\ \left. \left. + (1 - W(c'_H, c'_E)) \left(\lambda_1 (I_E - c'_E)^2 \right. \right. \right. \\ \left. \left. \left. - \lambda_2 (MD_E - |I_E - c'_E|)^2 \right) \right] \right\} \end{aligned} \quad (3.27)$$

where $\operatorname{div}(\cdot)$ is the divergence operator. The contour's expansion is terminated if the following criterion is met:

$$\begin{aligned} \frac{1}{\int \mathbf{1}(F_{total}^j(x, y) > T) dx dy} \times \\ \left(\left| \int_{\phi^j > 0} F_{total}^j \mathbf{1}(F_{total}^j(x, y) > T) dx dy \right. \right. \\ \left. \left. - \int_{\phi^{j-1} > 0} F_{total}^{j-1} \mathbf{1}(F_{total}^j(x, y) > T) dx dy \right| \right) < \tau \left(\alpha \sqrt{\frac{\gamma}{5}} \right)^2, \end{aligned} \quad (3.28)$$

where τ is the time step, ϕ^j denotes the j th iteration of the evolving curve, F_{total}^j is the total energy in the j th iteration, $F_{total}(x, y)$ is the total energy at the pixel (x, y) , $\mathbf{1}(x)$ is the indicator function and T is a threshold value to discard those pixels that feature very low energy values. In this work, I set the stop parameter α to 0.06 and the threshold value T to 0.5 based on several experiments. These values guarantee that the total energy difference between two consecutive iterations is minimal. Finally, after the cytoplasmic boundary is delineated using the DCAC model, I use the cubic spline interpolation with Gaussian smoothing as the refinement kernel [179] to smooth its shape.

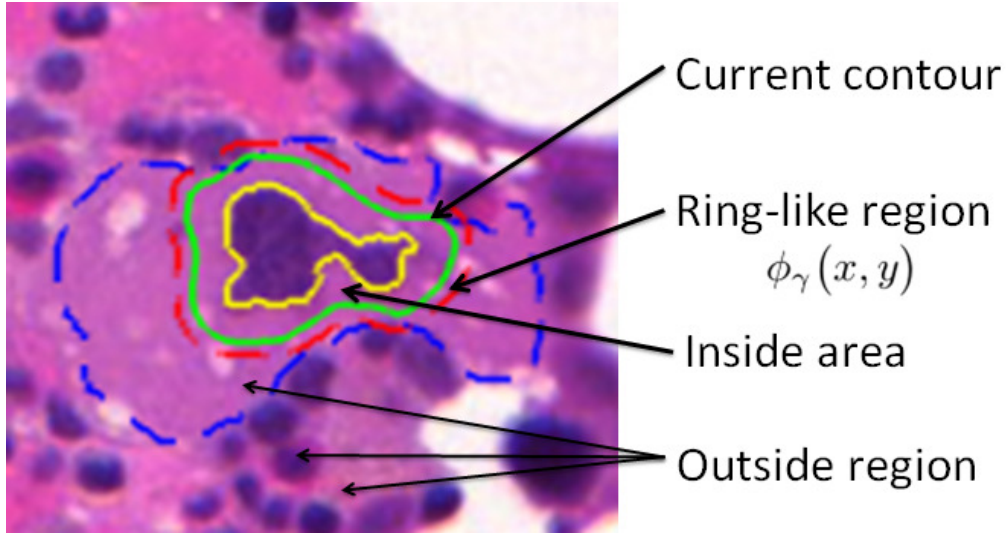


Figure 3.10: An example evolving contour and the corresponding ring-like region. The green contour denotes the evolving contour C ; the blue dashed contour denotes the cytoplasmic boundary; the yellow contour denotes the nuclear boundary, C_n ; and the red dashed contour denotes the ring-like region boundary.

3.4 Experimental Results

Three sets of experiments were performed. The first one evaluates the accuracy of MK nuclei detection as described in Section 3.3.1. The second experience evaluates the performance of the DCAC model to delineate MK cytoplasmic boundaries as compared to other region-based level-set methods. And the third one evaluates my complete framework against the multi-region active contour in [139], which allows delineating the nuclear and cytoplasmic boundaries simultaneously. All results are obtained using 50 images of bone marrow trephine biopsies digitized at $40\times$ magnification objective using the Omnyx VL120 digital slides scanner installed at the University Hospital Coventry and Warwickshire (UHCW), UK.

3.4.1 Evaluation of MK nuclei detection

I compare my MK nuclei detection method with an automatic unsupervised MK detection framework [96, 174], which I implemented in Matlab, and my supervised

Table 3.1: MK nuclei detection accuracy of three evaluated methods

| Framework | Precision | Recall | F1-score |
|-------------------------------------|-------------|--------------|---------------|
| Ballaro’s method [96, 174] | 0.84 | 0.5 | 0.6269 |
| Supervised framework of CAC [175] | 0.7 | 0.875 | 0.7758 |
| Proposed MK nuclei detection method | 0.86 | 0.833 | 0.8518 |

MK nuclei detection method previously proposed in [175], which uses an Adaboost classifier to generate the cytoplasm mask. I use 50 bone marrow trephine images, including 73 megakaryocytes, of early-stage ET and PMF diseases in this evaluation; 50% of the images are used for training and 50% for testing. Table 3.1 tabulates results in terms of precision, recall and accuracy for the three methods. Precision is the percentage of selected MK nuclei that are correct and Recall gives the percentage of selected correct MK nuclei in all ground truth of MK nuclei. The F1-score is the harmonic mean of Precision and Recall and is computed as $2 \times Precision \times Recall / (Precision + Recall)$. Results in Table 3.1 are computed using manually annotated ground truth provided by a pathology trainee and a senior pathologist (Dr. H. EIDaly) from the Addenbrookes Hospital, UK.

The proposed MK delineation method provides an accuracy of 85%, attaining the best performance. It is important to emphasize that the automatic unsupervised framework (Ballaro’s method) in [96, 174] is limited to identify the MKs that are closest to the center of the input image. Therefore, that method can only identify one MK nucleus per image. If the MK is located far from the image center with several other large overlapping structures, that framework is likely to obtain an incorrect result. My MK nuclei detection method, on the other hand, is capable of identifying several MK nuclei regardless of their position in the image. Although my previous supervised framework can provide good accuracy in identifying MK nuclei, the Adaboost classifier requires long times to process the texture of cytoplasm. The proposed method in this work can identify MK nuclei more efficiently with shorter computational times.

Table 3.2: Parameters of the evaluated models

| AC models | Parameters | | | | | | | | |
|--------------------------|------------|-------|-------------|-------------|-------------|-------------|----------|-------|----------|
| | μ | ν | λ_1 | λ_2 | λ_3 | λ_4 | σ | d | γ |
| CV [14] | 0.2 | 0 | 1 | 1 | — | — | — | — | — |
| LBF [128] | 0.2 | 0 | 1 | 1 | — | — | 3 | — | — |
| CAC [175] | 0.2 | 0 | 1.5 | 1 | 1.5 | 1 | — | — | — |
| Multi-region model [139] | — | — | 2/0.25 | 1.05/0.6 | — | — | — | 10/10 | — |
| Proposed DCAC model | 0.2 | 0 | 1 | 1 | — | — | — | — | 5 |

3.4.2 Evaluation of the Proposed DCAC Model

return;

As explained in Section 3.2, I expand the delineated nuclear boundary and use this as the initial contour for the proposed DCAC model. The delineated nuclear boundary is dilated by 3 pixels. This guarantees that the inside region of initial contour includes cytoplasm. For this evaluation, I use 40 MK cases in 30 images. Manually annotated ground truth data depicting MK nuclear and cytoplasmic boundaries are provided by a junior trainee and a senior pathologist. Fig. 3.11 shows four sample visual results obtained by the DCAC model. Note that the identified cytoplasmic boundaries cover most of the ground truth cytoplasmic region.

I compare the proposed DCAC model with Ballaro’s method [96, 174], and the CV, the LBF, and the CAC models. These last three models are all region-based level-set methods. For all evaluated models, I use the same initial contour and post-processing to delineate and refine the shape of the MK cytoplasmic boundaries. In order to provide a fair comparison, the parameters of the region-based level-set methods are set to those values that provide the best performance on the MK dataset (see Table 3.2). For the CAC model, λ_3 and λ_4 denote the parameters of internal and external texture energy forces, respectively. The local region in the LBF model is generated using the Gaussian kernel with $\sigma = 3$. In the DCAC model, I set the width of the ring-like region to $\gamma = 5$ pixels. The ring-like region should be

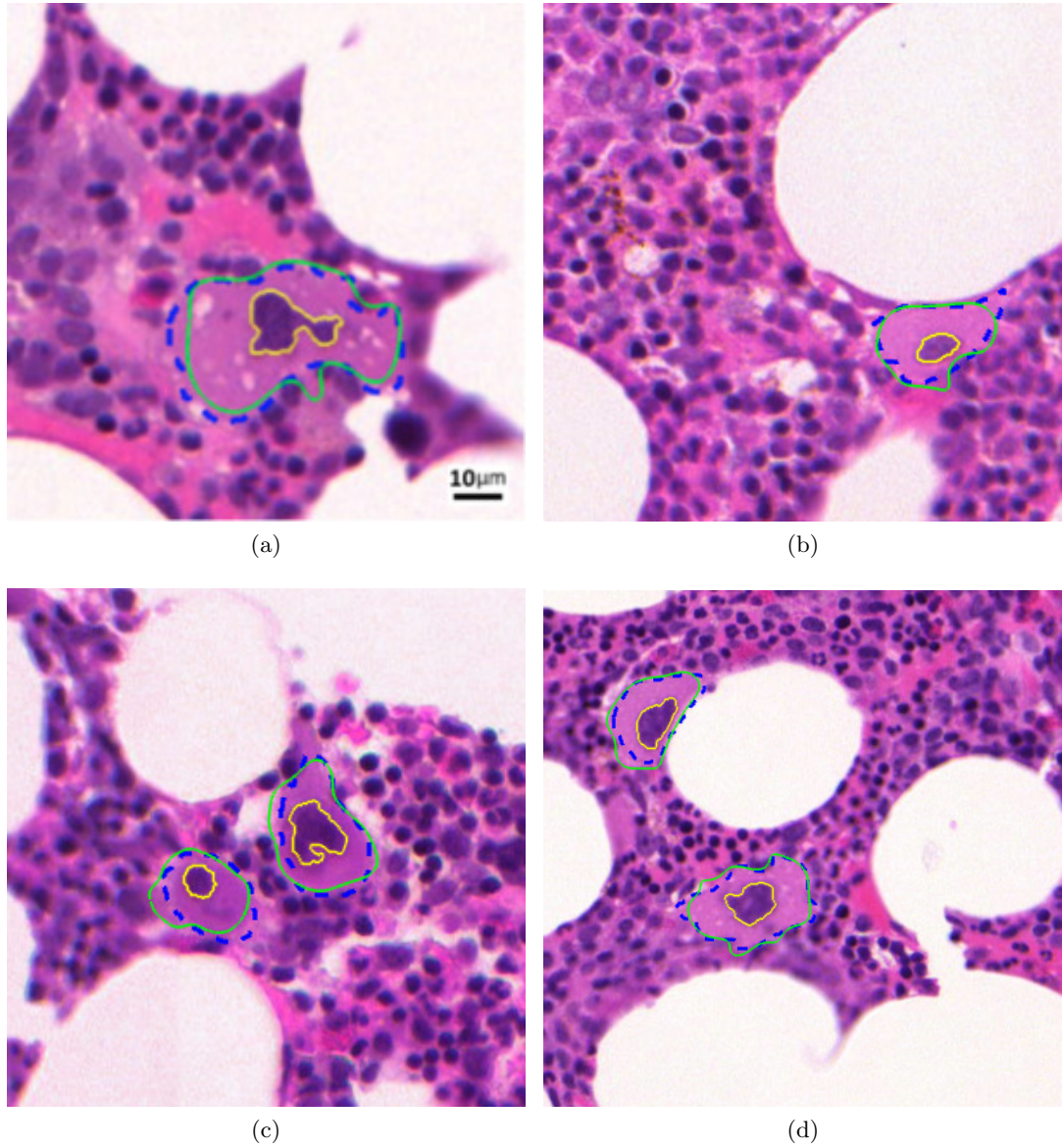


Figure 3.11: Visual results of the proposed DCAC model for identification of MK cytoplasmic boundaries. Yellow contours denote the segmented nuclear boundaries by the CV model. This boundary is used as the initial contour in the proposed model after dilating them. Green contours denote the identified cytoplasmic boundaries. Blue dashed contours denote the ground truth as manually annotated.

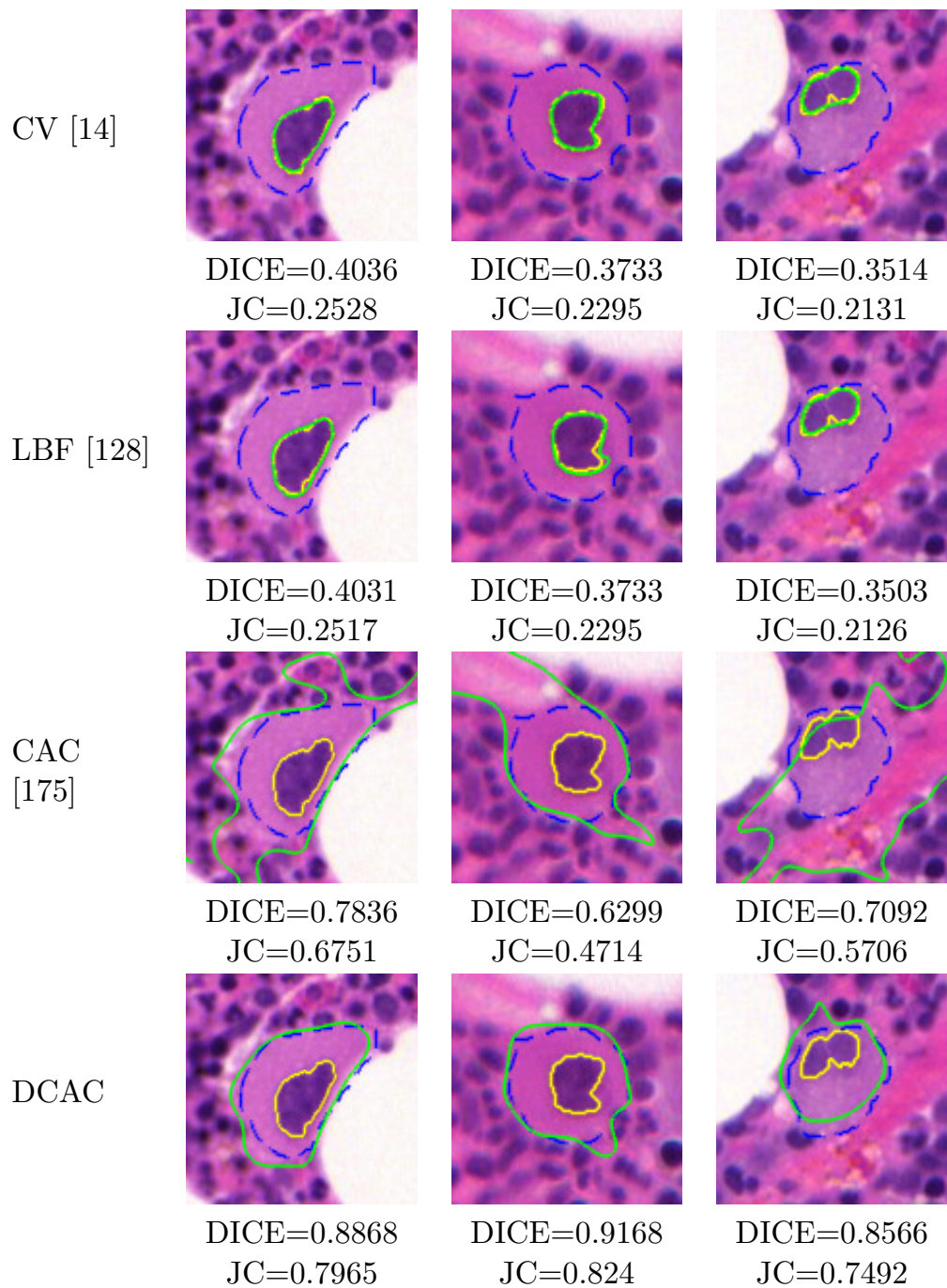


Figure 3.12: Visual results of CV model (first row), LBF model (second row), CAC model (third row) and DCAC model (fourth row). The yellow line denotes the initial contour; the green line denotes the final result and the blue dashed line denotes the ground truth.

wide enough to provide enough information to compute the external energy force. Empirical evaluations on the test images show that a width of $\gamma = 5$ pixels provides a high delineation accuracy.

The time step τ is set to 0.99 for all evaluated models. I use up to five hundred iterations. It is important to mention that all evaluated models, except for the LBF model, have a criterion to stop the evolution process [14, 128]. Fig. 3.12 shows visual results of the four models for four MKs in different images, as compared to the ground truth. Note that the proposed DCAC model visually attains a better performance than the other three models, particularly when the MK is surrounded by a non-smooth region. According to Fig. 3.12, the CV and LBF models fail to detect the cytoplasmic boundary as the evolving contour does not achieve convergence and shrinks back to the original contour. Let us recall that the CV model attempts to minimize the difference between the energy associated with the internal and external regions of the evolving contour. However, if the external region is non-smooth, the corresponding force may cause the contour to shrink back to the initial contour. The LBF model considers the local region surrounding the evolving contour to reduce any negative effects associated with non-smooth regions. However, the results show that the evolving contour of the LBF model also shrinks back to the initial contour (see Fig. 3.12). This is mainly due to the fact that the inside region of the evolving contour includes the highly smooth nuclear region, and therefore, the energy term associated with the outside region is overwhelmed by the inside region force, forcing the contour to shrink back. Note that although the CAC model is capable of expanding the evolving contour towards the cytoplasmic boundary, it results in over-segmentation due to the difficulty of converging within the non-smooth region surrounding the MK cytoplasm and the similarity in intensities between the MK cytoplasm and other tissues surrounding it.

To quantitatively evaluate the performance of these four models, I use the

Dice similarity coefficient (DICE) and the Jaccard coefficient (JC), which measure the similarity between the ground truth and the delineated areas. DICE and JC values are zero for the worst delineation results and one for perfect delineation. These two coefficients can estimate the similarity between the ground truth and the segmented images. The formulation of Dice similarity coefficient is given as:

$$Dice(X, Y) = \frac{2|X \cap Y|}{|X| + |Y|} \quad (3.29)$$

and Jaccard coefficient (JC) can be written as:

$$JC(X, Y) = \frac{|X \cap Y|}{|X \cup Y|}, \quad (3.30)$$

where X and Y represent the cytoplasmic regions of the ground truth and the segmented results respectively. Table 3.3 lists the average, minimum and maximum DICE and JC values for all test images. Note that the proposed DCAC model provides better performance than that attained by Ballaro’s method, mainly because their method uses morphological processing steps that may not be suitable for segmenting inhomogeneous or non-smooth regions. Table 3.3 also gives the average number of iterations and average computational time at which each model achieves convergence according to their stop criterion. I can see that the proposed DCAC model attains better performance than the other three evaluated models, with average DICE and JC values of 0.8509 and 0.73, respectively. As expected, the CV and LBF models obtain similarly low average DICE and JC values (0.3599 and 0.2328, respectively) because their evolving contours tend to shrink back to the initial contour when the outside region surrounding the cytoplasm is non-smooth, as previously discussed. This table also shows that the average number of iterations and computational time required by the DCAC model is lower than that required by the other evaluated models. This shows that the forces employed by the proposed model can help the evolving contour to quickly reach the desired boundary

Table 3.3: Average of accuracy, number of iterations and run times of Ballaro’s method and four evaluated active contour models for delineating MKs

| AC models | | Avg | Std | Min | Max | Iteration | Time(sec) |
|----------------------------|------|---------------|--------|--------|--------|--------------|-------------|
| Ballaro’s method [96, 174] | DICE | 0.5266 | 0.1383 | 0.3355 | 0.7679 | — | — |
| | JC | 0.369 | 0.1337 | 0.2015 | 0.6232 | | |
| CV [14] | DICE | 0.3599 | 0.1354 | 0.0394 | 0.7237 | 452.1 | 54.5 |
| | JC | 0.2328 | 0.1625 | 0.0201 | 0.5671 | | |
| LBF [128] | DICE | 0.3583 | 0.1348 | 0.0394 | 0.7218 | 500 | 61.2 |
| | JC | 0.2312 | 0.1618 | 0.0201 | 0.5658 | | |
| CAC [175] | DICE | 0.6482 | 0.1178 | 0.5215 | 0.8215 | 383.6 | 48.7 |
| | JC | 0.5215 | 0.1481 | 0.3862 | 0.6972 | | |
| Proposed DCAC model | DICE | 0.8509 | 0.0715 | 0.6712 | 0.9437 | 187.3 | 24.4 |
| | JC | 0.73 | 0.0938 | 0.557 | 0.8947 | | |

and achieve convergence.

It is important to recall that the proposed DCAC model employs the ring-like region to reduce any negative effects of the non-smooth regions surrounding the MK cytoplasm on the contour’s expansion. This idea is similar to the narrow-band active contour model in [180,181], with the main difference being that I only consider the outside ring-like region to restrict the external energy force. Although this ring-like region efficiently prevents over-segmentation, there may still be leakages as the proposed model uses global features obtained from the deconvolved stain channels, which may still depict cytoplasmic regions with weak edges. Local information, such as gradient value or orientation, will be introduced to improve the DCAC model [182]. This part will be considered to add in further work.

3.4.3 Comparison with Multi-Region Active Contour Model

I also compare the entire proposed framework with the multi-region active contour model in [139] using the images and ground truth used in the second experiment. The multi-region active contour model allows delineating the nuclear and cytoplasmic boundaries simultaneously. Since the parameters in this model should be manually set for each image, I use a set of optimal parameters that provide the best performance for all the test images. The values of these parameters are given in

Table 3.4: Segmentation accuracy of the proposed framework and the multi-region active contour model for MK cell, nuclear and cytoplasmic regions

| Active contour models | | Cell | Nuclei | Cytoplasm |
|--------------------------|------|----------------------|----------------------|----------------------|
| Multi-region model [139] | DICE | 0.8706±0.0339 | 0.7103±0.1902 | 0.7485±0.0822 |
| | JC | 0.7542±0.0821 | 0.5676±0.1776 | 0.586±0.1017 |
| Proposed DCAC model | DICE | 0.8829±0.03 | 0.9599±0.0452 | 0.8557±0.0448 |
| | JC | 0.7836±0.0569 | 0.9262±0.0799 | 0.7417±0.0681 |

Table 3.2. I use the same post-processing to smooth the shape of detected MK cytoplasmic boundary in both evaluated methods. Fig. 3.13 shows visual results of the two methods for five MKs in different images.

I also employ DICE and JC to quantify the accuracy of my entire framework and the multi-region active contour model in delineating MKs, including nuclear and cytoplasmic regions individually. These quantitative results are listed in Table 3.4. According to Table 3.4 and Fig. 3.13, both models can obtain very similar results for cell delineation, but the proposed framework provides better performance for the case of individual nucleus and cytoplasm delineation. The accuracy level attained by the multi-region model for nucleus delineation may be due to the fact that this model simultaneously segments two regions by calculating the geometrical constraint energy terms for each region, which result in one contour’s movement affecting to the other’s. In other words, this model favors similar shapes for both contours. It is important to mention that in [139], the authors also propose a model that does not favor similar shapes (i.e., it is oblivious to the shapes). This model may improve the accuracy of nucleus and cytoplasm delineation, especially if these regions are delineated by strong edges. The proposed framework delineates nuclear and cytoplasmic boundaries as two separate but consecutive steps. Moreover, the proposed DCAC model collects information from the H- and E-channel images to efficiently control the contour’s movement towards the cytoplasmic boundary. The two channel images provide information to compute the external energy force required to efficiently differentiate MK cytoplasmic regions from other tissue constituents. This helps to


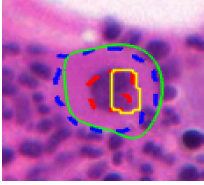


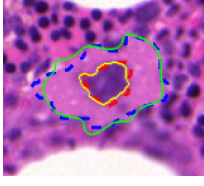
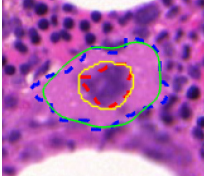
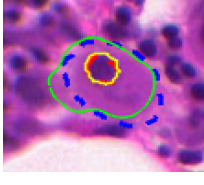
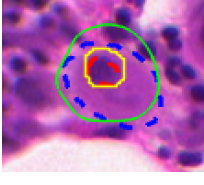

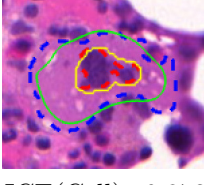
| Proposed Model | MRAC [139] |
|---|--|
|  |  |
| DICE(Cell)=0.9227 DICE(Cyto)= 0.9031 | DICE(Cell)=0.8766 DICE(Cyto)=0.7532 |
|  |  |
| DICE(Cell)=0.9004 DICE(Cyto)= 0.888 | DICE(Cell)=0.9161 DICE(Cyto)=0.8532 |
|  |  |
| DICE(Cell)=0.9295 DICE(Cyto)= 0.9152 | DICE(Cell)=0.9265 DICE(Cyto)=0.8347 |
|  |  |
| DICE(Cell)=0.8354 DICE(Cyto)= 0.8121 | DICE(Cell)=0.8105 DICE(Cyto)=0.7352 |
|  |  |
| DICE(Cell)=0.894 DICE(Cyto)= 0.8771 | DICE(Cell)=0.8722 DICE(Cyto)=0.7757 |

Figure 3.13: Visual results of my entire proposed framework (left column) and the multi-region active contour model (right column) for delineation of MK nuclear and cytoplasmic boundaries. Yellow contours denote the identified nuclear boundaries; green contours denote the identified cytoplasmic boundaries; red and blue dashed contours denote the ground truth of nuclear and cytoplasmic boundaries, respectively.

control the contour's expansion and prevent oversegmentation.

3.5 Summary

In this chapter, I presented a framework to delineate megakaryocytes (MKs) in bone marrow trephine histology images. The framework first delineates MK nuclei by using color and texture features in a supervised machine learning approach. To delineate MK cytoplasm, the framework uses a novel dual-channel active contour (DCAC) model that employs the previously delineated nuclear boundary as the initial contour, as well as intensity features of the constituent stain channel images. Specifically, the proposed DCAC model employs the Hematoxylin and Eosin channel images to efficiently determine the extent of MK cytoplasm under the observation that the cytoplasm is usually surrounded by non-smooth regions. The DCAC model also uses a ring-like region to restrict the contour's evolution and prevent over-segmentation. Experimental results show that the proposed framework can accurately delineate both MK nuclei and cytoplasm, providing more accurate results with low variability and computational time than those obtained by recent methods. I showed that the proposed DCAC model is particularly successful in delineating MK cytoplasmic boundaries delimited by weak edges and partially occluded by nearby cells or other non-MK cytoplasmic regions. After efficiently delineating MKs by the proposed framework with DCAC model, the various types of non-MK stem cells attract my attention. I would like to identify and realize these non-MK cells to look for potential clues or specific features for helping pathologists find important criteria of distinguishing ET and prefibrotic PMF.

Chapter 4

Cell Detection via Hybrid Deep Autoencoder

4.1 Introduction

In bone marrow diseases, the hematopoietic cells proliferate abnormally and quantitative measurement of cells is an essential diagnostic tool for pathological measurements that help distinguish different types of bone marrow diseases in routine clinical diagnosis. As I mentioned before, inter-observer variability exists among histopathologists for MPNs diagnosis [13]. Moreover, this study [13] points out the low individual inter-observer agreement not only on MK cellularity criteria but on other types of bone marrow cells, such as erythroid and myeloid cells. However, quantitative estimation of these non-MK bone marrow is largely subjective and manual quantification is laborious and hugely time-consuming [101, 183]. In order to address and overcome these challenges, automated cell detection is an important step in the quantification of cell based-experiments but is a difficult task, especially due to the complicated cellular characteristics of histopathological images. Most current nuclear or cell detection methods are based on exploiting low-level hand-crafted features [29], such as color, edge, contextual information, and texture; they

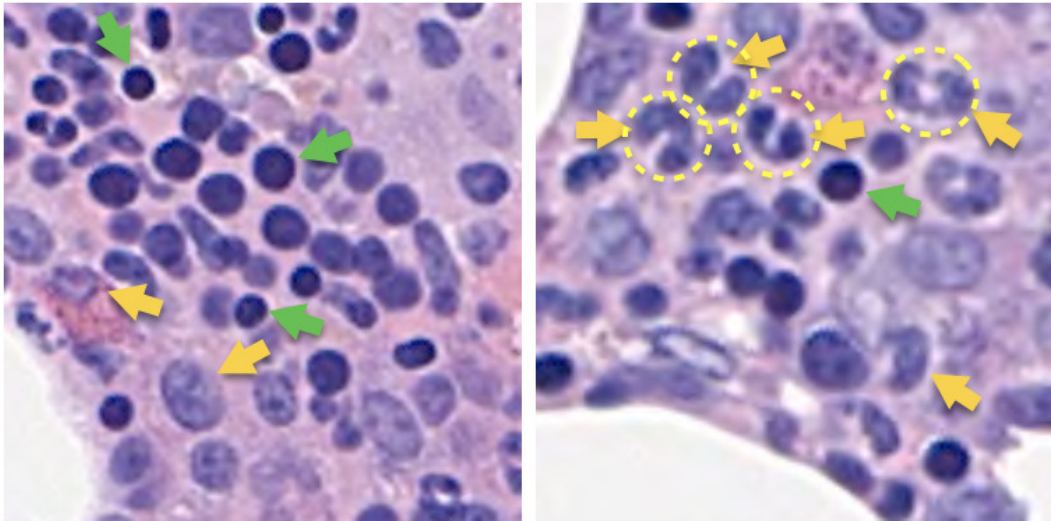


Figure 4.1: Many examples of bone marrow hematopoietic stem cells ($40\times$). We observe that there are different types of cells densely mixing and randomly distributed in bone marrow tissue. Green and yellow arrows point out erythroid cells and myeloid cells, respectively. Some specific shaped myeloid cells are shown in yellow circles.

rely on the shape of nuclei and stability of features. However, in bone marrow trephine specimens, as can be seen in Fig. 4.1, there are a large number of different types of cells mixing, which have variable sizes, shapes and textures. Hence, I need to develop algorithms for automated detection of bone marrow cells that take into account this variability.

In this chapter, I present a novel hybrid deep learning approach to detect these various cells in bone marrow biopsy images based on a novel deep autoencoder (AE). The proposed hybrid deep learning approach is based on two premises: (a) an object (nucleus or cell) with irregular shape can be represented as a Gaussian-like model to identify the center point in probability response map of the object, and (b) the original object can efficiently convert to its corresponding Gaussian-like labeled map and the center of the object can be predicted according to the properties of a specialized Gaussian model. The proposed deep learning network first estimates the properties of training data to generate the corresponding probability response map by using curve-support Gaussian model, which can help us to cater

for irregular-shaped cell or nuclear detection. Then I construct a hybrid AE-based network, named hybrid deep AE (HDAE), trained by using the input images and the corresponding probability responses to directly convert an input image to its predicted probability response map, which represents the center location based on a Gaussian-like model. Finally, I use a post-processing step to find the high probability values as local maximal points to obtain the centroids of the cells. I compare the proposed method with other common and state-of-the-art approaches of nuclei detection, and the proposed method provides better performance of detection than others. The proposed approach uses a small patch instead of the whole image to train the networks because a small patch efficiently provides the local essential characteristics of a single object to link to the corresponding curve-support Gaussian shape for spatially locating the center of the object.

The organization of this chapter is as follows. The Section 4.2 describes the proposed approach in detail, and experimental results and discussion are presented in Section 4.3. The conclusion is in Section 4.4.

4.2 The Proposed Method

The proposed approach utilizes a curve-support Gaussian model [184] to generate the probability label dataset corresponding to the input images. Then I design an unsupervised HDAE network to obtain the probability response map, which emphasizes the centroid response of each cell. I then use a post-processing step to identify the local maximal probability response as the center point of a cell.

4.2.1 Curve-Support Gaussian Model

Gaussian model is widely applied to nucleus and cell detection because the representation and properties of Gaussian are quite similar to that of round nucleus and cell. For irregularly shaped cells, the Gaussian model cannot efficiently reflect their

morphological properties. For resolving this issue, I employ the curve-support Gaussian model [184] to generate the probability response map. Curve-support Gaussian method has been used to detect the irregular shapes or ridges of biological structures, such as dendritic trees and corneal nerve fibers [184]. This model simultaneously takes into account rotation, scale and curvature to relax shape assumptions for accurately representing target structures. Here, for generating corresponding training label data, I use this model to represent the probability response map of different shapes of cells under the observation that the peak of a curve-support Gaussian corresponds to the centroid of cell, similar to the case of a Gaussian. From each input training patch, I can estimate the morphological properties to reconstruct the curve-support Gaussian probability response map. The formulation of a curve-support Gaussian model is as below:

$$CG(\hat{x}, \hat{y}; \sigma, \theta, k) = \frac{1}{\sqrt{2\pi\sigma_x^2}} e^{-\frac{\hat{x}^2}{2\sigma_x^2}} \frac{1}{\sqrt{2\pi\sigma_y^2}} e^{-\frac{(\hat{y}+k\hat{x}^2)^2}{2\sigma_y^2}}, \quad (4.1)$$

$$\hat{x} = x\cos\theta - y\sin\theta, \quad \hat{y} = x\sin\theta + y\cos\theta, \quad (4.2)$$

where k controls the level of curve of the Gaussian. The first term of Eq. 4.2 controls the longitudinal Gaussian profile of the model, while the second term controls the cross-sectional Gaussian profile. When the parameter k increases, the curve of the Gaussian becomes steeper. Fig. 4.2 shows the sample process that input training patches convert to their corresponding probability maps via curve-support Gaussian model with different levels of curve and orientation. In Fig. 4.2, there are two steps to generate a hand-crafted curve-support Gaussian label map according to its input images. First, I manually capture the shape of individual nucleus or cell and obtain the binary map. Then I estimate the parameters that curve-support Gaussian model uses from these binary maps to reconstruct them to curve Gaussian responses as the training probability maps.

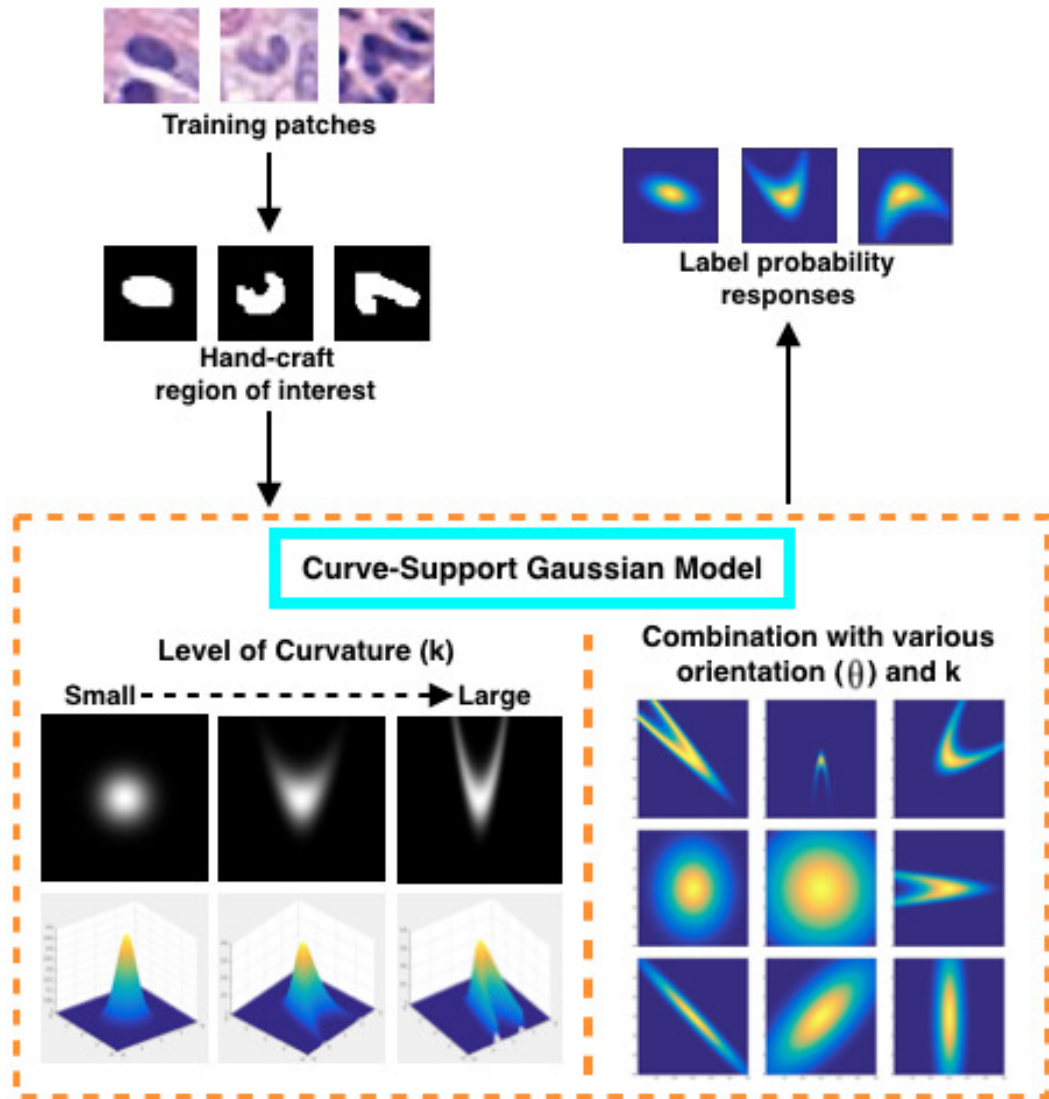


Figure 4.2: Some examples of input images and corresponding probability maps by using the curve-support Gaussian model. The parameter k controls the level of curvature. When k increases, the level of curvature becomes bigger. In addition, the parameter θ manages the orientation of curve-support Gaussian model. In the bottom right, there are some probability maps generated by combining different k and θ .

4.2.2 Training of Encoder and Decoder networks

The proposed network is inspired by the coupled network [185], which is based on the transformation of low-resolution images into high-resolution images. Similar to the concept of the coupled network, the proposed HDAE network converts the input image to the probability response map for identifying the centroids of cells. At first, I am going to generate the high-level features of input images and probability maps. As I mentioned in Section 2.2.3.2, AE is a kind of unsupervised learning method and is usually used to extract a high-level compressed representation by encoding input data. Here I build two different AE networks for obtaining the high-level features of input images and probability maps, respectively. According to the properties of AE, encoding section extracts high-level features from the original input data and decoding section reconstructs these features back to original input data. Formally, given a set of samples $X = [x_1, x_2, \dots, x_N]$ and a set of probability response maps $Y = [y_1, y_2, \dots, y_N]$, the formulations of encoding and decoding sections in these two AE networks are shown as:

$$\begin{cases} h_i^I = f(W_{l^I} x_i + b_{l^I}) \\ \hat{x}_i = f(W'_{l^I} h_i^I + b'_{l^I}) \end{cases} \quad (4.3)$$

$$\begin{cases} h_i^P = f(W_{l^P} y_i + b_{l^P}) \\ \hat{y}_i = f(W'_{l^P} h_i^P + b'_{l^P}), \end{cases} \quad (4.4)$$

where the two AEs generate the hidden representations h^I and h^P , which are intrinsic representations of input AE \mathcal{N}_I and probability label AE \mathcal{N}_P , $f(\bullet)$ is the activation function, which is set as a sigmoid function, l^I and l^P represent the number of layers in \mathcal{N}_I and \mathcal{N}_P , respectively, W and b are the weight matrix and bias terms in the encoding section, respectively, while W' and b' denote the same in the decoding section.

4.2.3 The Connecting Layer

After obtaining the high-level representation of both AE networks for input data and corresponding probability maps, I need a layer to connect the two networks. Here I notice that the input hidden representation h^I and the probability hidden representation h^P are similar because input images and corresponding probability response maps essentially represent the same objects. In order to connect these high-level features, according to the properties of AE, another network is constructed to extract and emphasize more important and related high-level features between these two feature representations. This network is built by AE and end-to-end neural networks and called the connect network \mathcal{N}_C . The formulation of the end-to-end connect network in \mathcal{N}_C is as follows:

$$\begin{cases} h_i^c = f(W_c h_i^I + b_c) \\ \hat{h}_i^P = f(W'_c h_i^c + b'_c), \end{cases} \quad (4.5)$$

and the AE in \mathcal{N}_C is shown as:

$$\begin{cases} h_i^{l^C} = f(W_{l^C} h_i^c + b_{l^C}) \\ \hat{h}_i^{l^C} = f(W'_{l^C} h_i^{l^C} + b'_{l^C}), \end{cases} \quad (4.6)$$

where h^c is the hidden representation of the end-to-end NN in \mathcal{N}_C network and \hat{h}^P is the reconstructed hidden representation of the probability response map. h^{l^C} represents the hidden features of AE in \mathcal{N}_C and l^C is the number of layer in the AE of \mathcal{N}_C network. The AE structure in \mathcal{N}_C network is used to strongly connect similar feature responses between h^c and h^P and to reduce the influence of unnecessary and non-significant features. The loss function of the connect network is as follows:

$$Loss^c = \sum_i \|h_i^P - \hat{h}_i^P\|^2. \quad (4.7)$$

The purpose of the connect network \mathcal{N}_C is to encode the hidden representation of input images and then convert them to the hidden representation of probability response maps. Here I note that the AE in connect network \mathcal{N}_C maintains decoding section to the entire connect network. The AE layer in the \mathcal{N}_C network is useful to capture much similar high-level features from the two high-level features layers and strengthen the processing of converting from input images to probability map. Fig. 4.3 shows each network component in the proposed network.

4.3 Hybrid Deep Autoencoder

Currently, I have obtained three AE networks \mathcal{N}_I , \mathcal{N}_P , and \mathcal{N}_C . For the purpose of constructing the AE-based transformation model, I capture the encoder from the AE \mathcal{N}_I and the decoder from the AE \mathcal{N}_P , and then I introduce the AE \mathcal{N}_C connect network to link the encoder and the decoder sections from the previous two AE networks (shown in Fig. 4.3). In the experiments, I found that the number of encoding hidden representation, h^I , should be equal to the number of decoding hidden representation, h^P . It means that the encoding and decoding hidden layers provide same kind of morphological and texture feature representations because each neuron of hidden layer represents a characteristic of given data. Then I would like to correlate the encoding feature representation with the decoding one to efficiently convert input images to probability responses.

In order to achieve this purpose, I use another network, which combines an AE network and an AE-based end-to-end network, to connect these two parts, namely the connect layer network \mathcal{N}_C . The \mathcal{N}_I and \mathcal{N}_P networks obtain the high-level features from the input images and the probability response maps, respectively. In essence these two high-level features should be similar because the input images and the corresponding probability response maps represent the same objects. In order to connect these high-level features, according to the properties of AE, the

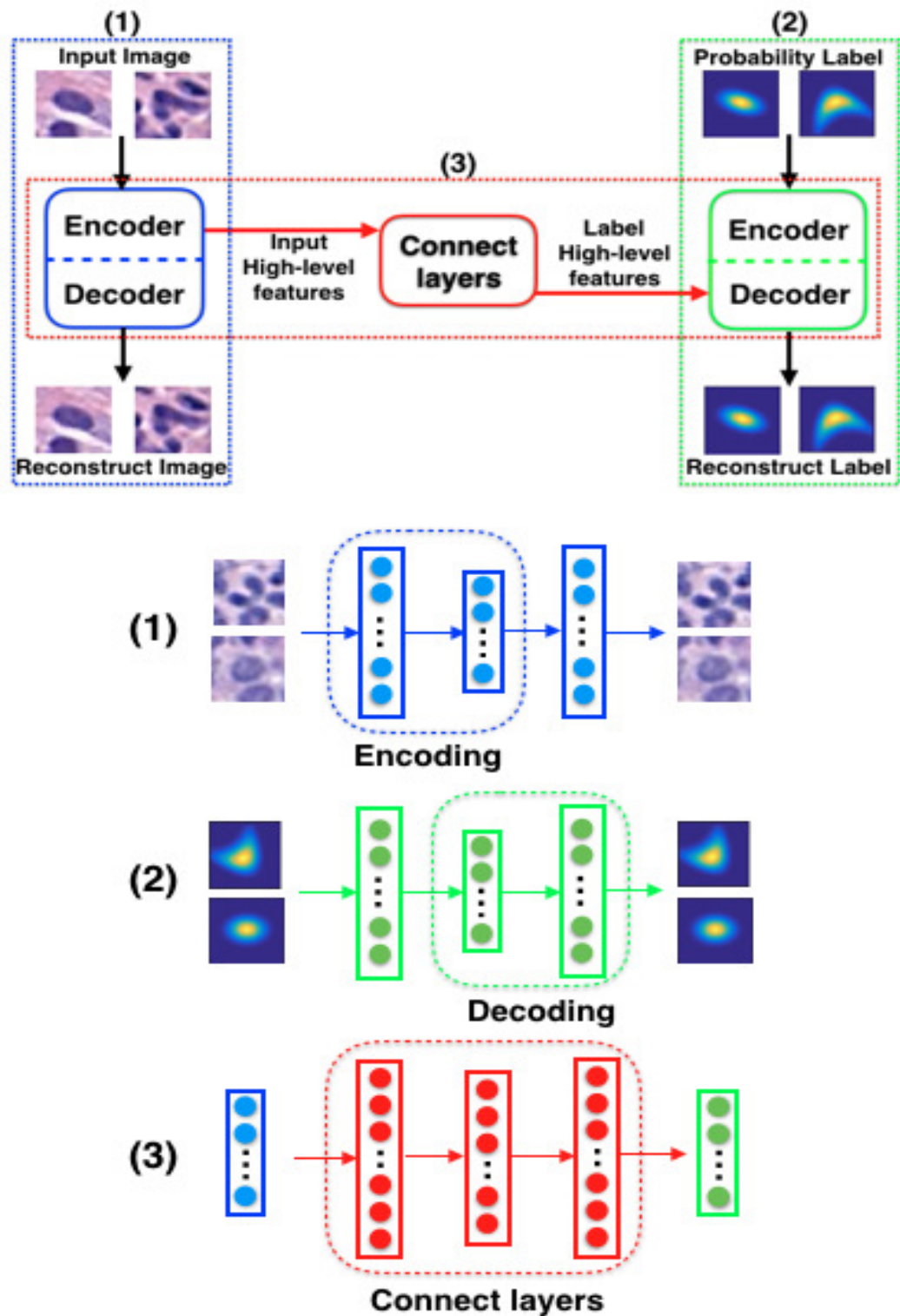


Figure 4.3: An overview of the proposed HDAE network. The top part of the Figure shows the whole structure of HDAE and the bottom part presents three sections to form final structure: (1) input AE network, (2) probability label AE network and (3) connect layer network.

\mathcal{N}_C network extracts and emphasizes more important and related high-level features between these two feature layers.

After the pre-training of each single AE network, I collect the resulting parameters and rebuild the HDAE network. Individual training for each set of parameters may result in high reconstruction error when they are combined. Therefore, I need a fine-tuning step to refine and optimize the resulting parameters by backpropagation. HDAE adopts the given parameters $\Theta = \{W_{l^I}, W_c, W'_c, W'_{l^P}\}$ to convert the input sample images to corresponding probability response maps. The complete setup of the proposed HDAE network can be described as follows:

$$\begin{cases} h_i^I = f(W_{l^I}x_i + b_{l^I}) \\ h_i^c = f(W_ch_i^I + b_c) \\ \hat{h}_i^P = f(W'_c h_i^c + b'_c) \\ \hat{y}_i^{HDAE} = f(W'_{l^P} \hat{h}_i^P + b'_{l^P}), \end{cases} \quad (4.8)$$

and the fine-tuning objective function is as follow:

$$Loss = \sum_i \|y_i - \hat{y}_i^{HDAE}\|^2. \quad (4.9)$$

Here I notice that the high-level feature representation h_i^c is reconstructed by enhancing higher level correlative features in the connect network (4.6). Moreover, this loss function of HDAE is similar to probability label network, but \hat{y}_i^{HDAE} is reconstructed via a complete hybrid network. The feature representation h_i^I , h_i^c and h_i^P follow (4.3), (4.5), and (4.4), respectively.

Finally, in order to detect the centers of nuclei from a large image, I use the sliding window strategy with overlapping window. After obtaining the probability response map of cell centroids, I find the local maxima from the probability map. In order to avoid over-detection, a fixed threshold is introduced, which is empirically

determined from the training data set in the experiments. All local maxima whose probability values are less than the threshold are not considered in the detection.

4.4 Experimental Results

I compare the proposed HDAE with other recent approaches of detection and show that the proposed algorithm attains the best performance among the compared methods for bone marrow trephine images.

4.4.1 The Dataset

The dataset involves a set of digitized images of 52 H&E stained biopsy samples that are obtained from 5 ET and 5 prefibrotic PMF cases at UHCW. The size of each image is about 700×1000 pixels and all images were cropped from non-overlapping regions of these 10 cases. The H&E stained bone marrow trephine biopsy glass slides were scanned into a computer using an Omyx VL120 scanner at a resolution $0.275 \mu\text{m}/\text{pixel}$ (equivalent to $40 \times$ optical magnification). I selected the cropped areas that represent a variety of cell appearance and distribution from both different cases. These images were randomly split into two groups for training and testing sets. For preventing over-fitting problem, I randomly split these images into two groups (2-fold cross validation, i.e. 26 images for each fold) for training and testing sets.

4.4.2 Network Architectures Setting

The architecture of HDAE network consists of input layer, input AE encoding layers, connect network layers, and probability AE decoding layers. The patch size is defined as 29×29 pixels which is big enough to contain a whole nucleus within the patch under $40 \times$ optical magnification resolution images. Each patch size has RGB color channels and one stain channel, which is the Hematoxylin channel. The Hema-

Table 4.1: Architectures and parameter setting of HDAE network. The network consists of input network N_I , connect network N_C , and probability network N_P .

| Layer | Type | | Input/Output Dimensions |
|-------|--------------|---|-------------------------|
| 0 | Input layer | | $29^2 \times 4$ |
| 1 | N_I | 1 | 1200 |
| 2 | | 2 | 400 |
| 3 | N_C | 1 | 625 |
| 4 | | 2 | 324 |
| 5 | | 3 | 625 |
| 6 | N_P | | 400 |
| | Output layer | | 29^2 |

toxylin channel can efficiently stain the nuclei to obtain nuclear local information due to nucleus acid and also represents morphological and texture information of nuclei with color channels. I use a recently proposed color deconvolution approach [42] to obtain the Hematoxylin channel intensity.

In input layer of HDAE network, the input is the vector of pixel intensities corresponding to a square patch with channels I use. This vector is represented as a column vector of pixel intensities with size $(29^2 \times 4)$. Moreover, the input AE encoding layers \mathcal{N}_I has two hidden layers and then there is a encoding-decoding AE structure, including three hidden layers, in the connect network \mathcal{N}_C . In the probability AE decoding layers \mathcal{N}_P , there is one hidden layer and the size of output is $(29^2 \times 1)$, which is the probability response map. The details of each layer in the HDAE network are shown in Table 4.1.

It is worth noting that if I set the number of hidden units become to be much smaller, such as quarter of the number of input units, the results of testing data deteriorate because of the compression property of the AEs. In addition, in order to avoid over-fitting, dropout is implemented in the HDAE network with a dropout rate of 0.2.

Here the weights are initialized for each layer by using a scaled uniform

distribution in the range between [186, 187]:

$$-0.5 \times 2 \times 4 \sqrt{\frac{6}{In_{num} + Out_{num}}} \leq W \leq 0.5 \times 2 \times 4 \sqrt{\frac{6}{In_{num} + Out_{num}}}, \quad (4.10)$$

where In_{num} and Out_{num} represent the number of input units and the number of output units, respectively. This normalized initialization is used for sigmoid activation function. Besides, all biases are set to 1. The network was trained by using adaptive moment estimation (Adam) [188], which is an optimization algorithm of stochastic gradient descent, with the momentum 0.9 and weight decay 5×10^{-4} for 300 epochs. The initial learning rate is set to 10^{-3} and adaptively adjusted by Adam method. The proposed network was implemented in Matlab R2015b.

4.4.3 Generation of Training and Testing Sets

Manual annotation of nuclei in whole image data was conducted by a junior trainee and verified by an experienced pathologist. Each nuclear patch is generated from a 29×29 square image window, employing the annotated dot as the center of the window. The size of each patch was chosen to be big enough to contain a nucleus within the patch and to contain various types of nuclei in the patch. The input dataset comprised of 11,623 nuclear patches from 52 images. I manually mark the shape of each nucleus from these input patch dataset and curve-support Gaussian model is used to generate the dataset of corresponding probability maps. The input patches and probability maps were employed for training and evaluating the proposed model.

4.4.4 Training the HDAE

I employ the greedy layer-wise approach for training the HDAE as shown in Fig. 4.3 by training each layer in a sequential manner. Here the training dataset of each fold is divided into 80% for training and 20% for validation. The training procedure

includes the following three steps: Firstly, an input AE network \mathcal{N}_I is trained to extract high-level feature representations h_i^I of image patches from training patch data and obtain the pre-trained weights W_{II} of encoding section. Then, the probability maps are used to train the probability AE network \mathcal{N}_P to generate the high-level features h_i^P of probability map and the pre-trained weights W'_{IP} of decoding section are obtained. Following this, the input high-level feature representations h_i^I are applied to train the connect network \mathcal{N}_C and the probability-level representation h_i^P are used to do the backpropagation of \mathcal{N}_C for updating the weights W_c and W'_c . Finally, the hyper-parameters $\{W_{II}, W_c, W'_c, W'_{IP}\}$ from these three pre-trained networks are assigned and optimized by fine-tuning to form the proposed HDAE network. After fine-tuning step, in order to choose the best set of hyper-parameters for evaluating the detection model, the convergence of loss function on the validation images is used and the minimum loss energy is chosen for the final set of model parameters. Local maxima and a fixed threshold value are used to efficiently remove low probability responses and identify the centroid of all types of cells.

Fig. 4.4 shows an example of visual result of the proposed HDAE network. Visual results for the probability map are shown in Fig. 4.4(b) and reveal that the pixels with high probability values are mostly located in the vicinity of the centers of nuclei. Fig. 4.4(c) shows the predicted detection result comparing with the ground truth. It demonstrates that the HDAE network can efficiently detect different types of bone marrow hematopoietic stem cells because curve-support Gaussian model represents geometric structure of individual nucleus and utilizes the properties of Gaussian model, i.e. the highest probability value is located at the center of the model. These results show that the proposed HDAE network with curve-support Gaussian model has a strong ability of detecting various nuclei shapes and precisely reflect the locations of centroids of various cells via related high-level feature correspondence between two different feature extraction networks.

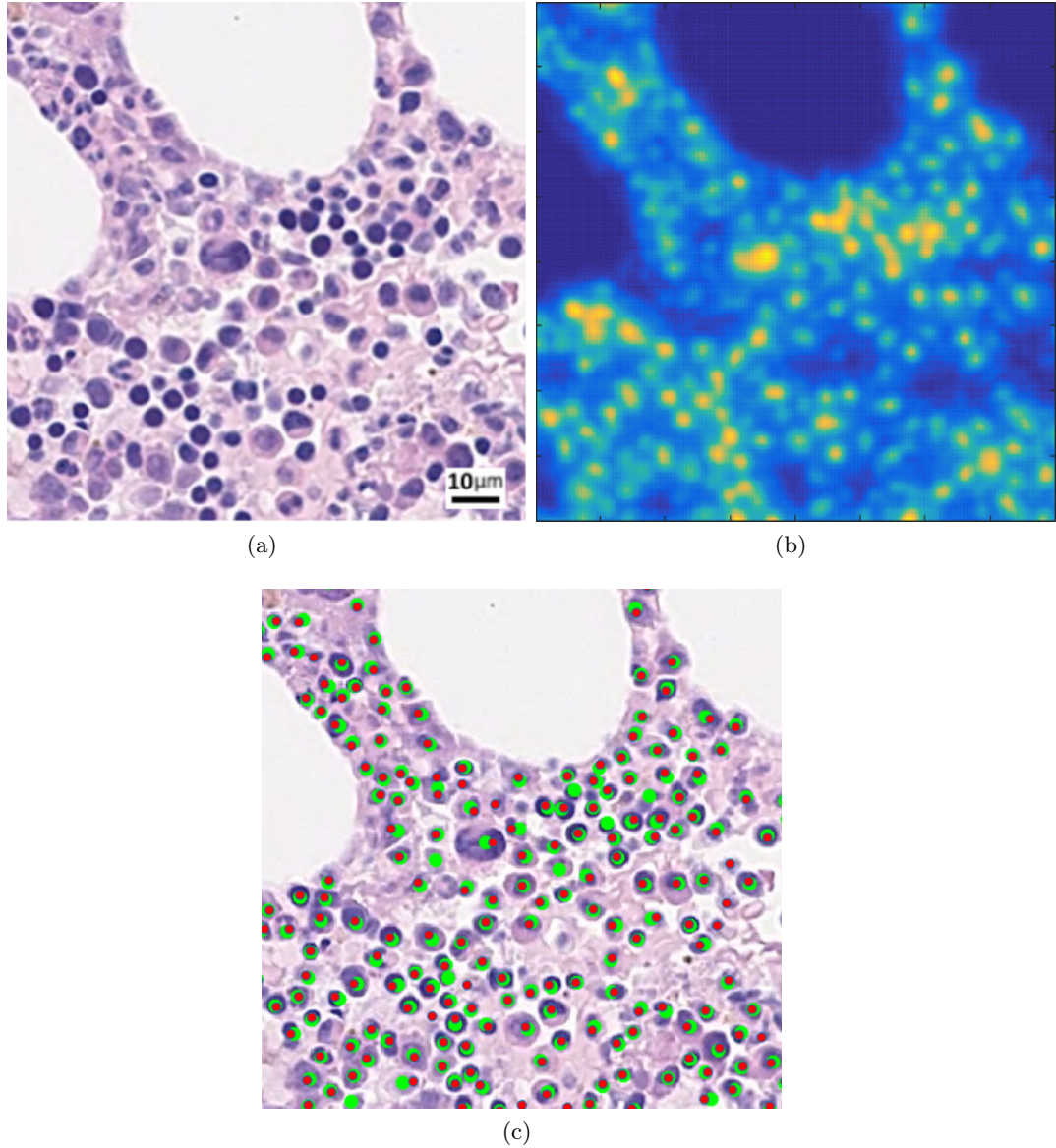


Figure 4.4: Visual results for nuclear detection via the HDAE network. (a) An example image (b) Probability map generated by the HDAE network. Detecting the center of an individual nucleus is based on the location of local maxima found in the probability map. (c) Detection results of HDAE. Here the detected centers of the nuclei are shown as red dots and ground truth areas are green shaded circles. Detection results of the proposed method and other approaches are shown in Figure 4.5 and 4.6.

4.4.5 Comparison of the proposed network with other deep learning methods

In order to assess the effectiveness of the HDAE model, I compare the performance of the proposed network with some conventional and some state-of-the-art nuclei detection algorithms. Firstly, Blue Ratio (BR) [189], which converts RGB color space to blue ratio response with Laplacian of Gaussian (LoG) filter for detection. The second method is Expectation-Maximization (EM) method [190] with geodesic active contour model which takes into account cell overlapping segmentation to detect each individual cell. Thirdly, local isotropic phase symmetry measure (LIP-SyM) [191] which yields high response values near the centers of symmetric nuclei which can be used for detection. Fourthly, stacked sparse autoencoder (SSAE) [101] which consists of two sparse AE layers with a softmax classifier which is trained to distinguish between nuclear and non-nuclear patches. If a patch is classified as a nucleus, all pixels inside of the output patch are assigned the value of 1, or 0 otherwise. Lastly, spatially constrained CNN (SC-CNN) uses spatial regression to predict the probability of a pixel being at the center of a nucleus. Here the implementations of BR, EM and SSAE algorithms for nuclei detection are based on the papers [189], [190], [101], respectively. The implementations of LIPSyM and SC-CNN methods are provided by the authors of those methods. For a fair comparison, I use the same input procedure of detecting the centers of nuclei, such as channel feature and patch size, in the SSAE and SC-CNN algorithms as that in the HDAE network.

For quantitative analysis of the detection performance among these comparing algorithms, Precision, Recall and F1-score were used to assess the detection

Table 4.2: Comparative results for detection

| Method | Precision | Recall | F1-Score |
|--------------|---------------|---------------|---------------|
| BR [189] | 0.5877 | 0.4779 | 0.5271 |
| EM [190] | 0.6388 | 0.5106 | 0.5676 |
| LIPSyM [191] | 0.6135 | 0.5266 | 0.5667 |
| SSAE [101] | 0.8733 | 0.719 | 0.7887 |
| SC-CNN [95] | 0.9517 | 0.9274 | 0.9394 |
| HDAE | 0.9273 | 0.9702 | 0.9483 |

performance. These measurements are calculated as follows:

$$\begin{cases} Precision = \frac{TP}{TP+FP} \\ Recall = \frac{TP}{TP+FN} \\ F1 - score = 2 \times \frac{Precision \times Recall}{Precision+Recall} \end{cases} \quad (4.11)$$

Here I define the region within a radius of 12 pixels, which can approximately contain the core area of a single bone marrow cell, from the annotated center of each nucleus as its ground truth. If there are multiple detected points within the same ground truth region, only the one closest to the annotated center is considered as a true positive (TP). FP and FN refer to false positive and false negative errors, respectively.

Table 4.2 shows the comparative quantitative detection performance of HDAE network and other methods. Also, Fig. 4.5 and 4.6 show the parts of sample visual results of these approaches. Overall, the comparison results indicate that the proposed approach provides F1-score over 94%, attaining the best performance among these algorithms and indicating that learning spatial and cellular context, such as SC-CNN and HDAE methods, efficiently help to predict the center of a nucleus by the probability response. The BR method requires intensity information to detect nuclei. If there are many nuclei in the dataset having weak staining, the BR method is likely to fail in those cases. The EM algorithm, which requires intensity clustering and segmentation, could not efficiently detect touching or weak stained

nuclei because weak stained nuclei could not provide stronger boundary or gradient information. In addition, LIPSyM heavily relies on bilateral symmetry of nuclei for detection. Due to this reason, it could not precisely detect touching and other irregular-shaped nuclei. The SSAE method works well on dark stained nuclei but fails on weak stained ones because it only considers pixel intensities and may identify some weak stained nuclear patches as cytoplasm regions. SC-CNN and HDAE both learn morphological and topological context to generate the probability response for detecting the center of nuclei and have better performance than other detection approaches. SC-CNN learns the spatial structure from the training output data, whereas HDAE learns the morphological and spatial structures from the training input images and probability maps, respectively, and combines them together for nuclei detection. I observe that SC-CNN provides a higher precision value because it extracts more local feature patches around the centroids of cells to precisely identify the location of centroids. SC-CNN can also detect some touching nuclei. However, it could not efficiently take into account some types of nuclear shapes, such as U-shaped nuclei or the nuclear size larger than patch size. Moreover, SC-CNN does not have good performance on the nuclei with weak intensity because convolutional layer reduces the impact of intensity feature and it causes that the probability value of center of a weak-intensity nucleus becomes too low to be identified (see Fig. 4.6). On the other hand, the proposed HDAE network can detect these cases because of the properties of curve-support Gaussian. HDAE can provide more advantages of efficiently reflecting the morphological and topological Gaussian-based structures of nuclei to detect these types of nuclei. To summarize, SC-CNN and HDAE can provide better ability of processing most of the cases to precisely predict the centers of nuclei in bone marrow trephine biopsy images.

Fig. 4.6 shows another sample result of the comparison among these approaches. It shows that SC-CNN is likely to fail for this case because the weak stained nuclei and various sizes of nuclei affect local geometric information extrac-

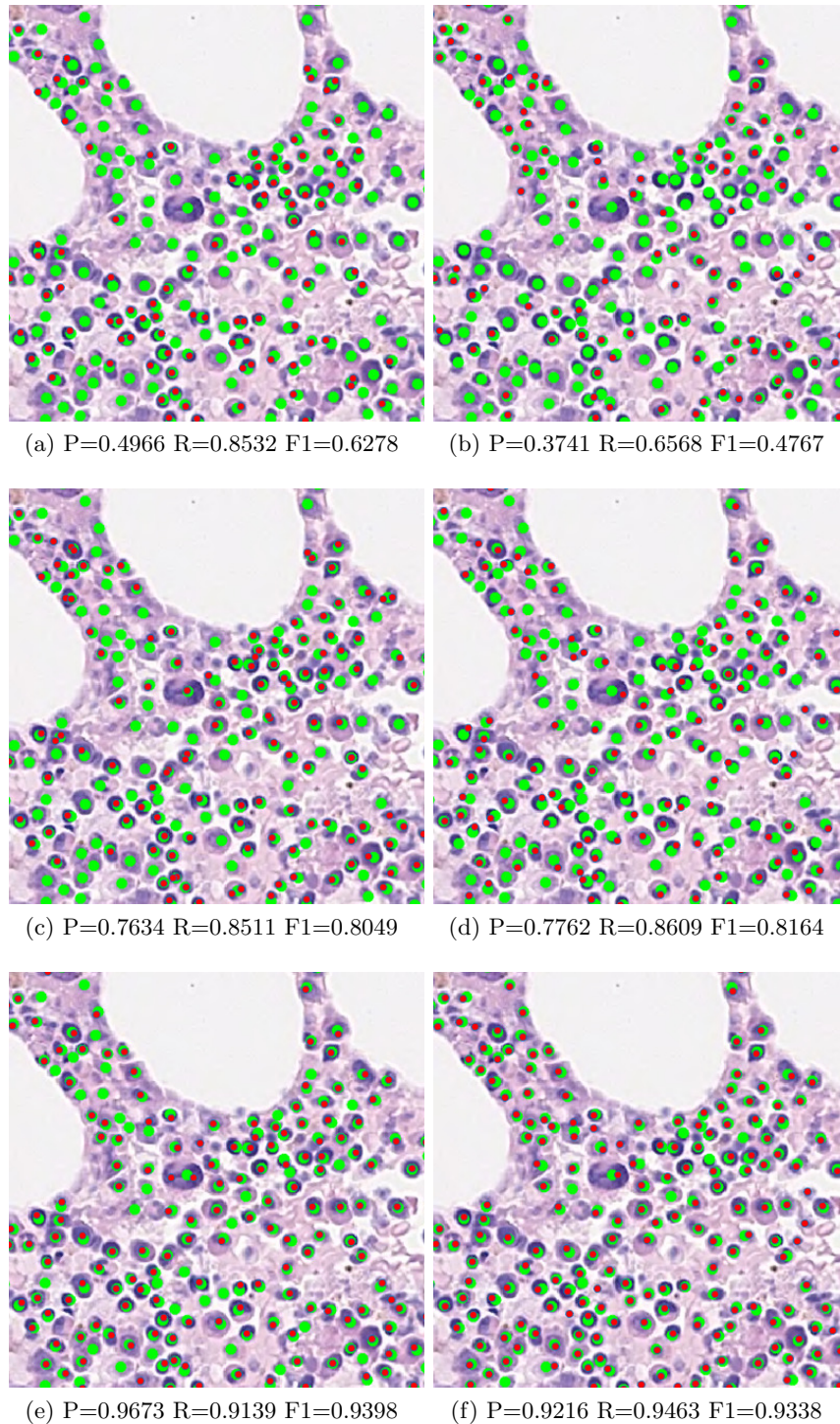


Figure 4.5: Comparative result for the proposed method and other approaches for nuclei detection on the sample image shown in Fig. 4.4(a): (a) BR, (b) EM, (c) LIP-SyM, (d) SSAE, (e) SC-CNN, (f) HDAE. The ground truth areas are represented by green shaded circle and red dots represent detected centers of nuclei. The Precision (P), Recall (R) and F1-Score (F1) are listed below each sample.

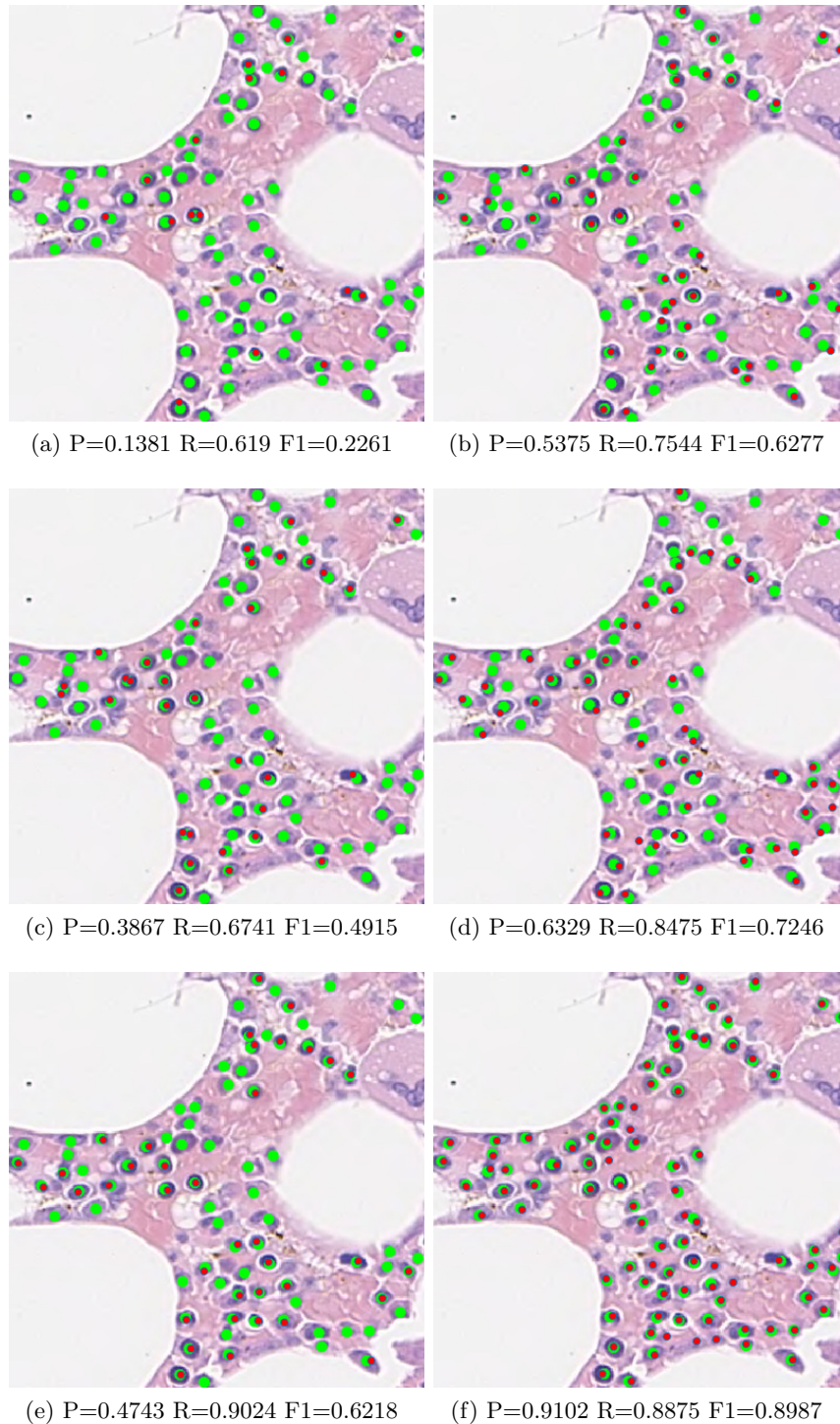


Figure 4.6: Another comparative result for the proposed method and other approaches for nuclei detection: (a) BR, (b) EM, (c) LIPSyM, (d) SSAE, (e) SC-CNN, (f) HDAE. Also, the Precision (P), Recall (R) and F1-Score (F1) are shown below each sample case. It shows that the proposed method provides better performance of nuclei detection than other conventional and learning approaches.

tion to identify the location of nuclear centers. In contrast, the HDAE network involves morphological context from the input network and topological context from the probability network to compensate the loss of local information due to the weak staining. These results show that the proposed HDAE network with curve-support Gaussian model has stronger ability of detecting various shapes and staining of nuclei and efficiently reflect the locations of centroids of nuclei via related high-level morphological and topological feature correspondences between two different feature extraction networks.

4.5 Summary

In this chapter, I have proposed a novel unsupervised AE-based network with curve-support Gaussian function designed for efficiently and precisely detecting various shapes of cells in bone marrow trephine images. A curve-support Gaussian model reconstructs the probability response label map of various morphological and topological features of cells and the proposed HDAE network efficiently combines two AE networks, both of which intrinsically represent the same targets to directly produce the probability response map from input multi-dimensional channel images through high-level feature extraction and similarity. Compared with other unsupervised and supervised deep learning approaches, the proposed HDAE network provides the best cell detection performance in bone marrow trephine biopsy images. Then I want to classify these detected centers for further investigation and quantitative analysis.

Chapter 5

A Synchronized Asymmetric Deep Learning Model for Cell Classification

5.1 Introduction

After obtaining the detected nuclear centers, the next step is to recognize the detected cells for statistical measurement and further quantitative investigation and analysis. Nuclei or cell classification is an important and routine processing step of many automated histopathological image processing techniques and analysis algorithms [29, 192]. Nuclei or cell classification can help obtain information about different cell types to help pathologists find clinical assessment rules or models for quickly producing correct diagnosis and giving efficient treatment strategies to patients. According to the WHO diagnosis criteria of MPNs [1, 183], there is no standard and efficient quantitative clinical assessment or grading system using these different bone marrow hematopoietic stem cells to help the pathologists realize cellular distribution and quantity to precisely distinguish different subtypes of MPNs. It is because the hematopoietic stem cells have various stain intensity, shape and

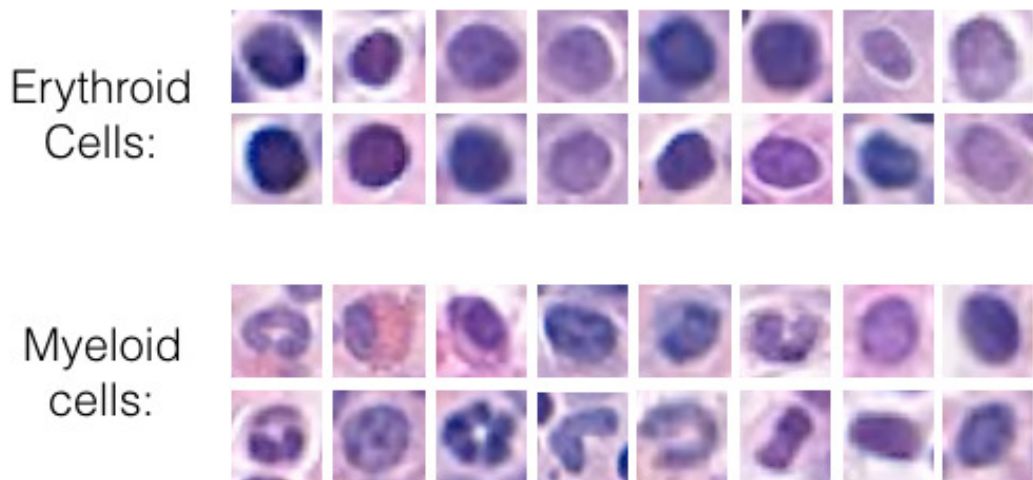


Figure 5.1: Examples of different types of bone marrow hematopoietic stem cells by H&E staining. There are two major cell types: erythroid cells and myeloid cells. The myeloid cells include several subtypes of cells but are difficult to be observed and identified by experts. Moreover, some of erythroid and myeloid samples have similar and rather fuzzy shape or intensity features (last two columns).

texture features and are massively distributed over heterogeneous structure of bone marrow trephine histopathology images. Fig. 5.1 shows examples of the two major cell types of bone marrow hematopoietic stem cells. It can be seen that some of the two types of cells exhibit similar morphological features. These factors increase the difficulty of not only manually identifying different types of bone marrow cells but segmenting and extracting cellular and tissue characteristics by using the current image processing approaches.

In order to efficiently recognize the two types of cells, I propose a novel deep learning based approach. In the previous chapter, I develop a hybrid deep AE-based network with hand-crafted features for detecting bone marrow cells with various shapes. In general, cell detection and classification are separated and assigned into two different networks, resulting in increased computational complexity for training the deep network. Here, in this chapter, a classification network is introduced and combined with the HDAE network to target detection and classification simultaneously. The proposed network can not only reduce much time of the training network

but also maintain the ability to efficiently detect and classify different types of bone marrow cells.

The organization of this chapter is as follow. A brief literature review is given in Section 5.2. The formulation and algorithm of proposed asymmetric model for detection and classification is described in Section 5.3. Finally, a comparison of the quantitative performance between the proposed model and a conventional framework in detection and classification is presented and discussed in Section 5.4 and 5.5.

5.2 Related Work

Cell classification has been applied to diverse histopathology related applications of disease diagnosis. In addition, a classification step, such as manual condition setting, clustering methods or linear classifier, is often used with segmentation or detection approaches which indicate the region or object of interest to extract specific morphological or texture features, to distinguish different types of cells. For example, Huang *et al.* [193] used multilevel thresholding based segmentation and PCA and k-mean clustering to recognize leukocytes from blood smear images. Also, during the last decade, machine learning approaches are widely applied as the classifiers based on cell or nuclear intensity, morphological, and texture features in histopathological image analysis. Theera-Umpon *et al.* [194] used fuzzy-C mean clustering and neural network to segment and classify the different series of myelocytes in bone marrow images. In [195], Ali *et al.* proposed a shape prior based AC model to segment nuclei and use morphological features with SVM for nuclei classification in prostate and breast histological images. Recently, Sharma *et al.* [196] proposed a framework including nuclei segmentation and multiple cell classification using Adaboost classifier based on intensity, morphological and texture features in gastric cancer. These approaches point out that the classification often requires other pre-

processing strategies to extract hand-crafted (morphological and intensity) features to achieve classification purposes [197].

In fact, there is relatively little work on cell classification for histopathology images because it depends on efficient preprocessing outcomes, such as nuclei segmentation, to obtain reliable feature information. The complex and heterogeneous architecture of tumor regions seriously affect accurate cellular feature extraction and then limit the evaluation on nuclei classification performance. In recent years, deep learning based approaches have been shown to be successful and powerful for the analysis of histopathological images [95, 103, 152]. There are two key concepts of DL methods: first, unlike conventional machine learning techniques, deep neural networks, such as an AE model, automatically extract and learn features by using the training data. Second, DL methods directly extract multiple high-level features because of the feed-forward hierarchical structures with multiple layers [101–103, 198]. These layers compute features from the previous layer/feature representations, and it is not widely accepted that DL networks gradually learn from low-level features to high-level features. This ability enables the DL networks to handle very complex functions and high dimensional data. For instance, Xu *et al.* [101] use the stacked sparse AE with a softmax classifier to learn a high-level representation of nuclear and non-nuclear objects for detecting and classifying the nuclear regions. In addition, Malon and Cosatto [99] trained CNN classifier for mitotic and non-mitotic cells using color, texture and shape information. Sirinukunwattana *et al.* [95] used convolutional neural networks (CNNs) to take into account nuclei detection and classification. However, detection and classification purposes in these methods are usually processed by independent DL approach and separately generate the results.

In previous chapter, the HDAE network has been efficiently used in nuclei/cell detection. In this chapter, based on the concepts and structure of HDAE network, I will rebuild HDAE model and design a synchronized DL structure to solve the detection and classification problems simultaneously.

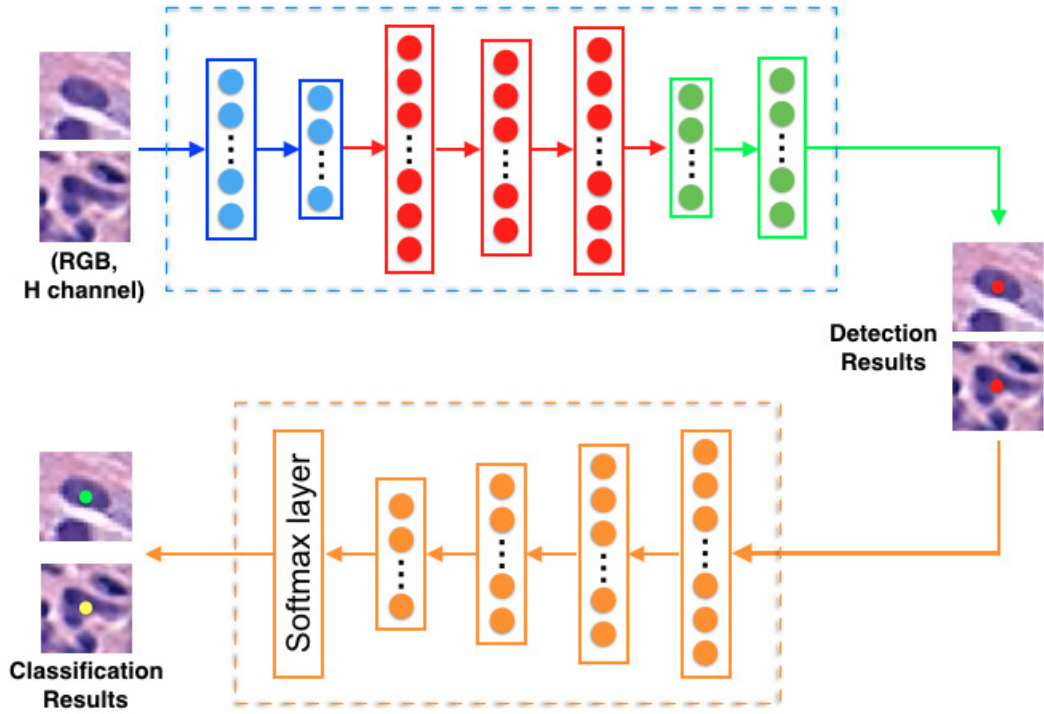


Figure 5.2: The representation of conventional progress for detection and classification via deep learning approaches. In general, there are two networks to process detection (upper dash-rectangle) and classification (bottom dash-rectangle) sequentially.

5.3 Methodology

Simultaneous detection and classification approaches deal with the location and types of nuclei for histology image analysis at the same time. Generally, these two problems are solved independently and requiring more training time. For reducing the time required for training and keeping the same performance as separated networks, the proposed approach combines the two networks to synchronize detection and classification processing steps.

5.3.1 Conventional Deep AE Structure of Classification

In general, after obtaining the detection results, classifying different types of objects is the next step of the analysis. Fig. 5.2 shows a conventional framework for

nuclear or cell detection and classification. The conventional structure includes one model for detection and one for classification. If deep learning approaches are used in both sections, it means that I need to train these two networks separately and it might take much time on training networks because the purposes of these two networks are different. For instance, we can use HDAE network and CNN method to detect and classify different nuclei. The classification part can be replaced by other learning approaches, such as softmax classifier or bag-of-words dictionary learning [199]. Specifically, I note that if a conventional stacked AE network with softmax classifier is used in the classification part, the first several layers of the stacked AE network and the first several layers of the HDAE network could learn similar color and morphological features from same image dataset. Moreover, the architectures of these two networks are similar. Therefore, I can use the HDAE for detection and a stacked AE network for classification and put them into a single parallel network to efficiently detect and classify BM hematopoietic stem cells.

5.3.2 Synchronized Hybrid Deep AE

Based on the concept of an integrated model, I would like to build a model to process the detection and classification strategies simultaneously. At first, I consider to use the same deep learning structure in both detection and classification sections. It is because if the number of hidden layers and the neurons in the encoding sections of HDAE network and a stacked AE network of classification are the same, it can be integrated as a whole encoding section to reduce processing time. In addition, according to the idea of HDAE network, the connection network can obtain correlated high-level feature representation from input and probability image data, which is similar to the high-level feature representation from input dataset in classification network. It means that the encoding section of the connection network can work with the input network and softmax classifier to be the classification learning network. In the fine-tuning, the loss energy of classification network is used to help

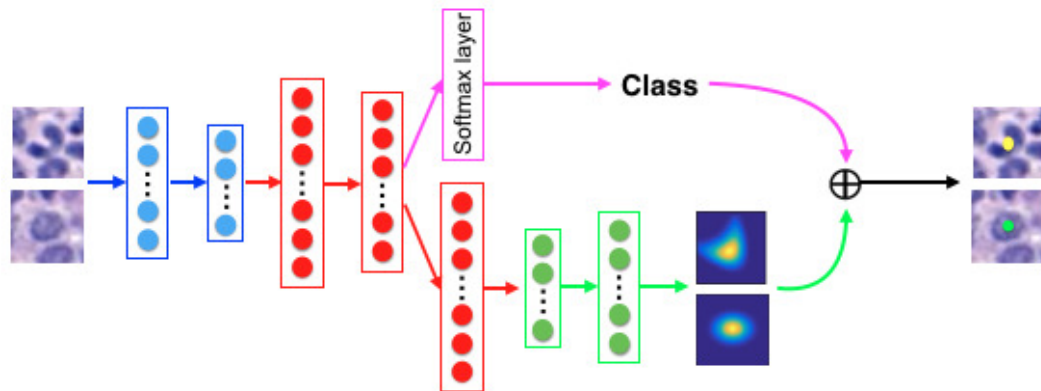


Figure 5.3: The architecture of synchronized HDAE network for detection and classification. The middle layer of connection network works with softmax classifier is used to identify different types of cells.

the encoding section of the whole synchronized network to optimize the parameters. Fig. 5.3 represents the structure of a parallel integrated model for cell detection and classification.

However, the synchronized HDAE network cannot efficiently obtain correct detection and classification results because detection and classification strategies affected each other. The probability network only learns the features from detection probability maps and doesn't include the information of classification. When the loss energy of classification is introduced in backpropagation step, it acts like noise and negatively influences the parameters' optimization for detection. In other words, for the classification section, the loss energy of detection also affects to optimize the parameters of classification to obtain incorrect outcomes. In order to efficiently avoid and reduce the influence between detection and classification strategies, I designed a new connection structure based on the HDAE network.

5.4 Synchronized Asymmetric Deep Hybrid AE (Syn-ADHA)

Due to the aforementioned reasons, I adopt a network architecture idea from Lee *et al.* [200], who proposed a concatenated asymmetric deep learning structure for capturing the distorted feature and noise estimation. According to the properties of AE-based model, input data are used to compare the reconstructed data to train the parameters of network via backpropagation, and this makes the network symmetric. If an AE-based learning model has one input and outputs two different results, it needs to combine with other networks by using specific network structure or components. In [200], the authors built an asymmetric deep denoising network to estimate the noise and reconstruct clear features from input distortion features. Inspired by this idea, I constructed a novel asymmetric learning network with HDAE model to process detection and classification at the same time.

For developing an asymmetric network, using similar learning network structures of both detection and classification is necessary to reduce the difficulty and complexity of the proposed network construction and mathematical functions. In previous work (Chapter 4), the HDAE network focuses on cell detection by connecting two AE-based networks. Moreover, as I mentioned before, a normal stacked AE network for classification has similar hierarchical structure to the input network of HDAE. I adopt this parts of HDAE and redesign the connect network, which is the key role of integrating input network, detection probability network and classification network, to achieve the abilities of detection and classification in parallel.

Fig. 5.4 shows the network structure of the improved asymmetric HDAE, also called Syn-AHDA. There are four sections in Syn-AHDA network: the input network \mathcal{N}_I , the improved probability network \mathcal{N}_{PC} , the asymmetric connect network \mathcal{N}_{AC} , and the classification network \mathcal{N}_{Class} . The input network \mathcal{N}_I in this proposed network is constructed and trained in the same way as that in HDAE

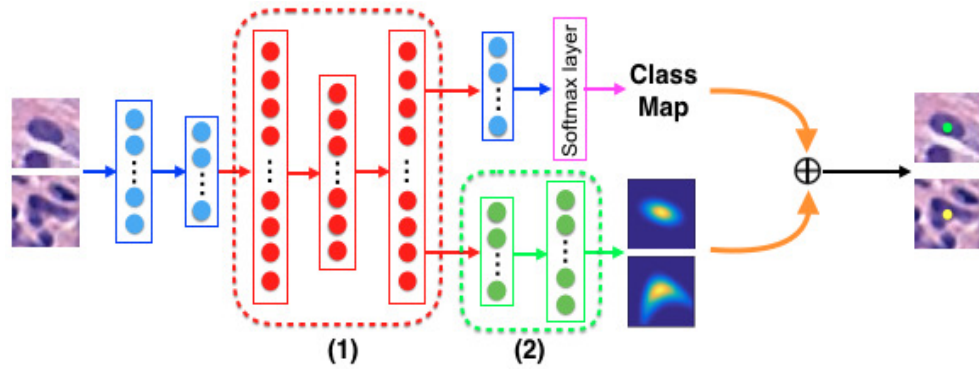


Figure 5.4: The structure representation of Syn-AHDA network. Here I construct an asymmetric learning network to detect the position of cell centers and classify different types of cells. The details of the key components: (1) asymmetric connect network and (2) probability network are shown in Fig. 5.5.

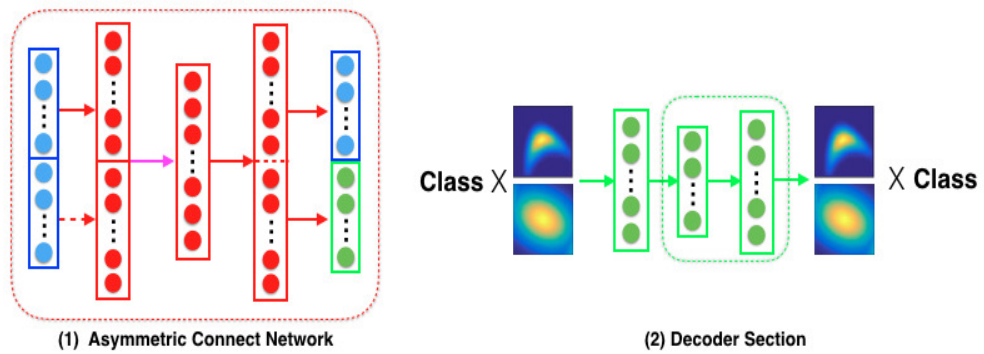


Figure 5.5: The structure of asymmetric connect network and probability network. There are two different processing sections to HDAE network in the training stage. The asymmetric connect network integrates one input vector and reconstructs two output vectors: the input vector for classification and probability label vector for detection. Moreover, the decoder of probability network is trained by the probability maps associated with corresponding class labels.

network (shown in Section 4.3). Finally, the classification network \mathcal{N}_{Class} is an AE-based structure with a softmax classifier and trained by using the high-level features from the input network \mathcal{N}_I . Given a set of class maps $C = c_1, c_2, \dots, c_n$, the formulation of input network with softmax classifier is shown as:

$$\begin{cases} h_i^I = f(W_{I^I}x_i + b_{I^I}) \\ \hat{c}_i = f(W_{SMC}h_i^I), \end{cases} \quad (5.1)$$

where W_{SMC} is the weight matrix of softmax classifier. I use the predicted class map \hat{c}_i and the labeled class map c_i to calculate the loss function for obtaining the weight W_{SMC} . For the probability network, as mentioned in the previous section, the detection probability maps do not include classification information to influence the classification section. In order to improve this situation, I combine probability maps with corresponding class labels instead of original probability maps. Here I set $z_i = y_i \times c_i$ and the formulation of improved probability network \mathcal{N}_{PC} is as follows:

$$\begin{cases} h_i^{PC} = f(W_{I^{PC}}z_i + b_{I^{PC}}) \\ \hat{z}_i = f(W'_{I^{PC}}h_i^{PC} + b'_{I^{PC}}). \end{cases} \quad (5.2)$$

After above networks are obtained, I would like to rebuild the asymmetric connect network for integrating these networks. According to (4.3) and (5.2), I obtain the high-level feature representation h^I from input images and h^{PC} from the class-probability maps. Here I need to create another two different sub-networks to set the initial parameters of \mathcal{N}_{AC} . The first AE network is used to obtain the weight matrix W_{AC_1} and W'_{AC_1} and bias term b_{AC_1} by using h^I being input vectors for classification, while h^I and h^{PC} are used to train the second network to get the weight matrix W_{AC_2} and W'_{AC_2} and bias term b_{AC_2} . The second network is a simple end-to-end structure and derived from the connect network of the HDAE model. From the above two sub-networks, these pre-training parameters for detection and classification are integrated to initialize the proposed asymmetric connect network

\mathcal{N}_{AC} . Here I initialize weight matrix W_{AC_3} and bias terms b_{AC_3} of first hidden layer and weight matrix W'_{AC_3} of last hidden layer of \mathcal{N}_{AC} as:

$$W_{AC_3} = \begin{bmatrix} W_{AC_1} & 0 \\ 0 & W_{AC_2} \end{bmatrix}, W'_{AC_3} = \begin{bmatrix} W'_{AC_1} & 0 \\ 0 & W'_{AC_2} \end{bmatrix}, \quad (5.3)$$

$$b_{AC_3} = \begin{bmatrix} b_{AC_1} & b_{AC_2} \end{bmatrix}^T, \quad (5.4)$$

and pre-train the asymmetric connect network \mathcal{N}_{AC} to optimize these parameters:

$$\begin{cases} h_i^{AC_3-in} = f(W_{AC_3}h_i^I + b_{AC_3}) \\ h_i^{AC} = f(W_{AC}h_i^{AC_3-in} + b_{AC}) \\ h_i^{\hat{AC}} = f(W'_{AC}h_i^{AC} + b'_{AC}) \\ h_i^{AC_3-out} = f(W'_{AC_3}h_i^{\hat{AC}} + b'_{AC}), \end{cases} \quad (5.5)$$

where W_{AC} and b_{AC} are the rest of weight matrix and bias terms of the asymmetric connect network. $h_i^{AC_3-out}$ is the reconstructed feature representation of $h_i^{AC_3-in}$. The structures of the asymmetric connect network and class-probability network are shown in Fig. 5.5. Then the loss function is calculated between $h_i^{AC_3-out}$ and $\begin{bmatrix} h_i^I & h_i^{PC} \end{bmatrix}$ to optimize the parameters of \mathcal{N}_{AC} . The training of the Syn-AHDA algorithm is described below.

I use the above parameters I obtained from input network \mathcal{N}_I , class-probability network \mathcal{N}_{PC} , and asymmetric connect network \mathcal{N}_{AC} to construct the whole proposed network and then do the fine-tuning stage. The formulation of the loss function of proposed Syn-AHDA network is shown as:

$$Loss^{Syn-AHDA} = \sum_i \|z_i - \hat{z}_i\|^2 + \sum_i H(c_i, \hat{c}_i), \quad (5.6)$$

where $H(c_i, \hat{c}_i)$ is the cross-entropy cost function to estimate the classification loss

Algorithm 1 The training of Syn-AHDA network

Input: X : Input data; Y : Probability maps; C : Class labels; \mathcal{N}_I : an input AE network; \mathcal{N}_{PC} : a class-probability label AE network; \mathcal{N}_{class} : a classification network; \mathcal{N}_{AC} : an asymmetric connect network; W_{SMC} : a softmax weight vector; W_{AC_3} , b_{AC_3} and W'_{AC_3} : the weight and bias term of first hidden layer and the weight matrix of last hidden layer in \mathcal{N}_{AC} .

Output: The pre-trained Synchronized Hybrid Deep AE network: $\mathcal{N}_{Syn-AHDA}$;

- 1: Using input data X to train \mathcal{N}_I and extracting the encoding part of \mathcal{N}_I , $\mathcal{N}_{I_{encoding}}$;
 - 2: Using probability maps Y and the class labels C to train \mathcal{N}_{PC} and extracting the decoding part of \mathcal{N}_{PC} , $\mathcal{N}_{PC_{decoding}}$;
 - 3: Using input data X and class labels C in the network \mathcal{N}_{class} to obtain W_{SMC} ;
 - 4: Using sub-AE networks to construct the initial weight W_{AC_3} and bias b_{AC_3} terms in first hidden layer and the reconstructed weight W'_{AC_3} in the last layer of \mathcal{N}_{AC} ;
 - 5: Training \mathcal{N}_{AC} by using the output feature representation of $\mathcal{N}_{I_{encoding}}$ and integrated vector which combines the out feature representation of $\mathcal{N}_{I_{encoding}}$ and the input feature representation of $\mathcal{N}_{PC_{decoding}}$;
 - 6: Integrating $\mathcal{N}_{I_{encoding}}$, $\mathcal{N}_{PC_{decoding}}$, \mathcal{N}_{AC} and W_{SMC} into $\mathcal{N}_{Syn-AHDA}$ and then fine-tune this proposed network to optimize the parameters;
 - 7: **return** \mathcal{N}_{S-AHDA}
-

energy and defined by:

$$H(c_i, \hat{c}_i) = - [c_i \log(\hat{c}_i) - (1 - c_i) \log(1 - \hat{c}_i)]. \quad (5.7)$$

5.4.1 Neighboring Class Selector

After the processing of the proposed Syn-AHDA network, I obtain probability maps and class maps and need to look for the local maximum points as the centers of cells and the corresponding class for each of them. For detecting the position of cell centroids, same as the post-processing in HDAE network, a thresholding value, which is obtained and optimized by evaluating training images, is introduced to remove the elements with low probability values and to capture the local maximum point in the probability to be the predicted center of each cell. In addition, I also consider the neighboring elements of class map around each predicted center point to identify which class this center point belongs to. For each predicted center $x_c^{(i)}$, I define a set of class considering range as:

$$R(x_c^{(i)}) = \{x_c^{(i)} \in \wp_I : \|z(x_c^{(i)}) - z(x)\|_2 \leq d_\rho\}, \quad (5.8)$$

where x_c denotes the predicted centers of cells; d_ρ is the radius of class considering range. $z(x)$ represent the location of a point x ; \wp_I denotes the class response of image I . Predicted class of each detected center is given by:

$$C(x_c^{(i)}) = \underset{k}{argmax} \frac{\sum (R(x_c^{(i)}) = k)}{|R(x_c^{(i)})|}, \quad (5.9)$$

where k is the class label and $|R(x_c^{(i)})|$ denotes the number of elements within range. In other words, the class selector measures that which class has high probability value and assigns this class label to the detected center. This class selector is

necessary because the classification section could be affected by the detection section in the proposed network. For reducing the influence of detection section, I consider the neighboring region of class map around each detected point. For accurately identifying the position and class of center points, I need to strictly define the size of range in detection and classification sections. In our experiments, I set the radius = 12 pixels for detection and $d_\rho = 2$ pixels for classification so as to allow considering range to cover the major area of a nucleus to be detected and classified.

5.5 Experimental Results

5.5.1 Data collection

The experiment dataset is same as in Chapter 4, including a set of 52 $40\times$ magnification H&E stained histopathological images of 5 ET and 5 prefibrotic PMF cases collected from UHCW by using an Omyx VL120 scanner. The annotation of 11,623 nuclear patches in our image dataset consists of 6856 erythroid cells and 4,767 myeloid cells, which are marked by a junior trainee and verified by an experienced pathologist. I only consider two major types of bone marrow cells to measure the ability of the Syn-AHDA model in our experiments because unclear, complex, and heterogeneous cellular features cause the experts not to precisely give the identification of different types of BM cells. Moreover, I keep using 2-fold validation to prevent over-fitting problem and use them as training and testing image datasets in all experiments.

5.5.2 Network Setting and Training

Here the patch size is also set 29×29 pixels, which can efficiently capture a whole non-MK nucleus in $40\times$ magnification resolution. Each patch still includes four color channels (RGB and the Hematoxylin channel). For the input network \mathcal{N}_I in the proposed scheme, I set the input vector with size $(29^2 \times 4) \times 1$, which is same as

the one in HDAE network, and two hidden layers. The first and second hidden layers of input network have 1600 and 400 hidden units, respectively. I also introduce one softmax classifier with \mathcal{N}_I for initializing the classification section. Moreover, the probability label network \mathcal{N}_{PC} has $(29^2 \times 1)$ input units, which are generated by using curve-support Gaussian model and combining corresponding class labels, and one hidden layer with 400 hidden units. For constructing the asymmetric connect network \mathcal{N}_{AC} , I set the architecture to have 400 input units from the output of \mathcal{N}_I , 800 hidden units, and 800 output units corresponding to the high-level feature representations of \mathcal{N}_I and \mathcal{N}_{PC} . As I mentioned in Section 5.3, the number of neurons of \mathcal{N}_{AC} is conducted by integrating the number of neurons in high-level representation of pre-trained sub-networks of hybrid detection network and hybrid classification network. In order to optimize the parameters of the entire Syn-AHDA network, I use these parameters to pre-train the asymmetric connect network and then fine-tune the whole proposed network with dropout. In the post-processing, local maxima and a thresholding value are used to remove low probability responses and identify the centroid of all types of cells. Then I use neighboring class selector to consider the neighboring points surrounding a detected center to identify final class of this center.

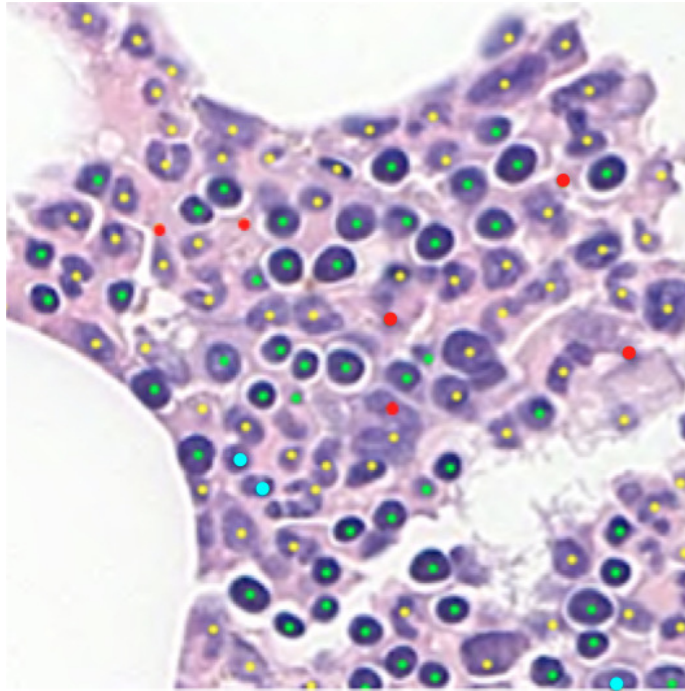
5.5.3 Evaluation and Comparison of Syn-AHDA network

Fig. 5.6 shows the examples of the results of the proposed Syn-AHDA network. It demonstrates that the Syn-AHDA network can efficiently detect and classify two different types of bone marrow hematopoietic stem cells. Here I define that a predicted point is true positive when the detection and classification outcomes of this point are as same as ground truth. However, there are a few incorrect detection or classification results. These incorrect outcomes in detection or classification occur because (1) the cell has faded stain color or the size of cell is larger than the size of the training patch; (2) the thresholding value is affected by class labels and

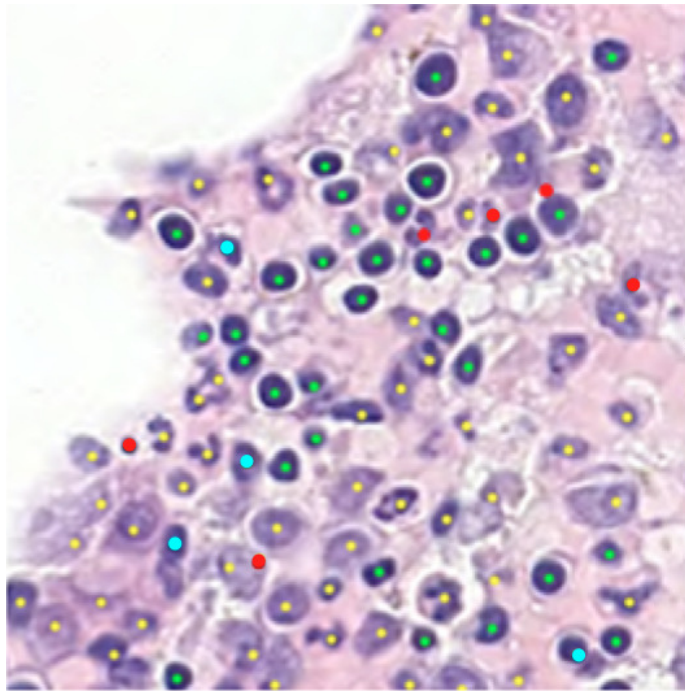
not efficient to remove the noise points in whole dataset or; (3) some myeloid cells have similar shape and intensity features to erythroid cells, and this affects that the proposed network is uncertain of these two types of cells in classification.

For evaluating the detection ability of Syn-HADA network, I compare the quantitative performance of the proposed network with other current conventional and DL approaches. At first, I need to confirm that the proposed Syn-AHDA network has similar ability of nuclei detection to other detection models, such as LIPSyM [191], SSAE [101] and SC-CNN [95], and our HDAE network, which the proposed method is derived from. Table 5.1 shows comparative results in terms of precision, recall and accuracy between the proposed model and other detection approaches. It shows that our proposed approach achieves similar performance to original HDAE network and has better performance than other state-of-the-art models for detection purpose. It also means the proposed network in detection section efficiently reduces the influence from the classification section in asymmetric structure and maintains the ability of detecting various nuclear shapes and precisely reflecting the locations of centroids of various cells.

In classification section, for fair comparison, I use the same method to detect the center points and different DL methods for classification. Here I adopt sparse AE, SSAE and CNN for comparing the classification performance with the proposed method. The number of hidden layers in SSAE network is set to 6, which is the same number of layers in the proposed method. CNN network includes 3 convolutional layers, 3 max-pooling layers, one fully connected layer and one softmax layer. Here I note that the predicted center points that match with the ground truth of detection are used in quantitative measurement of classification. Table 5.2 shows that our proposed network provides better performance than other DL frameworks. The proposed network also provides similar ability of classification to other DL approaches but has less performance than CNN in precision and than SSAE in recall. This situation exists in both detection and classification sections because,



(a)



(b)

Figure 5.6: Sample results of detection and classification via Syn-AHDA network. Green and yellow dots represent the erythroid and myeloid cells, respectively. Red dots denote the incorrect cases of detection and cyan dots are incorrect cases of classification.

Table 5.1: Comparison of results of detection between the proposed model and other methods

| Methods | Precision | Recall | F1-score |
|--------------|---------------|---------------|---------------|
| LIPSyM [191] | 0.7267 | 0.6514 | 0.687 |
| SSAE [101] | 0.8733 | 0.719 | 0.7887 |
| SC-CNN [95] | 0.9517 | 0.9118 | 0.9313 |
| HDAE [201] | 0.9273 | 0.9702 | 0.9483 |
| Syn-AHDA | 0.9129 | 0.9641 | 0.9378 |

Table 5.2: Comparison of classification results between the proposed model and other combined approaches

| Methods | Precision | Recall | F1-score |
|-----------|---------------|---------------|--------------|
| HDAE+SAE | 0.8267 | 0.8108 | 0.8187 |
| HDAE+SSAE | 0.8461 | 0.9037 | 0.874 |
| HDAE+CNN | 0.8605 | 0.8922 | 0.8761 |
| Syn-AHDA | 0.859 | 0.896 | 0.877 |

although I have designed several components in the proposed network for avoiding and reducing this loss energy influence, the detection and classification sections in proposed network are affected by each other, and that affects the accuracy of detection and classification. Moreover, this influence propagation between detection and classification sections makes the optimized parameters not to suit both the strategies but finds a balance point between them to maintain sufficient functionalities of detection and classification purposes as individual ones by using pre-training stage and reconstructing initial parameters of \mathcal{N}_{AC} . Overall, although the proposed Syn-AHDA network can obtain better performance of detection and classification than some conventional deep learning frameworks, there is room for improvement in our proposed network in future research. For instance, because the detection and classification sections affect each other, the high-level features of the detection or classification might be lost or occur some errors in training stage. I will use some low-level features and add them into high-level features to compensate those lost or error feature information for improving the performance of the Syn-AHDA network.

Table 5.3: Comparison of the training time between conventional frameworks and the proposed method

| Methods | Training Time |
|-----------|------------------|
| HDAE+SAE | 5-6 hours |
| HDAE+SSAE | 7-8 hours |
| HDAE+CNN | 6-7 hours |
| Syn-AHDA | 4-5 hours |

5.5.4 Computational Run Times

In addition, I compare the time of training among these frameworks of detection and classification. Table 5.3 shows our proposed network takes fewer time for training than other framework. It means the proposed network provides lower computational complexity and need to train less number of parameters than other conventional frameworks. It is because the Syn-AHDA network uses the parallel architecture to implement simultaneous detection and classification. Removing the redundant learning layers and using the asymmetric connect network are key roles in the proposed network to reduce the number of full connection layers that need to be trained.

5.6 Summary

In this chapter, I presented a novel synchronized hybrid deep AE network to perform nuclei detection and classification simultaneously. The proposed network consists of the HDAE network [201], an asymmetric connection network and a softmax classifier. The experimental results show that the proposed Syn-AHDA method provides better abilities of detection and classification than most of conventional DL frameworks and efficiently takes less training time than other approaches.

Chapter 6

Conclusions and Future Work

6.1 Conclusions

According to the WHO diagnosis criteria of distinguishing ET and prefibrotic PMF, it is difficult to differentiate the trephine histology images in these two subtypes of MPNs that suffer from low inter-observer agreement among the experienced pathologists. For more reproducible and reliable diagnostic analysis of ET and prefibrotic PMF, computer techniques and algorithms are introduced in this thesis to help pathologists realize current diagnostic features and discover potential clues to improve current diagnostic criteria of ET and prefibrotic PMF.

This thesis makes three main contributions, which produce robust image processing outcomes of segmentation, detection and classification on various types of cells in BM trephine images. This chapter summarizes the contributions of this thesis and proposes future work.

In chapter 3, I presented an automated framework that delineates MKs from non-homogeneous BM trephine images. The proposed framework considers Hematoxylin and Eosin stain channels to describe nuclear, cytoplasmic and background regions and then uses naïve Bayesian classifier with scattering transform to obtain MK cytoplasmic regions to identify potential MK nuclei. After that, a region-based

AC model and the proposed DCAC model are used to segment MK nuclear region and cytoplasmic region. The proposed DCAC model utilizes energy forces of both stain channels and circumscribing regions to automatically control the evolving contour to gradually converge to the desirable cytoplasmic boundary even in areas where weak edges exist. The proposed framework and DCAC model provide better performance of delineating MKs than other approaches in BM trephine biopsy images.

Chapter 4 proposes a novel hybrid deep autoencoder network for detecting all hematopoietic stem cells with irregular shapes in BM trephine images. The proposed network employs a curve-support Gaussian model to represent topographic features of irregular cell shapes. Then it uses three different networks to learn high-level features of the input image and these topographic features and connect them to generate probability response of center points. The proposed HDAE network provides better performance of detection than other state-of-the-art conventional and deep learning approaches.

Chapter 5 proposes a novel parallel deep learning approach that can simultaneously detect and classify hematopoietic stem cells in BM trephine images. The proposed network is derived from the HDAE network but is an asymmetric structure that makes the network has two functions at the same time. The asymmetric structure of the proposed network is developed from an asymmetric connect component to integrate input, detection and classification networks. Due to the key asymmetric connect component, the proposed Syn-AHDA network can learn high-level features from input images and use these features to simultaneously generate probability maps of detection and class maps of classification. The proposed Syn-AHDA network maintains as good abilities of detection and classification as other conventional deep learning frameworks and takes less training time than others.

According to Section 1.4, the above three main research objectives are accomplished. The framework with DCAC model can efficiently delineate the nuclei

and cytoplasm regions of MKs with weak boundary features. HDAE network can easily identify the center of irregular-shape BM cells because curve-support Gaussian model can efficiently reconstruct approximate Gaussian shape for each BM cell. Syn-AHDA network can simultaneously work on BM cell detection and classification by using an asymmetric connect component. However, these proposed methods have some limitations. For instance, if the size of MK nucleus is as small as the size of non-MK nucleus, the framework might miss this MK. Moreover, if the size of BM cell is much larger than the size of sliding window, HDAE network might find more than one center point in a large cell. In addition, as I mentioned in Chapter 5, the intra-influence between two different functions still exists in Syn-AHDA network because of backpropagation, and it makes the performance become worse. Otherwise, according to research objectives, integrating these three proposed methods into a whole framework is not accomplished yet. This unaccomplished research objective and these drawbacks of proposed methods will be implemented and improved in the future research.

6.2 Future Directions

For helping hematopathologists efficiently identify ET and prefibrotic PMF, algorithms proposed in this thesis can be used to build a CAD system for further investigation and analysis. More works need to be done in order to obtain more robust and accurate outcomes for diagnosis improvement. There are several future research direction listed as follows:

- One can modify the DCAC model with repulsive shape prior information to avoid overlapping or touching problems.
- The Syn-ADAC network can be modified by weighting probability and class maps and using other approaches to improve the accuracy of nuclei detection

and classification. Then it can be extended to do multi-classes identification via the Syn-ADAC network to look for potential cytological and geographic features for further investigation.

- The framework of delineating MKs can be combined with Syn-ADAC network to form an automated integrated system for extracting diagnostic features from all types of BM cells.
- Finally, quantitative analysis is the key for investigating and identifying specific features of diseases to help pathologists make precise diagnosis. An integrated CAD system will take into account BM trephine whole slide biopsies and quantify cellular and texture characteristics to assist pathologists to analyze and find potential clues for improving the current WHO criteria of distinguishing ET and prefibrotic PMF in further investigation. Extensive validation of techniques developed in this thesis is required before they can be deployed in a clinical setting.

Bibliography

- [1] J. W. Vardiman *et al.*, “The 2008 revision of the world health organization (WHO) classification of myeloid neoplasms and acute leukemia: rationale and important changes,” *Blood*, vol. 114, no. 5, pp. 937–951, 2009.
- [2] “Bone marrow biopsy,” 2015, Cancer Research UK. [Online]. Available: <http://www.cancerresearchuk.org/about-cancer/bone-cancer/>
- [3] “Bone marrow biopsy article,” 2017, EMedicinehealth.com. [Online]. Available: https://www.emedicinehealth.com/bone_marrow_biopsy/article_em.htm
- [4] M. Helfrich, “Bone marrow aspiration: Normal hematopoiesis and basic interpretive procedures,” 2017, MediaLab Incorporated. [Online]. Available: https://www.medialabinc.net/bone_marrow_aspiration_hematopoiesis.aspx
- [5] J. Blair, “Various normal marrow cells are shown;,” 2016, Slideplayer.com. [Online]. Available: <http://slideplayer.com/slide/11018533/>
- [6] B. J. Bain, D. M. Clark, I. A. Lampert, and B. S. Wilkins, *Bone marrow pathology*, 4th ed. West Sussex, UK: Blackwell Science Ltd., 2010.
- [7] “Funny medical cliparts,” 2016, cliparts Library. [Online]. Available: <http://clipart-library.com/clipart/1808527.htm>

- [8] “Equipment: Aperio scanscope slide scanner,” 2017, beecher Instruments, Lifespan. [Online]. Available: <https://www.lifespan.org/centers-services/cobre-center-cancer-research-development-rhode-island-hospital/molecular-0>
- [9] “Database png transparent images,” 2016, cliparts Library. [Online]. Available: clipart-library.com/clipart/Database-PNG-Clipart.htm
- [10] “Database and sql,” 2017, the Tech Academy. [Online]. Available: <https://www.learncodinganywhere.com/CourseOverViews/databaseSql>
- [11] A. Chekkoury, “Automatic malignancy detection in breast histopathology images,” 2012. [Online]. Available: <http://campar.in.tum.de/Main/AndreiChekkoury>
- [12] A. V. Hoffbrand, P. A. H. Moss, and J. E. Pettit, “Essential haematology 2006,” *Blackwell Publishing, Malden MA, pgs*, vol. 5, p. 249, 2006.
- [13] B. S. Wilkins *et al.*, “Bone marrow pathology in essential thrombocythemia: interobserver reliability and utility for identifying disease subtypes,” *Blood*, vol. 111, no. 1, pp. 60–70, 2008.
- [14] T. F. Chan and L. A. Vese, “Active contours without edges,” *IEEE Transaction on Image Processing*, vol. 10, no. 2, pp. 266–277, 2001.
- [15] R. Wu, “Chan-vese active contours,” 2014. [Online]. Available: <https://sites.google.com/site/rexstribefimageprocessing/chan-vese-active-contours>
- [16] “What is cancer?” 2015, National Cancer Institute. [Online]. Available: <https://www.cancer.gov/about-cancer/understanding/what-is-cancer>
- [17] A. Tefferi, “Myeloproliferative neoplasms,” 2015. [Online]. Available: <https://clinicalgate.com/myeloproliferative-neoplasms-2/>

- [18] A. A. Fauser and H. A. Messner, "Identification of megakaryocytes, macrophages, and eosinophils in colonies of human bone marrow containing neutrophilic granulocytes and erythroblasts," *Blood*, vol. 53, no. 5, pp. 1023–1027, 1979.
- [19] G. J. Titmarsh, A. S. Duncombe, M. F. McMullin, M. O'Rorke, R. Mesa, F. D. Vocht, S. Horan, L. Fritschi, M. Clarke, and L. A. Anderson, "How common are myeloproliferative neoplasms? a systematic review and meta-analysis," *American Journal of Hematology*, vol. 89, no. 6, pp. 581–587, 2014.
- [20] T. Barbui *et al.*, "Problems and pitfalls regarding who-defined diagnosis of early/prefibrotic primary myelofibrosis versus essential thrombocythemia," *Leukemia*, vol. 27, no. 10, pp. 1953–1958, 2013.
- [21] J. Thiele *et al.*, "Early stage idiopathic (primary) myelofibrosis - current issues of diagnostic features," *Leukemia & Lymphoma*, vol. 43, no. 5, pp. 1035–1041, 2002.
- [22] A. Tefferi, "Myeloproliferative neoplasms 2012: the John M. Bennett 80th birthday anniversary lecture," *Leukemia Research*, vol. 36, no. 12, pp. 1481–1489, 2012.
- [23] A. Tefferi and J. W. Vardiman, "Classification and diagnosis of myeloproliferative neoplasms: the 2008 world health organization criteria and point-of-care diagnostic algorithms," *Leukemia*, vol. 22, no. 1, pp. 14–22, 2008.
- [24] A. Tefferi, "Novel mutations and their functional and clinical relevance in myeloproliferative neoplasms: Jak2, mpl, tet2, asxl1, cbl, idh and ikzf1," *Leukemia*, vol. 24, no. 6, pp. 1128–1138, 2010.
- [25] J. Thiele, "Philadelphia chromosome–negative chronic myeloproliferative disease," *American Journal of Clinical Pathology*, vol. 132, no. 2, pp. 261–280, 2009.

- [26] A. Tefferi, “Molecular drug targets in myeloproliferative neoplasms: mutant *abl1*, *jak2*, *mpl*, *kit*, *pdgfra*, *pdgfrb* and *fgfr1*,” *Journal of Cellular and Molecular Medicine*, vol. 13, no. 2, pp. 215–237, 2009.
- [27] S. A. Wang, R. P. Hasserjian, P. S. Fox, H. J. Rogers, J. T. Geyer, D. Chabot-Richards, E. Weinzierl, J. Hatem, J. Jaso, R. Kanagal-Shamanna *et al.*, “Atypical chronic myeloid leukemia is clinically distinct from unclassifiable myelodysplastic/myeloproliferative neoplasms,” *Blood*, vol. 123, no. 17, pp. 2645–2651, 2014.
- [28] M. G. Rojo, “State of the art and trends for digital pathology,” *Studies in Health Technology and Informatics*, vol. 179, pp. 15–28, 2012.
- [29] H. Irshad *et al.*, “Methods for nuclei detection, segmentation and classification in digital histopathology: A review. current status and future potential,” *IEEE Review in Biomedical Engineering*, vol. 7, pp. 97–114, December 2014.
- [30] J. Thiele, H. M. Kvasnicka, J. W. Vardiman, A. Orazi, V. Franco, H. Gisslinger, G. Birgegard, M. Griesshammer, and A. Tefferi, “Bone marrow fibrosis and diagnosis of essential thrombocythemia,” *Journal of Clinical Oncology*, vol. 27, no. 34, pp. e220–e221, 2009.
- [31] H. M. Kvasnicka and J. Thiele, “Prodromal myeloproliferative neoplasms: the 2008 who classification,” *American Journal of Hematology*, vol. 85, no. 1, pp. 62–69, 2010.
- [32] T. Barbui, J. Thiele, F. Passamonti, E. Rumi, E. Boveri, M. L. Randi, I. Bertozzi, F. Marino, A. M. Vannucchi, L. Pieri *et al.*, “Initial bone marrow reticulin fibrosis in polycythemia vera exerts an impact on clinical outcome,” *Blood*, vol. 119, no. 10, pp. 2239–2241, 2012.
- [33] T. Barbui, J. Thiele, F. Passamonti, E. Rumi, E. Boveri, M. Ruggeri, F. Rodeghiero, E. S. d’Amore, M. L. Randi, I. Bertozzi *et al.*, “Survival and

disease progression in essential thrombocythemia are significantly influenced by accurate morphologic diagnosis: an international study,” *Journal of Clinical Oncology*, vol. 29, no. 23, pp. 3179–3184, 2011.

- [34] C. Lopez, M. Lejeune, R. Bosch, A. Korzynska, M. Garcia-Rojo, M.-T. Salvado, T. Alvaro, C. Callau, A. Roso, and J. Jaen, “Digital image analysis in breast cancer: an example of an automated methodology and the effects of image compression.” *Studies in Health Technology and Informatics*, vol. 179, pp. 155–171, 2011.
- [35] D. J. Foran, L. Yang, W. Chen, J. Hu, L. A. Goodell, M. Reiss, F. Wang, T. Kurc, T. Pan, A. Sharma *et al.*, “Imageminer: a software system for comparative analysis of tissue microarrays using content-based image retrieval, high-performance computing, and grid technology,” *Journal of the American Medical Informatics Association*, vol. 18, no. 4, pp. 403–415, 2011.
- [36] M. G. Rojo, V. Punys, J. Slodkowska, T. Schrader, C. Daniel, and B. Blobel, “Digital pathology in Europe: coordinating patient care and research efforts,” *Studies in Health Technology and Informatics*, vol. 150, pp. 997–1001, January 2009.
- [37] M. N. Gurcan *et al.*, “Histopathological image analysis: A review,” *IEEE Reviews in Biomedical Engineering*, vol. 2, pp. 147–171, October 2009.
- [38] A. Madabhushi, “Digital pathology image analysis: opportunities and challenges,” *Imaging In Medicine*, vol. 1, no. 1, pp. 7–10, 2009.
- [39] E. Reinhard, M. Adhikhmin, B. Gooch, and P. Shirley, “Color transfer between images,” *IEEE Computer Graphics and Applications*, vol. 21, no. 5, pp. 34–41, 2001.
- [40] D. Magee, D. Treanor, D. Crellin, M. Shires, K. Smith, K. Mohee, and P. Quirke, “Colour normalisation in digital histopathology images,” in *Proc*

Optical Tissue Image analysis in Microscopy, Histopathology and Endoscopy (MICCAI Workshop), vol. 100. Daniel Elson, 2009.

- [41] M. Macenko, M. Niethammer, J. Marron, D. Borland, J. T. Woosley, X. Guan, C. Schmitt, and N. E. Thomas, “A method for normalizing histology slides for quantitative analysis,” in *Biomedical Imaging: From Nano to Macro, 2009. ISBI’09. IEEE International Symposium on*. IEEE, 2009, pp. 1107–1110.
- [42] A. M. Khan, N. M. Rajpoot, D. Treanor, and D. Magee, “A non-linear mapping approach to stain normalization in digital histopathology images using image-specific colour deconvolution,” *IEEE Transactions on Biomedical Engineering*, vol. 61, pp. 1729–1738, 2014.
- [43] J. Cheng, J. C. Rajapakse *et al.*, “Segmentation of clustered nuclei with shape markers and marking function,” *IEEE Transactions on Biomedical Engineering*, vol. 56, no. 3, pp. 741–748, 2009.
- [44] F. Cloppet and A. Boucher, “Segmentation of overlapping/aggregating nuclei cells in biological images,” in *Pattern Recognition, 2008. ICPR 2008. 19th International Conference on*. IEEE, 2008, pp. 1–4.
- [45] R. C. Gonzalez and R. E. Woods, *Digital image processing*, Upper Saddle River, NJ, USA, 2008.
- [46] J. MacQueen *et al.*, “Some methods for classification and analysis of multivariate observations,” in *Proceedings of the fifth Berkeley Symposium on Mathematical Statistics and Probability*, vol. 1, no. 14, 1967, pp. 281–297.
- [47] C. M. Bishop, “Pattern recognition,” *Machine Learning*, vol. 128, pp. 1–58, 2006.
- [48] E. Meijering, “Cell segmentation: 50 years down the road,” *IEEE Signal Processing Magazine*, vol. 29, no. 5, pp. 140–145, 2012.

- [49] X. Yang, H. Li, and X. Zhou, “Nuclei segmentation using marker-controlled watershed, tracking using mean-shift, and kalman filter in time-lapse microscopy,” *IEEE Transactions on Circuits and Systems I: Regular Papers*, vol. 53, no. 11, pp. 2405–2414, 2006.
- [50] C. Wählby, I.-M. Sintorn, F. Erlandsson, G. Borgefors, and E. Bengtsson, “Combining intensity, edge and shape information for 2d and 3d segmentation of cell nuclei in tissue sections,” *Journal of Microscopy*, vol. 215, no. 1, pp. 67–76, 2004.
- [51] C. Jung and C. Kim, “Segmenting clustered nuclei using h-minima transform-based marker extraction and contour parameterization,” *IEEE Transactions on Biomedical Engineering*, vol. 57, no. 10, pp. 2600–2604, 2010.
- [52] J. Friedman, T. Hastie, and R. Tibshirani, *The elements of statistical learning*. Springer, NY, USA, 2011, vol. 2.
- [53] M. Arif and N. Rajpoot, “Classification of potential nuclei in prostate histology images using shape manifold learning,” in *Machine Vision, 2007. ICMV 2007. International Conference on*, 2007, pp. 113–118.
- [54] A. P. Dempster, N. M. Laird, and D. B. Rubin, “Maximum likelihood from incomplete data via the em algorithm,” *Journal of the Royal Statistical Society. Series B (methodological)*, pp. 1–38, 1977.
- [55] C. Jung, C. Kim, S. W. Chae, and S. Oh, “Unsupervised segmentation of overlapped nuclei using bayesian classification,” *IEEE Transactions on Biomedical Engineering*, vol. 57, no. 12, pp. 2825–2832, 2010.
- [56] T. Janssens, L. Antanas, S. Derde, I. Vanhorebeek, G. V. den Berghe, and F. G. Grandas, “Charisma: An integrated approach to automatic h&e-stained skeletal muscle cell segmentation using supervised learning and novel robust clump splitting,” *Medical Image Analysis*, vol. 17, no. 8, pp. 1206–1219, 2013.

- [57] J.-R. Dalle, H. Li, C.-H. Huang, W. K. Leow, D. Racoceanu, and T. C. Putti, “Nuclear pleomorphism scoring by selective cell nuclei detection.” in *WACV*, 2009.
- [58] E. Cosatto *et al.*, “Grading nuclear pleomorphism on histological micrographs,” in *Pattern Recognition, 2008. ICPR 2008. 19th International Conference on*, 2008, pp. 1–4.
- [59] G. Cong and B. Parvin, “Model-based segmentation of nuclei,” *Pattern Recognition*, vol. 33, no. 8, pp. 1383–1393, 2000.
- [60] S. Kumar, S. H. Ong, S. Ranganath, T. C. Ong, and F. T. Chew, “A rule-based approach for robust clump splitting,” *Pattern Recognition*, vol. 39, no. 6, pp. 1088–1098, 2006.
- [61] S. Nasr-Isfahani, A. Mirsafian, and A. Masoudi-Nejad, “A new approach for touching cells segmentation,” in *BioMedical Engineering and Informatics, 2008. BMEI 2008. International Conference on*, vol. 1. IEEE, 2008, pp. 816–820.
- [62] O. Lezoray and H. Cardot, “Cooperation of color pixel classification schemes and color watershed: a study for microscopic images,” *IEEE Transactions on Image Processing*, vol. 11, no. 7, pp. 783–789, 2002.
- [63] M. Veta, A. Huisman, M. A. Viergever, P. J. van Diest, and J. P. Pluim, “Marker-controlled watershed segmentation of nuclei in h&e stained breast cancer biopsy images,” in *Biomedical Imaging: From Nano to Macro, 2011 IEEE International Symposium on*, 2011, pp. 618–621.
- [64] Y. Song, L. Zhang, S. Chen, D. Ni, B. Lei, and T. Wang, “Accurate segmentation of cervical cytoplasm and nuclei based on multiscale convolutional network and graph partitioning,” *IEEE Transactions on Biomedical Engineering*, vol. 62, no. 10, pp. 2421–2433, 2015.

- [65] H. Fatakdawala *et al.*, “Expectation maximization driven geodesic active contour with overlap resolution (emagacor): Application to lymphocyte segmentation on breast cancer histopathology,” *IEEE Transection on Biomedical Engineering*, vol. 57, no. 7, pp. 1676–1689, 2010.
- [66] H. Masmoudi, S. M. Hewitt, N. Petrick, K. J. Myers, and M. A. Gavrielides, “Automated quantitative assessment of her-2/neu immunohistochemical expression in breast cancer,” *IEEE Transactions on Medical Imaging*, vol. 28, no. 6, pp. 916–925, 2009.
- [67] M. S. Kulikova, A. Veillard, L. Roux, and D. Racoceanu, “Nuclei extraction from histopathological images using a marked point process approach.” in *Medical Imaging: Image Processing*, 2012, p. 831428.
- [68] C. Jung, C. Kim, S. W. Chae, and S. Oh, “Unsupervised segmentation of overlapped nuclei using bayesian classification,” *IEEE Transactions on Biomedical Engineering*, vol. 57, no. 12, pp. 2825–2832, 2010.
- [69] O. Ronneberger, P. Fischer, and T. Brox, “U-net: Convolutional networks for biomedical image segmentation,” in *International Conference on Medical Image Computing and Computer-Assisted Intervention*. Springer, 2015, pp. 234–241.
- [70] Y. Song, L. Zhang, S. Chen, D. Ni, B. Lei, and T. Wang, “Accurate segmentation of cervical cytoplasm and nuclei based on multiscale convolutional network and graph partitioning,” *IEEE Transactions on Biomedical Engineering*, vol. 62, no. 10, pp. 2421–2433, 2015.
- [71] P. Soille, *Morphological image analysis: principles and applications*. Springer Science & Business Media, 2013.
- [72] X. Yang, H. Li, and X. Zhou, “Nuclei segmentation using marker-controlled watershed, tracking using mean-shift, and kalman filter in time-lapse mi-

croscopy,” *IEEE Transactions on Circuits and Systems I: Regular Papers*, vol. 53, no. 11, pp. 2405–2414, 2006.

- [73] C. R. Maurer, R. Qi, and V. Raghavan, “A linear time algorithm for computing exact euclidean distance transforms of binary images in arbitrary dimensions,” *IEEE Transactions on Pattern Analysis and Machine Intelligence*, vol. 25, no. 2, pp. 265–270, 2003.
- [74] U. Adiga, R. Malladi, R. Fernandez-Gonzalez, and C. O. de Solorzano, “High-throughput analysis of multispectral images of breast cancer tissue,” *IEEE Transactions on Image Processing*, vol. 15, no. 8, pp. 2259–2268, 2006.
- [75] J. Matas, O. Chum, M. Urban, and T. Pajdla, “Robust wide-baseline stereo from maximally stable extremal regions,” *Image and Vision Computing*, vol. 22, no. 10, pp. 761–767, 2004.
- [76] Z. Lu, G. Carneiro, and A. P. Bradley, “Automated nucleus and cytoplasm segmentation of overlapping cervical cells,” in *International Conference on Medical Image Computing and Computer-Assisted Intervention*, 2013, pp. 452–460.
- [77] J. Matas, O. Chum, M. Urban, and T. Pajdla, “Robust wide-baseline stereo from maximally stable extremal regions,” *Image and Vision Computing*, vol. 22, no. 10, pp. 761–767, 2004.
- [78] C. Arteta, V. Lempitsky, J. A. Noble, and A. Zisserman, “Learning to detect cells using non-overlapping extremal regions,” in *International Conference on Medical Image Computing and Computer-Assisted Intervention*. Springer, 2012, pp. 348–356.
- [79] J. Byun, M. R. Verardo, B. Sumengen, G. P. Lewis, B. Manjunath, and S. K. Fisher, “Automated tool for the detection of cell nuclei in digital microscopic images: application to retinal images,” *Molecular Vision*, vol. 12, no. 105-07, pp. 949–60, 2006.

- [80] T. Lindeberg, “Feature detection with automatic scale selection,” *International Journal of Computer Vision*, vol. 30, no. 2, pp. 79–116, 1998.
- [81] H. Peng, X. Zhou, F. Li, X. Xia, and S. T. Wong, “Integrating multi-scale blob/curvilinear detector techniques and multi-level sets for automated segmentation of stem cell images,” in *Biomedical Imaging: From Nano to Macro, 2009. ISBI’09. IEEE International Symposium on*, 2009, pp. 1362–1365.
- [82] F. Li, X. Zhou, H. Zhao, and S. T. Wong, “Cell segmentation using front vector flow guided active contours,” in *International Conference on Medical Image Computing and Computer-Assisted Intervention*, 2009, pp. 609–616.
- [83] Y. Al-Kofahi, W. Lassoued, W. Lee, and B. Roysam, “Improved automatic detection and segmentation of cell nuclei in histopathology images,” *IEEE Transactions on Biomedical Engineering*, vol. 57, no. 4, pp. 841–852, 2010.
- [84] B. Parvin, Q. Yang, J. Han, H. Chang, B. Rydberg, and M. H. Barcellos-Hoff, “Iterative voting for inference of structural saliency and characterization of subcellular events,” *IEEE Transactions on Image Processing*, vol. 16, no. 3, pp. 615–623, 2007.
- [85] J. Byun, M. R. Verardo, B. Sumengen, G. P. Lewis, B. S. Manjunath, and S. K. Fisher, “Automated tool for the detection of cell nuclei in digital microscopic images: application to retinal images,” *Molecular Vision*, vol. 12, no. 105-07, pp. 949–60, 2006.
- [86] P. V. Hough, “Method and means for recognizing complex patterns,” Tech. Rep., 1962.
- [87] R. O. Duda and P. E. Hart, “Use of the hough transformation to detect lines and curves in pictures,” *Communications of the ACM*, vol. 15, no. 1, pp. 11–15, 1972.

- [88] D. Reisfeld, H. Wolfson, and Y. Yeshurun, “Context-free attentional operators: The generalized symmetry transform,” *International Journal of Computer Vision*, vol. 14, no. 2, pp. 119–130, 1995.
- [89] D. Reisfeld and Y. Yeshurun, “Preprocessing of face images: Detection of features and pose normalization,” *Computer Vision and Image Understanding*, vol. 71, no. 3, pp. 413–430, 1998.
- [90] E. Cosatto, M. Miller, H. P. Graf, and J. S. Meyer, “Grading nuclear pleomorphism on histological micrographs,” in *Pattern Recognition, 2008. ICPR 2008. 19th International Conference on*. IEEE, 2008, pp. 1–4.
- [91] G. Loy and A. Zelinsky, “Fast radial symmetry for detecting points of interest,” *IEEE Transactions on Pattern Analysis and Machine Intelligence*, vol. 25, no. 8, pp. 959–973, 2003.
- [92] X. Qi, F. Xing, D. J. Foran, and L. Yang, “Robust segmentation of overlapping cells in histopathology specimens using parallel seed detection and repulsive level set,” *IEEE Transactions on Biomedical Engineering*, vol. 59, no. 3, pp. 754–765, September 2012.
- [93] D. C. Cireşan, A. Giusti, L. M. Gambardella, and J. Schmidhuber, “Mitosis detection in breast cancer histology images with deep neural networks,” in *International Conference on Medical Image Computing and Computer-assisted Intervention*, 2013, pp. 411–418.
- [94] Y. Xie, F. Xing, X. Kong, H. Su, and L. Yang, “Beyond classification: structured regression for robust cell detection using convolutional neural network,” in *International Conference on Medical Image Computing and Computer-Assisted Intervention*, 2015, pp. 358–365.
- [95] K. Sirinukunwattana, S. Raza, Y.-W. Tsang, D. Snead, I. Cree, and N. Rajpoot, “Locality sensitive deep learning for detection and classification of nu-

- clei in routine colon cancer histology images,” *IEEE Transactions on Medical Imaging*, vol. 35, no. 5, pp. 1196–1206, 2016.
- [96] B. Ballarò, A. M. Florena, V. Franco, D. Tegolo, C. Tripodo, and C. Valenti, “An automated image analysis methodology for classifying megakaryocytes in chronic myeloproliferative disorders,” *Medical Image Analysis*, vol. 12, pp. 703–712, 2008.
- [97] P.-W. Huang and Y.-H. Lai, “Effective segmentation and classification for hcc biopsy images,” *Pattern Recognition*, vol. 43, no. 4, pp. 1550–1563, 2010.
- [98] J. P. Vink, M. B. V. Leeuwen, C. H. M. V. Deurzen, and G. D. Haan, “Efficient nucleus detector in histopathology images,” *Journal of Microscopy*, vol. 249, no. 2, pp. 124–135, 2013.
- [99] C. D. Malon and E. Cosatto, “Classification of mitotic figures with convolutional neural networks and seeded blob features,” *Journal of Pathology Informatics*, vol. 4, no. 1, p. 9, 2013.
- [100] X. Zhou, F. Li, J. Yan, and S. T. Wong, “A novel cell segmentation method and cell phase identification using markov model,” *IEEE Transactions on Information Technology in Biomedicine*, vol. 13, no. 2, pp. 152–157, 2009.
- [101] J. Xu, L. Xiang *et al.*, “Stacked sparse autoencoder (ssae) for nuclei detection on breast cancer histopathology images,” *IEEE Transactions on Medical Imaging*, vol. 35, no. 1, pp. 119–130, January 2016.
- [102] P. Baldi, “Autoencoders, unsupervised learning, and deep architectures,” *ICML unsupervised and transfer learning*, vol. 27, no. 37–50, p. 1, 2012.
- [103] J. Schmidhuber, “Deep learning in neural networks: An overview,” *Neural Networks*, vol. 61, pp. 85–117, January 2015.

- [104] A. A. Cruz-Roa, J. E. A. Ovalle, A. Madabhushi, and F. A. G. Osorio, “A deep learning architecture for image representation, visual interpretability and automated basal-cell carcinoma cancer detection,” in *International Conference on Medical Image Computing and Computer-Assisted Intervention (MICCAI)*, vol. 8150. Nagoya, Japan: Springer, 2013, pp. 403–410.
- [105] A. Mouelhi *et al.*, “Automatic segmentation of clustered breast cancer cells using watershed and concave vertex graph,” in *Communications, Computing and Control Applications (CCCA), 2011 International Conference on*, 2011, pp. 1–6.
- [106] A. Veillard *et al.*, “Cell nuclei extraction from breast cancer histopathology images using color, texture, scale and shape information,” *Diagnostic Pathology*, vol. 8, no. 1, pp. 1–3, 2013.
- [107] J. P. Vink *et al.*, “Efficient nucleus detector in histopathology images,” *Journal of Microscopy*, vol. 249, no. 2, pp. 124–135, 2013.
- [108] F. Bunyak *et al.*, “Histopathology tissue segmentation by combining fuzzy clustering with multiphase vector level sets,” in *Software tools and algorithms for biological systems*, 2011, pp. 413–424.
- [109] X. Qi *et al.*, “GPU enabled parallel touching cell segmentation using mean shift based seed detection and repulsive level set,” in *Medical Image Computing, Computer Assisted Intervention*, 2010, pp. 30–40.
- [110] A. Hafiane *et al.*, “Clustering initiated multiphase active contours and robust separation of nuclei groups for tissue segmentation,” in *Pattern Recognition, 2008. ICPR 2008. 19th International Conference on*, 2008, pp. 1–4.
- [111] J. Xu *et al.*, “Markov random field driven region-based active contour model (MaRACel): application to medical image segmentation,” in *International*

Conference on Medical Image Computing and Computer-Assisted Intervention, 2010, pp. 197–204.

- [112] R. Delgado-Gonzalo, V. Uhlmann, D. Schmitter, and M. Unser, “Snakes on a plane: A perfect snap for bioimage analysis.” *Signal Processing Magazine, IEEE* 32, vol. 1, pp. 41–48, 2015.
- [113] M. Kass, A. Witkin, and D. Terzopoulos, “Snakes: Active contour models,” *International Journal of Computer Vision*, vol. 1, no. 4, pp. 321–331, 1988.
- [114] K. Li, E. D. Miller, M. Chen, T. Kanade, L. E. Weiss, and P. G. Campbell, “Cell population tracking and lineage construction with spatiotemporal context,” *Medical Image Analysis*, vol. 12, no. 5, pp. 546–566, 2008.
- [115] D. Cremers, M. Rousson, and R. Deriche, “A review of statistical approaches to level set segmentation: integrating color, texture, motion and shape,” *International Journal of Computer Vision*, vol. 72, no. 2, pp. 195–215, 2007.
- [116] F. Xing, H. Su, and L. Yang, “An integrated framework for automatic ki-67 scoring in pancreatic neuroendocrine tumor,” in *International Conference on Medical Image Computing and Computer-Assisted Intervention*, 2013, pp. 436–443.
- [117] F. Xing, H. Su, J. Neltner, and L. Yang, “Automatic ki-67 counting using robust cell detection and online dictionary learning,” *IEEE Transactions on Biomedical Engineering*, vol. 61, no. 3, pp. 859–870, 2014.
- [118] L. A. Vese and T. F. Chan, “A multiphase level set framework for image segmentation using the mumford and shah model,” *International Journal of Computer Vision*, vol. 50, no. 3, pp. 271–293, 2002.

- [119] A. Tsai *et al.*, “Curve evolution implementation of the mumford-shah functional for image segmentation, denoising, interpolation, and magnification,” *IEEE Transection on Image Processing*, vol. 10, no. 8, pp. 1169–1186, 2001.
- [120] N. Paragios and R. Deriche, “Geodesic active regions and level set methods for supervised texture segmentation,” *International Journal of Computer Vision*, vol. 46, no. 3, pp. 223–247, 2002.
- [121] S. Gao and T. D. Bui, “Image segmentation and selective smoothing by using mumford-shah model,” *IEEE Transection on Image Processing*, vol. 14, no. 10, pp. 1537–1549, 2005.
- [122] J. E. Solem *et al.*, “Initialization techniques for segmentation with the chan-vese model,” in *Pattern Recognition, 2006. ICPR 2006. 18th International Conference on*, vol. 2, 2006, pp. 171–174.
- [123] R. Xia *et al.*, “An optimal initialization technique for improving the segmentation performance of chan-vese model,” in *Automation and Logistics, 2007 IEEE International Conference on*, 2007, pp. 411–415.
- [124] Y. Shi and W. C. Karl, “A fast level set method without solving PDEs,” in *Acoustics, Speech, and Signal Processing, 2005. Proceedings.(ICASSP’05). IEEE International Conference on*, vol. 2, 2005, pp. 97–100.
- [125] Y. Pan *et al.*, “Efficient implementation of the chan-vese models without solving PDEs,” in *Multimedia Signal Processing, 2006 IEEE 8th Workshop on*, 2006, pp. 350–354.
- [126] C. Li *et al.*, “Level set formulation without re-initialization: a new variational formulation,” in *CVPR 2005. IEEE Computer Society Conference on*, vol. 1, 2005, pp. 430–436.

- [127] L. Pi *et al.*, “A variational formulation for segmenting desired objects in color images,” *Image and Vision Computing*, vol. 25, no. 9, pp. 1414–1421, 2007.
- [128] C. Li *et al.*, “Implicit active contours driven by local binary fitting energy,” in *CVPR 2007. IEEE Conference on*, 2007, pp. 1–7.
- [129] X. F. Wang *et al.*, “An efficient local chan-veese model for image segmentation,” *Pattern Recognition*, vol. 43, no. 3, pp. 603–618, 2010.
- [130] Y. Zhou, W.-R. Shi, W. Chen, Y. lin Chen, Y. Li, L.-W. Tan, and D.-Q. Chen, “Active contours driven by localizing region and edge-based intensity fitting energy with application to segmentation of the left ventricle in cardiac ct image,” *Neurocomputing*, vol. 156, pp. 199–210, 2015.
- [131] Z. Ji, Y. Xia, Q. Sun, G. Cao, and Q. Chen, “Active contour driven by local likelihood image fitting energy for image segmentation,” *Information Science*, vol. 301, pp. 285–304, 2015.
- [132] M. Shen and Y. Wu, “A new improved local chan-veese model,” in *Proc. SPIE, Sixth ICGIP 2014*, vol. 9443, 2015.
- [133] E. S. Brown *et al.*, “Completely convex formulation of the chan-veese image segmentation model,” *International Journal of Computer Vision*, vol. 98, no. 1, pp. 103–121, 2012.
- [134] G. Liu, Z. Zhou, H. Zhong, and S. Xie, “Gradient descent with adaptive momentum for active contour models,” *IET Computer Vision*, vol. 8, no. 4, pp. 287–298, 2014.
- [135] J. Spencer and K. Chen, “Stabilised bias field: segmentation with intensity inhomogeneity,” *Journal of Algorithms & Computational Technology*, vol. 10, no. 4, pp. 302–313, 2016.

- [136] B. Zhang, C. Zimmer, and J.-C. Olivo-Marin, "Tracking fluorescent cells with coupled geometric active contours," in *Biomedical Imaging: Nano to Macro, 2004. IEEE International Symposium on*, 2004, pp. 476–479.
- [137] P. W. Huang and Y. H. Lai, "Effective segmentation and classification for HCC biopsy images," *Pattern Recognition*, vol. 43, no. 4, pp. 1550–1563, 2010.
- [138] S. Ali, R. Veltri, J. I. Epstein, C. Christudass, and A. Madabhushi, "Selective invocation of shape priors for deformable segmentation and morphologic classification of prostate cancer tissue microarrays," *Computerized medical imaging and graphics*, vol. 41, pp. 3–13, 2015.
- [139] M. S. Nosrati and G. Hamarneh, "Local optimization based segmentation of spatially-recurring, multi-region objects with part configuration constraints," *IEEE Transactions on Medical Imaging*, vol. 33, no. 9, pp. 1845–1859, 2014.
- [140] A. L. Samuel, "Some studies in machine learning using the game of checkers," *IBM Journal of Research and Development*, vol. 3, no. 3, pp. 210–229, 1959.
- [141] W. L. Hosch, "Machine learning-artificial intelligence," 2016. [Online]. Available: <http://www.britannica.com/EBchecked/topic/1116194/machine-learning>
- [142] F. Provost and R. Kohavi, "Guest editors' introduction: On applied research in machine learning," *Machine Learning*, vol. 30, no. 2, pp. 127–132, 1998.
- [143] C. Cortes and V. Vapnik, "Support-vector networks," *Machine Learning*, vol. 20, no. 3, pp. 273–297, 1995.
- [144] H. Su, F. Xing, J. D. Lee, C. A. Peterson, and L. Yang, "Automatic myonuclear detection in isolated single muscle fibers using robust ellipse fitting and sparse representation," *IEEE/ACM Transactions on Computational Biology and Bioinformatics*, vol. 11, no. 4, pp. 714–726, 2014.

- [145] H. Su, F. Xing *et al.*, “Learning based automatic detection of myonuclei in isolated single skeletal muscle fibers using multi-focus image fusion,” in *Biomedical Imaging (ISBI), 2013 IEEE 10th International Symposium on*. IEEE, 2013, pp. 432–435.
- [146] A. M. Khan, H. El-Daly, and N. M. Rajpoot, “A gamma-gaussian mixture model for detection of mitotic cells in breast cancer histopathology images,” in *Pattern Recognition (ICPR), 2012 21st International Conference on*, 2012, pp. 149–152.
- [147] L. Breiman, “Random forests,” *Machine learning*, vol. 45, no. 1, pp. 5–32, 2001.
- [148] C. Sommer, L. Fiaschi, F. A. Hamprecht, and D. W. Gerlich, “Learning-based mitotic cell detection in histopathological images,” in *Pattern Recognition (ICPR), 2012 21st International Conference on*. IEEE, 2012, pp. 2306–2309.
- [149] K. Sirinukunwattana, A. M. Khan, and N. M. Rajpoot, “Cell words: Modelling the visual appearance of cells in histopathology images,” *Computerized Medical Imaging and Graphics*, vol. 42, pp. 16–24, 2015.
- [150] J. Wright, A. Y. Yang, A. Ganesh, S. S. Sastry, and Y. Ma, “Robust face recognition via sparse representation,” *IEEE Transactions on Pattern Analysis and Machine Intelligence*, vol. 31, no. 2, pp. 210–227, 2009.
- [151] G. Dong, N. Ray, and S. T. Acton, “Intravital leukocyte detection using the gradient inverse coefficient of variation,” *IEEE Transactions on Medical Imaging*, vol. 24, no. 7, pp. 910–924, 2005.
- [152] Y. LeCun, Y. Bengio, and G. Hinton, “Deep learning,” *Nature*, vol. 521, no. 7553, pp. 436–444, 2015.

- [153] L. Deng, D. Yu *et al.*, “Deep learning: methods and applications,” *Foundations and Trends® in Signal Processing*, vol. 7, no. 3–4, pp. 197–387, 2014.
- [154] Y. Bengio *et al.*, “Learning deep architectures for ai,” *Foundations and trends® in Machine Learning*, vol. 2, no. 1, pp. 1–127, 2009.
- [155] Y. Bengio, A. Courville, and P. Vincent, “Representation learning: A review and new perspectives,” *IEEE Transactions on Pattern Analysis and Machine Intelligence*, vol. 35, no. 8, pp. 1798–1828, 2013.
- [156] I. Arel, D. C. Rose, and T. P. Karnowski, “Deep machine learning—a new frontier in artificial intelligence research [research frontier],” *IEEE Computational Intelligence Magazine*, vol. 5, no. 4, pp. 13–18, 2010.
- [157] G. E. Hinton and R. R. Salakhutdinov, “Reducing the dimensionality of data with neural networks,” *Science*, vol. 313, no. 5786, pp. 504–507, 2006.
- [158] H. Su, F. Xing, X. Kong, Y. Xie, S. Zhang, and L. Yang, “Robust cell detection and segmentation in histopathological images using sparse reconstruction and stacked denoising autoencoders,” *International Conference on Medical Image Computing and Computer-Assisted Intervention (MICCAI)*, vol. 9351, pp. 383–390, 2015.
- [159] L. Deng, D. Yu *et al.*, “Deep learning: methods and applications,” *Foundations and Trends in Signal Processing*, vol. 7, no. 3–4, pp. 197–387, 2014.
- [160] H. R. Roth, L. Lu, A. Seff, K. M. Cherry, J. Hoffman, S. Wang, J. Liu, E. Turkbey, and R. M. Summers, “A new 2.5 d representation for lymph node detection using random sets of deep convolutional neural network observations,” in *International Conference on Medical Image Computing and Computer-Assisted Intervention*, 2014, pp. 520–527.

- [161] Y. LeCun, L. Bottou, Y. Bengio, and P. Haffner, “Gradient-based learning applied to document recognition,” *Proceedings of the IEEE*, vol. 86, no. 11, pp. 2278–2324, 1998.
- [162] Y. LeCun, K. Kavukcuoglu, and C. Farabet, “Convolutional networks and applications in vision,” in *Circuits and Systems (ISCAS), Proceedings of 2010 IEEE International Symposium on*, 2010, pp. 253–256.
- [163] A. Krizhevsky, I. Sutskever, and G. E. Hinton, “Imagenet classification with deep convolutional neural networks,” in *Advances in Neural Information Processing Systems*, 2012, pp. 1097–1105.
- [164] C. Farabet, C. Couprie, L. Najman, and Y. LeCun, “Learning hierarchical features for scene labeling,” *IEEE Transactions on Pattern Analysis and Machine Intelligence*, vol. 35, no. 8, pp. 1915–1929, 2013.
- [165] R. Collobert and J. Weston, “A unified architecture for natural language processing: Deep neural networks with multitask learning,” in *Proceedings of the 25th international conference on Machine learning*, 2008, pp. 160–167.
- [166] B. Dong, L. Shao, M. D. Costa, O. Bandmann, and A. F. Frangi, “Deep learning for automatic cell detection in wide-field microscopy zebrafish images,” in *Biomedical Imaging (ISBI), 2015 IEEE 12th International Symposium on*, 2015, pp. 772–776.
- [167] Y. Mao, Z. Yin, and J. M. Schober, “Iteratively training classifiers for circulating tumor cell detection,” in *Biomedical Imaging (ISBI), 2015 IEEE 12th International Symposium on*, 2015, pp. 190–194.
- [168] F. Xing, Y. Xie, and L. Yang, “An automatic learning-based framework for robust nucleus segmentation,” *IEEE Transactions on Medical Imaging*, vol. 35, no. 2, pp. 550–566, 2016.

- [169] F. Liu and L. Yang, “A novel cell detection method using deep convolutional neural network and maximum-weight independent set,” in *International Conference on Medical Image Computing and Computer-Assisted Intervention*, 2015, pp. 349–357.
- [170] A. BenTaieb and G. Hamarneh, “Topology aware fully convolutional networks for histology gland segmentation,” in *International Conference on Medical Image Computing and Computer-Assisted Intervention*. Springer, 2016, pp. 460–468.
- [171] M. Veta *et al.*, “Breast cancer histopathology image analysis: A review,” *IEEE Transaction on Biomedical Engineering*, vol. 61, no. 5, pp. 1400–1411, 2014.
- [172] S. Colantonio, I. B. Gurevich, and O. Salvetti, “Automatic fuzzy-neural based segmentation of microscopic cell images,” *International Journal of Signal and Imaging Systems Engineering*, vol. 1, no. 1, pp. 18–24, 2008.
- [173] H.-Q. Huang, X.-Z. Fang, J. Shi, and J. Hu, “Abnormal localization of immature precursors (alip) detection for early prediction of acute myelocytic leukemia (aml) relapse,” *Medical & Biological Engineering & Computing*, vol. 52, no. 2, pp. 121–129, 2014.
- [174] C. Tripodo, C. Valenti, B. Ballarò, Z. Rudzki, D. Tegolo, V. D. Gesù, A. M. Florena, and V. Franco, “Megakaryocytic features useful for the diagnosis of myeloproliferative disorders can be obtained by a novel unsupervised software analysis,” *Histology and Histopathology*, vol. 21, no. 8, pp. 813–821, 2006.
- [175] T.-H. Song, V. Sanchez, H. EIDaly, and N. Rajpoot, “A circumscribing active contour model for delineation of nuclei and membranes of megakaryocytes in bone marrow trephine biopsy images,” in *Proc. SPIE, Medical Imaging 2015: Digital Pathology*, vol. 9420, 2015.

- [176] J. J. Michiels, H. De Raeve, K. Hebeda, K. H. Lam, Z. Berneman, W. Schroyens, and J. Schwarz, “Who bone marrow features and european clinical, molecular, and pathological (ecmp) criteria for the diagnosis of myeloproliferative disorders,” *Leukemia research*, vol. 31, no. 8, pp. 1031–1038, 2007.
- [177] K. Murtaza, S. Khan, and N. Rajpoot, “Villagefinder: Segmentation of nucleated villages in satellite imagery,” in *Proceedings of the British Machine Vision Conference*, ser. BMVA Press, A. Cavallaro, S. Prince, and D. Alexander, Eds., 2009, pp. 83.1–83.11.
- [178] J. Bruna and S. Mallat, “Invariant scattering convolution network,” *IEEE Transactions on Pattern Analysis and Machine Intelligence*, vol. 35, no. 8, pp. 1872–1886, 2013.
- [179] C. D. Boor, *A practical guide to splines*. New York: Springer-Verlag, 1978.
- [180] J. Mille, “Narrow band region-based active contours and surfaces for 2D and 3D segmentation,” *Computer Vision and Image Understanding*, vol. 113, no. 9, pp. 946–965, 2009.
- [181] Q. Zheng and E. Q. Dong, “Narrow band active contour model for local segmentation of medical and texture images,” *Acta Automatica Sinica*, vol. 39, no. 1, pp. 21–30, 2013.
- [182] A. Khadidos *et al.*, “Weighted level set evolution based on local edge features for medical image segmentation,” *IEEE Transection on Image Processing*, 2017.
- [183] J. Thiele, M. Imbert, R. Pierre, J. W. Vardiman, R. D. Brunning, and G. Flan-drin, “Chronic idiopathic myelofibrosis. who classification of tumours: tumours of haematopoietic and lymphoid tissues,” *IARC Press. Lyon*, pp. 35–38, 2001.

- [184] R. Annunziata, A. Kheirkhah, P. Hamrah, and E. Trucco, “Scale and curvature invariant ridge detector for tortuous and fragmented structures,” *Medical Image Computing and Computer Assisted Interventions (MICCAI)*, pp. 588–595, October 2015.
- [185] K. Zeng, J. Yu, R. Wang, C. Li, and D. Tao, “Coupled deep autoencoder for single image super-resolution,” *IEEE Transactions on Cybernetics*, no. 99, pp. 1–11, November 2015.
- [186] Y. Ian Boureau, Y. L. Cun *et al.*, “Sparse feature learning for deep belief networks,” in *Advances in Neural Information Processing Systems 20 (NIPS 2007)*, Vancouver, Canada, December 2008, pp. 1185–1192.
- [187] N. Jiang, W. Rong, B. Peng, Y. Nie, and Z. Xiong, “An empirical analysis of different sparse penalties for autoencoder in unsupervised feature learning,” in *Neural Networks (IJCNN), 2015 International Joint Conference on.* IEEE, 2015, pp. 1–8.
- [188] D. Kingma and J. Ba, “Adam: A method for stochastic optimization,” *arXiv preprint arXiv:1412.6980*, 2014.
- [189] H. Chang, J. Han, A. Borowsky, L. Loss, J. W. Gray, P. T. Spellman, and B. Parvin, “Invariant delineation of nuclear architecture in glioblastoma multiforme for clinical and molecular association,” *IEEE Transactions on Medical Imaging*, vol. 32, no. 4, pp. 670–682, 2013.
- [190] H. Fatakdawala, J. Xu, A. Basavanthally, G. Bhanot, S. Ganesan, M. Feldman, J. E. Tomaszewski, and A. Madabhushi, “Expectation–maximization-driven geodesic active contour with overlap resolution (emagacor): Application to lymphocyte segmentation on breast cancer histopathology,” *IEEE Transactions on Biomedical Engineering*, vol. 57, no. 7, pp. 1676–1689, 2010.

- [191] M. Kuse, M. Khan, N. Rajpoot, V. Kalasannavar, and Y. F. Wang, “Local isotropic phase symmetry measure for detection of beta cells and lymphocytes,” *J. Pathol. Inform.*, vol. 2, no. 2, p. 2, 2011.
- [192] M. T. McCann, J. A. Ozolek, C. A. Castro, B. Parvin, and J. Kovacevic, “Automated histology analysis: Opportunities for signal processing,” *IEEE Signal Processing Magazine*, vol. 32, no. 1, pp. 78–87, 2015.
- [193] D.-C. Huang, K.-D. Hung, and Y.-K. Chan, “A computer assisted method for leukocyte nucleus segmentation and recognition in blood smear images,” *Journal of Systems and Software*, vol. 85, no. 9, pp. 2104–2118, 2012.
- [194] N. Theera-Umpon, “White blood cell segmentation and classification in microscopic bone marrow images,” *Fuzzy systems and knowledge discovery*, pp. 485–485, 2005.
- [195] S. Ali and A. Madabhushi, “An integrated region-, boundary-, shape-based active contour for multiple object overlap resolution in histological imagery,” *IEEE Transactions on Medical Imaging*, vol. 31, no. 7, pp. 1448–1460, 2012.
- [196] H. Sharma, N. Zerbe, D. Heim, S. Wienert, H.-M. Behrens, O. Hellwich, and P. Hufnagl, “A multi-resolution approach for combining visual information using nuclei segmentation and classification in histopathological images.” in *VISAPP (3)*, 2015, pp. 37–46.
- [197] K. Nguyen, J. Bredno, and D. A. Knowles, “Using contextual information to classify nuclei in histology images,” in *Biomedical Imaging (ISBI), 2015 IEEE 12th International Symposium on*. IEEE, 2015, pp. 995–998.
- [198] N. Bayramoglu and J. Heikkilä, “Transfer learning for cell nuclei classification in histopathology images,” in *Computer Vision–ECCV 2016 Workshops*. Springer, 2016, pp. 532–539.

- [199] S. Ensafi, S. Lu, A. A. Kassim, and C. L. Tan, “A bag of words based approach for classification of hep-2 cell images,” in *Pattern Recognition Techniques for Indirect Immunofluorescence Images (I3A), 2014 1st Workshop on*. IEEE, 2014, pp. 29–32.
- [200] K. H. Lee, S. J. Kang, W. H. Kang, and N. S. Kim, “Two-stage noise aware training using asymmetric deep denoising autoencoder,” *Acoustics, Speech and Signal Processing (ICASSP), 2016 IEEE International Conference on*, pp. 5765–5769, 2016.
- [201] T.-H. Song, V. Sanchez, H. EIDaly, and N. Rajpoot, “Hybrid deep autoencoder with curvature gaussian for detection of various types of cells in bone marrow trephine biopsy images,” in *Biomedical Imaging (ISBI 2017), 2017 IEEE 14th International Symposium on*. IEEE, 2017, pp. 1040–1043.